Analysis of Hypothetical Severe Accidents in Boiling Water Reactors with ASTEC Code and Estimation of Radiological Impact with JRODOS

Zur Erlangung des akademischen Grades eines
DOKTORS DER INGENIEURWISSENSCHAFTEN (Dr.-Ing.)

von der KIT-Fakultät für Maschinenbau des
Karlsruher Instituts für Technologie (KIT)
angenommene
DISSERTATION

von

M.Sc. Onur Murat

Tag der mündlichen Prüfung: 03.11.2026

Hauptreferent: Prof. Dr. -Ing. Marco K. Koch
Ruhr-Universität Bochum

Korreferenten: Prof. Dr. José Cesar Queral Salazar
Universidad Politécnica de Madrid

Prof. Dr. -Ing. Xu Cheng
Karlsruhe Institut für Technologie

2026

Acknowledgements

I would like to thank Dr. Victor Hugo Sanchez Espinoza and Dr. Fabrizio Gabrielli for their support and guidance and to our great RPD team in the institute for always creating great working environment for me.

I would like to express one more time in here my deepest condolences for Prof. Robert Stieglitz and would like to thank him for his guidance.

I would like to thank my parents, Erhan Murat and Vildan Murat, for their enormous efforts throughout my entire life to make me a decent person and ensuring that I receive a proper education. They will forever be my absolute support.

I would like to thank my little companies in this life: Sezar, Simba, Korsan and Minos for bringing joy in my life.

I would like to thank my supervisors Prof. Sule Ergün and Prof. Mehmet Tombakoglu in Hacettepe University for their educational and guiding lessons during my undergraduate and graduate period.

I would like to thank Prof. A.M. Celal Sengör for always keeping my interest in science fresh with his mastery of his field and his impressive ability for simplifying even the most complex subjects have been truly inspiring.

I would like to express my deepest and sincere gratitude to Mustafa Kemal Atatürk, the visionary founder of the modern Republic of Turkey. On the 100th anniversary of the republic, I would like to thank him again for all the achievements he has made for the nation. During these challenging times, I wish to remind every Turkish citizen to keep in mind Atatürk's following words:

"*Science is the only true guide in the life.*"

And always strive for:

"*Peace at home, peace in the world.*"

Karlsruhe, November 2026 Onur Murat

Abstract

Following the Fukushima Daiichi accident, the accurate estimation of severe accident consequences for Boiling Water Reactors has become a critical priority in nuclear safety research. While the estimation of radiological impacts for Pressurized Water Reactors using the European reference code ASTEC is well established, a comparable methodology for BWRs is lacking, primarily because there are no operating BWRs in France. Consequently, there is an urgent need to develop a dedicated computational chain based on ASTEC to predict the radiological consequences of BWR core meltdown accidents. The information generated by such a computational route is of high importance for emergency response teams to plan effective countermeasures and protect the public following a significant release of radioactive materials.

This dissertation aims to contribute to the development of a first-of-a-kind computational chain to realistically and accurately estimate the environmental impact of severe BWR accidents. This integrated route couples tools for precise nuclide inventory prediction, the simulation of in-vessel core degradation and ex-vessel fission product transport using ASTEC, and atmospheric dispersion modeling using the JRODOS decision support system.

As a foundational step, recently implemented BWR specific core degradation models in ASTEC were validated against the QUENCH-20 experimental test. It was demonstrated that these models describe the heat transfer and oxidation of absorber blades, canisters, and water rods with acceptable accuracy. The code successfully predicted global hydrogen production and the local axial temperature evolution of the core components within the typical error bands of severe accident codes. This validation confirmed the adequacy of ASTEC for full-scale BWR plant analysis.

Following this validation, a full-scale, integral ASTEC model of the BWR Peach Bottom Unit-2 was developed entirely from scratch to estimate the radiological source term during severe accident sequences. Notably, an explicit and novel representation of the jet pump hydrodynamics was implemented using native ASTEC capabilities, which significantly improved the estimation of downcomer flow rates and water coast-down profiles.

To evaluate the impact of core loading and burnup history on severe accident progression and the resulting radiological severity, two distinct configurations were modeled: a historical core loading utilizing 7x7 low-burnup fuel assemblies, and a modernized core loading utilizing GE14 10x10 high-burnup assemblies. Precise initial radionuclide inventories at the time of accident initiation were calculated using neutronic codes (ORIGEN and CASMO) and fed directly into the severe accident model.

A Short-Term Station Blackout was selected as the reference transient to demonstrate the capability of this computational chain. A comparative analysis revealed that the modernized, high-burnup core significantly altered the accident progression timeline compared to the historical core. Furthermore, the analysis determined that the radiological source term for the high-burnup configuration, while one order of magnitude lower than Fukushima Daiichi estimates, still represents a massive environmental hazard. For emergency preparedness, extracting source term data from this worst-case, high-burnup scenario is inherently more conservative and valuable.

Finally, the source terms calculated by ASTEC were deployed into the JRODOS code for atmospheric dispersion analysis. To overcome the limitations of standard, single-day weather simulations, a massive statistical approach was introduced based on the Central Limit Theorem. Utilizing this approach, tens of thousands of multi-year dispersion scenarios were simulated across a 400 km regional grid. This extensive databank enabled the construction of novel, probabilistic Risk Maps. By visualizing both the maximum effective gamma dose rates and their geographic impact frequencies, these Risk Maps provide a powerful, high-resolution tool for decision-makers and emergency teams to plan countermeasures, mitigate the consequences of severe radiological releases, and ultimately protect citizens.

Kurzfassung

Nach dem Unfall von Fukushima Daiichi hat die präzise Abschätzung der Folgen schwerer Unfälle bei Siedewasserreaktoren in der Forschung zur nuklearen Sicherheit höchste Priorität erlangt. Während die Abschätzung radiologischer Auswirkungen für Druckwasserreaktoren unter Verwendung des europäischen Referenzcodes ASTEC bereits etabliert ist, fehlt eine vergleichbare Methodik für Siedewasserreaktoren – vor allem deshalb, weil in Frankreich keine Siedewasserreaktoren betrieben werden. Folglich besteht dringender Bedarf an der Entwicklung einer dedizierten Rechenkette auf Basis von ASTEC, um die radiologischen Folgen von Kernschmelzunfällen in Siedewasserreaktoren prognostizieren zu können. Die durch ein solches Rahmenwerk gewonnenen Informationen sind für Katastrophenschutzteams von entscheidender Bedeutung, um nach einer signifikanten Freisetzung radioaktiver Stoffe wirksame Gegenmaßnahmen planen und die Bevölkerung schützen zu können.

Diese Dissertation zielt darauf ab, zur Entwicklung einer neuartigen Rechenkette beizutragen, um die Umweltauswirkungen schwerer Störfälle in Siedewasserreaktoren (BWR) realistisch und präzise abzuschätzen. Dieses integrierte Rahmenwerk verknüpft Werkzeuge zur präzisen Vorhersage des Nuklidinventars, zur Simulation der Kernzerstörung im Reaktordruckbehälter sowie des Spaltproduktttransports außerhalb des Behälters unter Verwendung von ASTEC und zur Modellierung der atmosphärischen Ausbreitung mittels des Entscheidungsunterstützungssystems JRODOS.

Als grundlegender Schritt wurden die kürzlich in ASTEC implementierten, spezifischen Modelle zur Kernzerstörung in Siedewasserreaktoren (BWR) anhand des experimentellen Tests QUENCH-20 validiert. Dabei konnte nachgewiesen werden, dass diese Modelle den Wärmeübergang sowie die Oxidation von Absorberplatten, Kanistern und Wasserstäben mit akzeptabler Genauigkeit beschreiben. Der Code prognostizierte sowohl die globale Wasserstoffproduktion als auch den lokalen axialen Temperaturverlauf der Kernkomponenten erfolgreich innerhalb der für Codes zur Analyse schwerer Störfälle typischen Fehlerbandbreiten. Diese Validierung bestätigte die Eignung von ASTEC für die umfassende Analyse von BWR-Anlagen.

Im Anschluss an diese Validierung wurde ein umfassendes, integrales ASTEC-Modell des Siedewasserreaktors Peach Bottom Unit-2 vollständig neu entwickelt, um den radiologischen Quellterm während schwerer Störfallabläufe abzuschätzen. Insbesondere wurde unter Nutzung nativer ASTEC-Funktionalitäten eine explizite und neuartige Darstellung der Hydrodynamik der

Strahlpumpen implementiert, was die Abschätzung der Durchflussraten im Ringraum sowie der Profile des Wasserstands-Abfalls signifikant verbesserte.

Um den Einfluss der Kernbeladung und der Abbrandhistorie auf den Ablauf schwerer Störfälle sowie die daraus resultierende radiologische Schwere zu bewerten, wurden zwei unterschiedliche Konfigurationen modelliert: eine historische Kernbeladung unter Verwendung von 7x7-Brennelementen mit geringem Abbrand und eine modernisierte Kernbeladung unter Verwendung von GE14-10x10-Brennelementen mit hohem Abbrand. Die exakten anfänglichen Radionuklidinventare zum Zeitpunkt des Störfallbeginns wurden mithilfe neutronenphysikalischer Codes (ORIGEN und CASMO) berechnet und direkt in das Modell für schwere Störfälle eingespeist.

Als Referenztransient zur Demonstration der Leistungsfähigkeit dieser Rechenkette wurde ein kurzzeitiger Stations-Blackout ausgewählt. Eine vergleichende Analyse ergab, dass der modernisierte Kern mit hohem Abbrand den zeitlichen Ablauf des Störfalls im Vergleich zum historischen Kern signifikant veränderte. Des Weiteren stellte die Analyse fest, dass der radiologische Quellterm für die Konfiguration mit hohem Abbrand – wenngleich er um eine Größenordnung unter den Schätzungen für Fukushima Daiichi liegt – dennoch eine massive Umweltgefahr darstellt. Für die Notfallvorsorge ist die Ableitung von Quellterm-Daten aus diesem Worst-Case-Szenario mit hohem Abbrand naturgemäß konservativer und wertvoller.

Schließlich wurden die von ASTEC berechneten Quellterme in den JRODOS-Code zur Analyse der atmosphärischen Ausbreitung integriert. Um die Einschränkungen standardmäßiger, auf Einzelereignissen basierender Wettersimulationen zu überwinden, wurde ein umfassender statistischer Ansatz eingeführt, der auf dem Zentralen Grenzwertsatz beruht. Unter Anwendung dieses Ansatzes wurden Zehntausende mehrjähriger Ausbreitungsszenarien auf einem regionalen Raster von 400 km simuliert. Diese umfangreiche Datenbank ermöglichte die Erstellung neuartiger, probabilistischer Risikokarten. Durch die Visualisierung sowohl der maximalen effektiven Gamma-Dosisleistungen als auch ihrer geografischen Häufigkeiten des Auftretens stellen diese Risikokarten ein leistungsstarkes, hochauflösendes Instrument für Entscheidungsträger und Einsatzkräfte dar, um Gegenmaßnahmen zu planen, die Folgen schwerwiegender radiologischer Freisetzungen abzumildern und letztlich die Bevölkerung zu schützen.

Publications related to this thesis

- Murat, O., Sanchez-Espinoza, V., Gabrielli, Wang, S., F., Stieglitz, R., and Queral, C., "Improved Analysis of the Short-Term Station Blackout Accidents of the Peach Bottom Unit-2 Reactor with ASTEC Including Radiological Impact and Statistical Analysis with JRODOS", Nuclear Engineering and Design, Vol. 420, pages 113012, 2024. DOI: 10.1016/j.nucengdes.2024.113012
- V.H. Sanchez-Espinoza, F. Gabrielli, U. Imke, K. Zhang, L. Mercatali, G. Huaccho, J. Duran, A. Campos, A. Stakhanova, O. Murat, A.K. Mercan, J. Etcheto, M. Steinbrück, J. Stuckert, S. Gabriel, S. Ottenburger, R. Stieglitz, W. Tromm, "KIT reactor safety research for LWRs: Research lines, numerical tools, and prospects", Nuclear Engineering and Design, Volume 414, 2023, 112573, ISSN 0029-5493, DOI: 10.1016/j.nucengdes.2023.112573.
- Murat, O., Sanchez-Espinoza, V., Gabrielli, F., Stieglitz, R., and Queral, C., "Analysis of the Short Term-Station Blackout Accident at the Peach Bottom Unit-2 Reactor with ASTEC Including the Estimation of the Radiological Impact with JRODOS", Nuclear Engineering and Design, Vol. 406, 2023. DOI: 10.1016/j.nucengdes.2023.112227
- Murat, O., Sanchez-Espinoza, V., Stieglitz, R., "Peach Bottom Unit-2 ASTEC V2.2.0.1 Model and Stationary Results", ERMSAR 2022 10th European Review Meeting on Severe Accidents Research. DOI: 10.5445/IR/1000148653
- Murat, O., Sanchez-Espinoza, V., Stieglitz, R., "Analysis of QUENCH-20 Test with ASTEC V2.2.b", 26th International QUENCH Workshop, 6-9 December 2021. DOI: 10.5445/IR/1000141824
- Gabrielli, F., Sanchez Espinoza, V.H., Murat, O., Mercan, A.K., Tromm, W., "Employment of the ASTEC Code in the Severe Accidents Research Activities at KIT", 30th International Conference Nuclear Energy for New Europe, September 6-9, 2021.
- Murat, O., Sanchez-Espinoza, V., Wang, S., and Stuckert, J., "Preliminary validation of ASTEC V2.2.b with the QUENCH-20 BWR bundle experiment", Nuclear Engineering and Design, Vol. 370, No. 15, 2020. DOI: 10.1016/j.nucengdes.2020.110931

Content

1 Introduction 1

1.1 Motivation and research gaps 1

1.2 Research questions 4

1.3 Thesis goals 5

2 Peculiarities, Phenomena, Tools and Code Validation 6

2.1 Peculiarities of BWRs 6

2.2 Key severe accident phenomena in BWRs 19

2.3 Key radiological dispersion phenomena following a severe accident 24

2.4 Validation of severe accident codes 25

3 Design of a First-of-the-kind Computational Route for the Prediction of Radiological Consequences after Severe Accidents in BWRs 27

3.1 Introduction 27

3.2 Key elements of the computational route 28

3.2.1 Tools for the nuclide inventory prediction of the core loading: ORIGEN, CASMO5 29

3.2.2 Integral severe accident code: ASTEC 30

3.2.3 Tool for the prediction of dispersion of radioactive isotopes: JRODOS ..31

4 Validation of ASTEC Using QUENCH-20 BWR Test 32

4.1 Introduction 32

4.2 The QUENCH-20 BWR test description 32

4.2.1 BWR test bundle 34

4.2.2 The QUENCH-20 BWR test conduction 37

4.3 Development of an ASTEC-model for QUENCH-20 BWR test 38

4.3.1 Test section model 38

4.3.2 Initial and boundary conditions 40

4.3.3 Selected ASTEC-models relevant for early in-vessel phase of severe accidents 40

4.4 Comparison of ASTEC predictions with experimental data 43

4.5 Conclusion 53

5 Application of the computational route to predict the radiological consequences of severe accidents in BWRs 55

5.1 Realistic prediction of the nuclide inventory of the different core loading of the Peach Bottom Unit-2 BWR 55

5.1.1 Relevance of core loading and irradiation history for radiological impact 55

5.1.2 Nuclide inventory predictions at End of Cycle 56
5.2 Development of an integral Peach Bottom Unit-2 BWR model for severe accident analysis with ASTEC 61
5.2.1 Integral ASTEC Peach Bottom Unit-2 BWR model for steady conditions 62
5.2.2 Core model configurations 63
5.2.3 Reactor pressure vessel and recirculation system models 66
5.2.4 Primary containment vessel and building model 69
5.2.5 Selected ASTEC-models for the simulation of key severe accident phenomena 71
5.3 Verification of ASTEC steady state predictions against reference plant data 72
5.4 Analysis of severe accident scenarios in Peach Bottom Unit-2 BWR for the source term prediction 73
5.4.1 Scenario-1: ST-SBO with core loading with 7x7 fuel assemblies 74
5.4.2 Scenario-2: ST-SBO with modern GE14 10x10 fuel assemblies 75
5.4.3 Scenario-3: ST-SBO with modern GE14 10x10 fuel assemblies with stuck open SRV 75
5.5 Analysis of the Scenario-1: ST-SBO with core loading with 7x7 fuel assemblies .. 76
5.6 Analysis of the Scenario-2: ST-SBO with modern GE14 10x10 fuel assemblies ... 83
5.7 Analysis of the Scenario-3: ST-SBO with modern GE14 10x10 fuel assemblies with stuck open SRV 89

6 Prediction of the Radiological Impact After Severe Accidents 96
6.1 Introduction 96
6.2 Development of JRODOS-model to predict the radionuclide dispersion around BWR site 97
6.2.1 Scenario 1: ST-SBO with historical 7x7 fuel assemblies 97
6.2.2 Scenario 2: ST-SBO with modern GE14 10x10 fuel assemblies 100
6.2.3 Scenario 3: ST-SBO with modern GE14 10x10 fuel assemblies with stuck open SRV 102
6.3 Discussion of the main results 104
6.4 Conclusion 104

7 Development of Risk Map of Radiological Dispersion 106
7.1 Introduction 106
7.2 Development of realistic risk maps for selected region using radiological dispersion 106
7.3 Discussion of the main results 108

8 Main Conclusions 112

9 Outlook 115

Bibliography 117

List of Acronyms

ADS	Automatic Depressurization System
ASTEC	Accident Source Term Evaluation Code
BOC	Beginning of Cycle
BWR	Boiling Water Reactor
CST	Condensate Storage Tank
DID	Defense in Depth
ECCS	Emergency Core Cooling Systems
EOC	End of Cycle
HPCI	High Pressure Coolant Injection
LOCA	Loss of Coolant Accident
LOOP	Loss of Offsite Power
LPCI	Low Pressure Coolant Injection
IAEA	International Atomic Energy Agency
IRSN	Institute for Radiation Protection and Nuclear Safety
IVMR	In Vessel Melt Retention
LOSP	Loss of Offsite Power
LWR	Light Water Reactor
KIT	Karlsruhe Institute of Technology
MCCI	Molten Core Concrete Interaction
MOC	Middle of Cycle
NPP	Nuclear Power Plant
PCV	Primary Containment Vessel
PSA	Probabilistic Safety Assessment
PWR	Pressurized Water Reactor
RCIC	Reactor Core Isolation Cooling
RHR	Residual Heat Removal
RPV	Reactor Pressure Vessel
SAMG	Severe Accident Management Guideline
SBO	Station Blackout
SC	Suppression Chamber
SLC	Standby Liquid Control
SOSRV	Stuck Open Safety Relief Valve
SRV	Safety Relief Valve
SV	Safety Valve
UFSAR	Updated Final Safety Analysis Report

1 Introduction

1.1 Motivation and research gaps

Worldwide , there are more than 300 Pressurized Water Reactors (PWR) and 40 Boiling Water Reactors (BWR) of different designs currently in operation (IAEA, 2023). Despite continuous improvements in nuclear power plant technology, safety systems, and safety standards to improve economics, assure high availability, and maintain the high safety standards required by national regulators, nuclear accidents with severe core damage, such as Chernobyl and Fukushima, have occurred. Extensive research activities started worldwide after the last severe accident in Fukushima to re-evaluate the status of all operating Nuclear Power Plants (NPPs), and to estimate the hypothetical radiological risks to which society may be exposed as a consequence of core meltdown accidents (OECD and Nuclear Energy Agency, 2021). Even though severe accidents are local events, their radiological consequences cross country borders and may impact large areas around the site and at distant areas depending of the specific weather conditions on-site at the time of occurrence of the accident. In addition, the amount of radiological source term and the timing of release into the environment depends strongly of the peculiar design characteristics of a Nuclear Power Plant (NPP) type, the operational history, core loading with fissile material and last but not least of the accidental sequence leading to core-meltdown and subsequence failure of the safety barriers i.e., fuel cladding, Reactor Pressure Vessel (RPV), water circuit systems, and containment. It is also evident that the implementation of additional safety measures when moving from Generation-2 to Generation-3 reactors does not eliminate the risk entirely. For this reason, it is of prominent importance to develop computational routes consisting of different numerical tools for the prediction of the realistic nuclide inventories of core loadings, the phenomena taking place during the core degradation, fission product releases and transport along the pathways of potential severe accident sequences and finally of the radiological dispersion of the fission products released from an NPP. This information is very important for emergency teams to develop action plans and get in time and as accurate as possible to be able to develop countermeasures, to take decisions aimed to minimize the consequences of core-meltdown accidents for the environment and population. Moreover, to assure reliable predictions of the different numerical tools part of the computational routes used for such purposes, the validation using available experimental data relevant for each reactor design is a mandatory step before the tools are applied for safety assessments.

It is worth recalling that the Defense-in-Depth (DiD) concept (IAEA, 1999) relies on two important principles: prevention and mitigation. Hence, numerous preventive measures are foreseen and implemented in NPPs for each safety level between 1 and 3 of the DiD concept to hinder the occurrence of severe accidents, i.e., to prevent entering safety levels 4 and 5. If a severe accident cannot be prevented, the focus shifts to mitigative measures to minimize the consequences (safety levels 4 and 5, known as Severe Accident Management Guidelines). In order to effectively implement Severe Accident Management Guidelines (SAMG) it is required to have deep knowledge of the severe accident phenomena taking place inside the RPV, which is called in-vessel phenomena, and outside the RVP, which is called ex-vessel phenomena, is necessary for representative severe accident sequences of any reactor design. Numerical simulations by using integral severe accident codes could provide a deep understanding of the NPP behavior during severe accident sequences with fission product releases and estimations of amount and timing of the released fission products for any failure mode of the safety barriers can be performed.

The radiological risk after a severe accident is represented by the amount and time-dependent release of radioactive substances from NPPs into the environment (air, soil, groundwater, rivers, etc.). After the occurrence of a severe accident, it is of paramount importance for emergency teams to know the time-dependent release of radioactive substances (type of nuclide, amount, state, and spatial distribution) in order to initiate appropriate countermeasures. This protects the population in and around the NPP site and along the path of the radioactive cloud, depending on local weather conditions. More specifically, the estimation of the radiological risk potentially arising after a severe accident requires of a simulation chain consisting of different simulation tools. These tools describe the core depletion during the operation, the behavior of NPPs after a severe accident, and the dispersion of radioactive substances close to the NPP and along the radioactive cloud, considering local climatic conditions.

Worldwide, different integral severe accident codes, such as MELCOR (Humphries *et al.*, 2017) and MAAP (ERIN Engineering and Research, Inc., 2010) in USA, AC2 (Wielenberg *et al.*, 2019) in Germany, and ASTEC (Chatelard *et al.*, 2016) in France are being developed, validated, and applied to different reactor designs. These tools predict the radiological source term potentially released into the environment needed by the numerical tools that estimate how dispersion of released fissions products around an NPP-site take place and estimate the expected dose in the air, soil and humans.

The severe accident research activities at KIT are heavily relying on the ASTEC code and are done in close cooperation with ASNR (main developer of ASTEC). One goal of this cooperation was to extend the ASTEC-capabilities for the analysis of severe accidents in BWRs and to contribute to the validation using unique KIT-data of the QUENCH BWR program. In addition, a proper representation of the jet pumps of BWR designs is needed in ASTEC for a realistic description of the thermal hydraulic behavior of the recirculated water in RPV system during transients and accidents. Since no BWR-plants are operated in France, the ASTEC-development is mainly focused on severe accidents for PWRs. After Fukushima accident, developments to include the simulation of BWR-specific core components such as absorber cross, guide tubes in the upper plenum, water rods and fuel assembly canisters during early and late phase of severe accidental sequences in the ASTEC-code gained increased interest in France to be able to assess the radiological consequences of BWRs operated outside France. Consequently, new models were implemented in ASTEC to describe the in-vessel phase of severe accidents in BWRs.

It is worth to mention that the material composition of the core structures and components of BWR differs largely from the ones of PWRs, which will impact on the oxidation and chemical energy release and hydrogen generation, amount and composition of the molten material relocated to the lower plenum and on the failure of the RPV, the ex-vessel molten material concrete interactions and so the overall fission product transport from the core to the circuits and to the containment, depending of the accidental sequence.

Furthermore, KIT develops the JRODOS tool, which predicts the radiological dispersion and environmental consequences of isotope releases. Utilizing this in-house tool for dispersion analysis provides critical insights into the real-world impact of severe accidents on public safety and the environment.

Currently, there is a lack of an integrated simulation route capable of coupling core radiological inventories, BWR severe accident progression, and environmental dispersion. Current de-coupled application of different tools for a specific phenomenon (core neutronics, severe accident and radiological dispersion) accidental sequence of a NPP is therefore conservative, prone for errors at the core interfaces. The fission product inventory, which depends on the burn-up stage of the fuel i.e., irradiation during operation, defines the excess heat and thus impact the accident progression dynamics. Then, the time-dependent loss of the safety barrier integrity together with the release of the radiological inventory determines the potential risk to the public and the environment of a severe accident. Consequently, establishing a complete computational chain to determine the radiological consequences after severe accidents of NPPs and specifically of BWRs with release of radioactive materials is an urgent need to enable rigorous

communication with emergency teams and so ensuring accident preparedness and effective countermeasures.

1.2 Research questions

Based on the scientific gaps identified above, the doctoral thesis aims to contribute to answer the following research questions:

- Do methods and tools for the prediction of realistic nuclide inventories of BWR-core loadings with different irradiation history as needed by the severe accident integral codes exist to be part of an integrated computational route for the overall estimation of the radiological impact after severe accidents in BWRs?
- Are ASTEC-models recently implemented for the description of the heat-up, oxidation, eutectic interaction and molten material formation and relocation during the in-vessel phase of a BWR during a severe accident sequence validated using relevant experimental data?
- Does it exist appropriate interfaces to exchange information between severe accident codes and tools like JRODOS for the prediction of radiological dispersion and consequences that assure an automatic transfer of timely radiological source terms in different formats and considering variable number of nuclides to be part of an integrated computational route?
- Can smart alternative methods be developed for a more realistic estimation of the radiological risks including more relevant information that the current JRODOS-computational route for the gathering of reliable information in time and amount of nuclide types and classes depending of the dose to make it available to the emergency teams for better decisions and effective countermeasures?
- Is it feasible to develop an integrated computational route for the risk estimation after severe accidents with release of radioactive material into the environment applicable to any reactor design?

1.3 Thesis goals

The main goals of the doctoral thesis are intended to provide solutions to the listed research questions. For this purpose, the following technical goals are defined below:

1. Explore the best tools and methods for the nuclide inventory predictions of core loading during the operation of a BWR to be part of the computational route that can provide the nuclide inventories in the detail and precision as needed by severe accident codes.
2. Contribute to the validation of the new BWR-models implemented in ASTEC using the experimental data of the KIT QUENCH-BWR test related to the early in-vessel phase.
3. Development from scratch of an integral plant model of a specific BWR-plant to make an analysis of severe accident phenomena including the fission products release with ASTEC code as close as possible to the reality considering the peculiarities of the core of BWRs (representation of canister, water rods, absorber cross) and of the jet pumps located around the downcomer of the RPV using native ASTEC-capability for a realistic representation of the flow circulation inside the RPV.
    a. Check the validity of the model for stationary plant conditions by comparing predicted parameters with reference values of the selected BWR-plant (Peach Bottom Unit-2).
    b. Extend the integral model to consider the safety systems, phenomena and control systems of the plant that will be active during the transient phase of the selected severe accident sequence of choice (Short-Term Station Blackout).
    c. Prepare and modify the radiological source term predicted by ASTEC in the formats and units as needed by the JRODOS tool for radiological consequence analysis.
4. Develop the JRODOS model for a realistic dispersion estimation after a severe accident by selecting the proper space-mesh, time frame for accident and the respective meteorological data over the domain.
5. Design the computational route consisting of the three kind of simulation tools and the respective interfaces for an integrated computational route for BWR radiological impact estimation applicable and extendable for any reactor design.
6. Further development of risk maps for a more detailed estimation of the radiological consequences compared to the traditional method in JRODOS to increase the technical background for better decisions increasing the quality of the countermeasures to protect citizens and environment.

2 Peculiarities, Phenomena, Tools and Code Validation

In order to establish the proposed computational route, a comprehensive understanding of BWR phenomenology and the specific numerical tools required to simulate accident progression from beginning to end is required. This chapter details the physical and operational peculiarities of BWRs such as the unique core hydrodynamics and emergency cooling systems that determine the severe accident progression. Furthermore, it outlines the specific early and late-phase degradation mechanisms, including BWR-specific eutectic interactions and lower plenum melt relocation, which must be accurately captured by the selected simulation tools. Finally, this chapter establishes the critical need for validating these computational models against representative experimental databases, setting the stage for the integral safety assessments performed later in this thesis.

2.1 Peculiarities of BWRs

The design of a BWR relies on the conversion of liquid water into steam within the pressure vessel, and the direct transfer of this steam to the turbines. The general layout of the water cycle in the pressure vessel and the steam flow path through the turbines and condenser is presented in Figure 2-1.

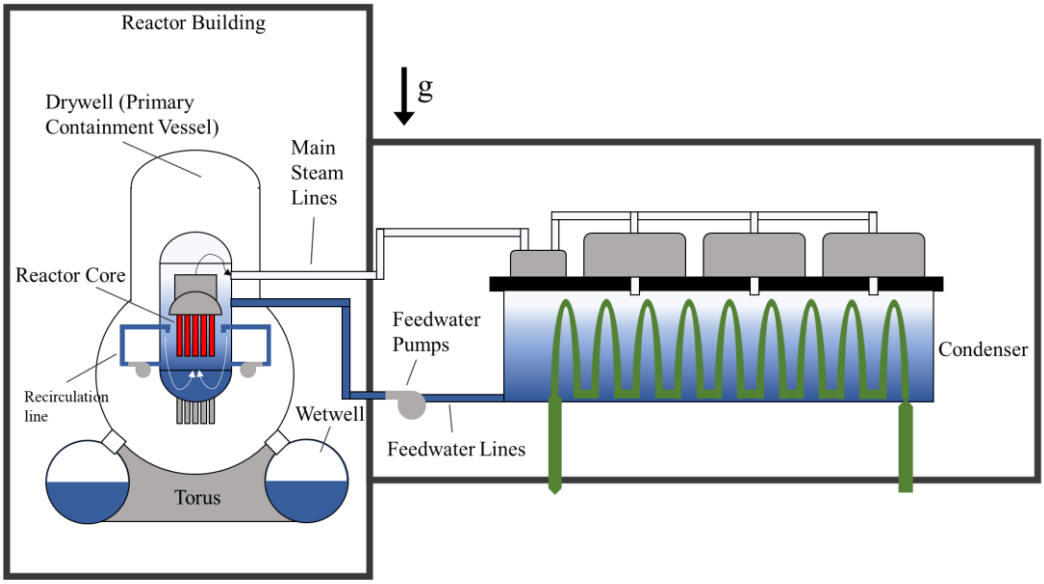


Figure 2-1 Boiling Water Reactor general layout of water cycle.

The BWR core layout and the placement of the fuel assemblies are shown in Figure 2-2. The number and type of fuel assemblies in the core depend on the specific BWR design. In the figure, a generic GE14 10x10 fuel assembly design is presented. The power plant under consideration, Peach Bottom Unit-2, has 764 fuel assemblies in its core. During the operational years of the plant, the types of loaded fuel assemblies have changed, and this evolution is addressed in the following chapters of this thesis. Each fuel assembly host two water rods where coolant flows upwards without having any contact with fuel rods and it increases the averaged coolant density along the core height. In addition, new fuel designs incorporate gadolinium rods and partial-length rods within the fuel assembly to optimize burnup and reactivity control over the cycle. Each group of four fuel assemblies contains one control blade structure positioned between them.

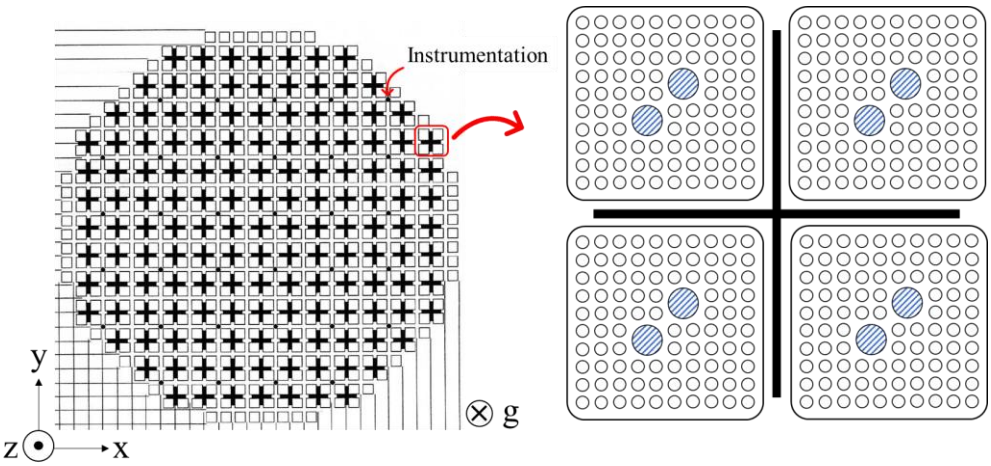


Figure 2-2 Boiling Water Reactor core layout (left) and generic fuel assembly and control blade structures (right).

The injected liquid feedwater enters the downcomer section located between the pressure vessel and the shroud, flows downward, and is drawn into the recirculation loop suction line. The recirculation loop pumps force the water through the recirculation line, directing it from the jet pump nozzle into the jet pump. Approximately one-third of the total core flow is constantly recirculated through the recirculation line by the recirculation pumps. As the high-velocity water flows down into the jet pump cone structures, it drives the surrounding water in the downcomer, and the combined total core flow enters the lower plenum. Moving upward from the lower plenum through the active core region, the water is heated to saturation at operating pressure. Due to the shape and design of the flow paths in the steam separator, steam and liquid water are separated; the liquid flow back to the downcomer section to continue the liquid water cycle, while the separated steam rises and enters the steam dryer. The dryer further increases the dry steam content

in the flow before directing it to the turbines. The water flow path and sections within the pressure vessel are shown in Figure 2-3.

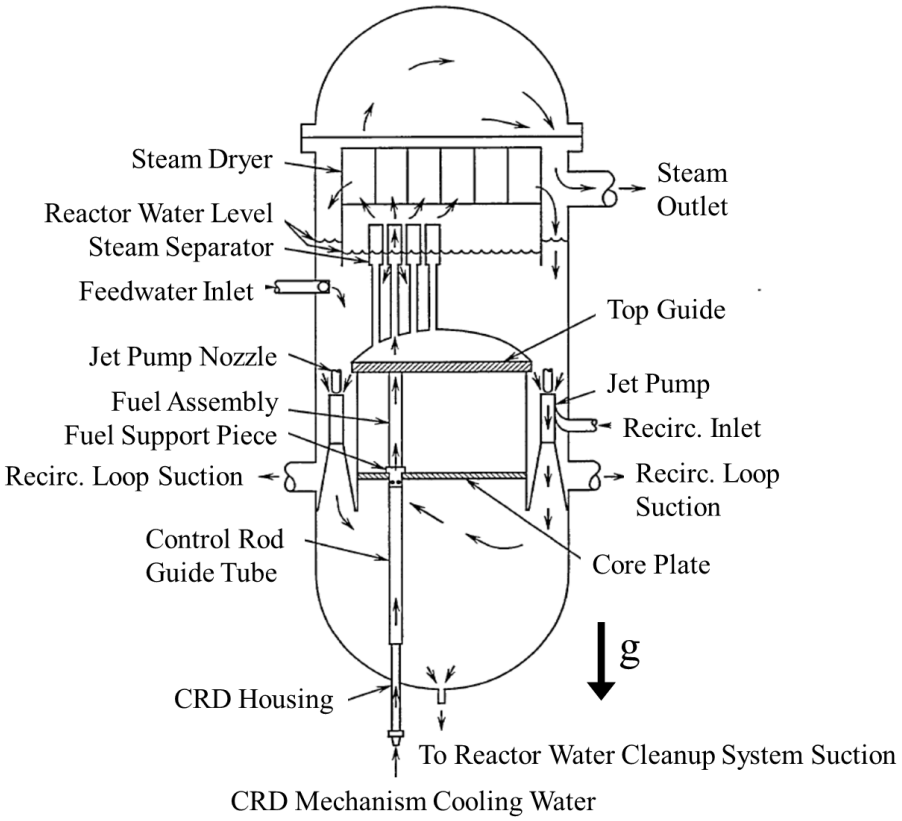


Figure 2-3 Boiling Water Reactor pressure vessel and main internal components.

The Primary Containment Vessel (PCV) consists of two parts: the Drywell and the Wetwell. The Drywell part of the containment hosts the pressure vessel and the concrete cavity in a nitrogen-filled environment. Because the containment volumes of Mark-I and Mark-II BWR designs are smaller than those of generic PWR designs, the containment atmosphere is inerted with nitrogen gas to prevent the risk of hydrogen combustion. However, newer BWR Mark-III containment designs possess volumes comparable to PWR containment designs. The Wetwell part of the PCV consists of a torus-shaped suppression chamber containing a large pool of water. Vents provide a connection from the Drywell to the Wetwell and suppression chamber. The water pool in the suppression chamber acts as a heat sink to remove excess heat from the core. The general schematic of the PCV and pressure vessel arrangement in the Drywell is shown in Figure 2-4.

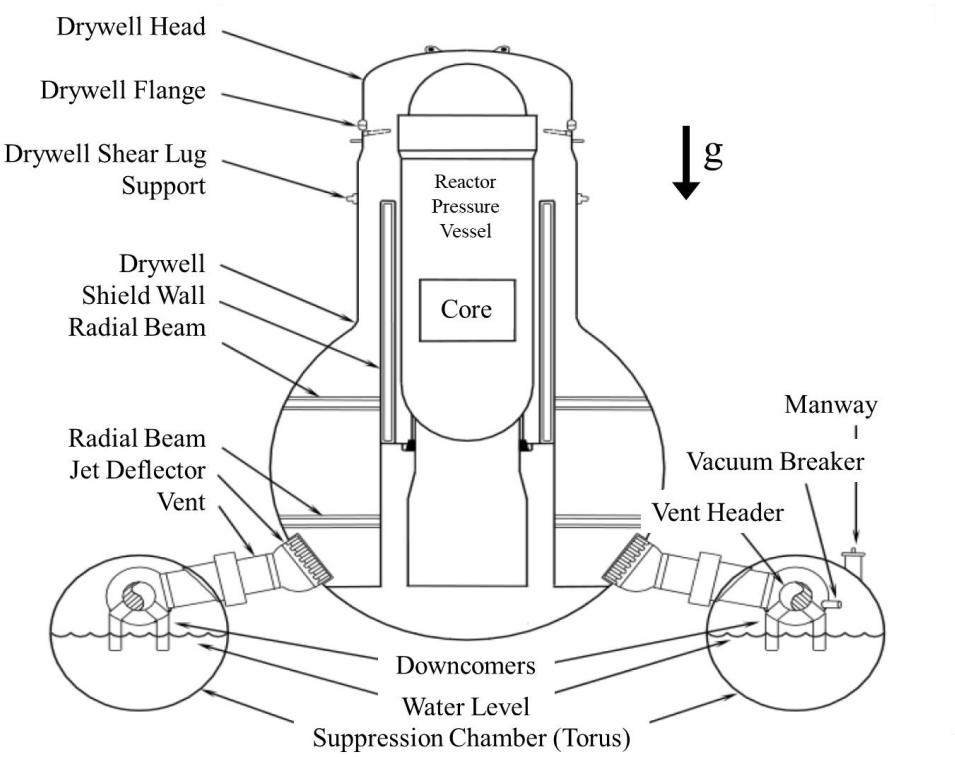


Figure 2-4 BWR4 Mark-1 primary containment vessel.

The surrounding building sections and rooms located outside of the PCV are collectively considered as the reactor building. A reactor building cross-section of the BWR4 Mark-1 design is given in Figure 2-5. Due to the complex layout of the rooms and connections, only the B-B cross-sectional layout is presented here. This specific layout is also the one utilized in the modelling of the reactor building.

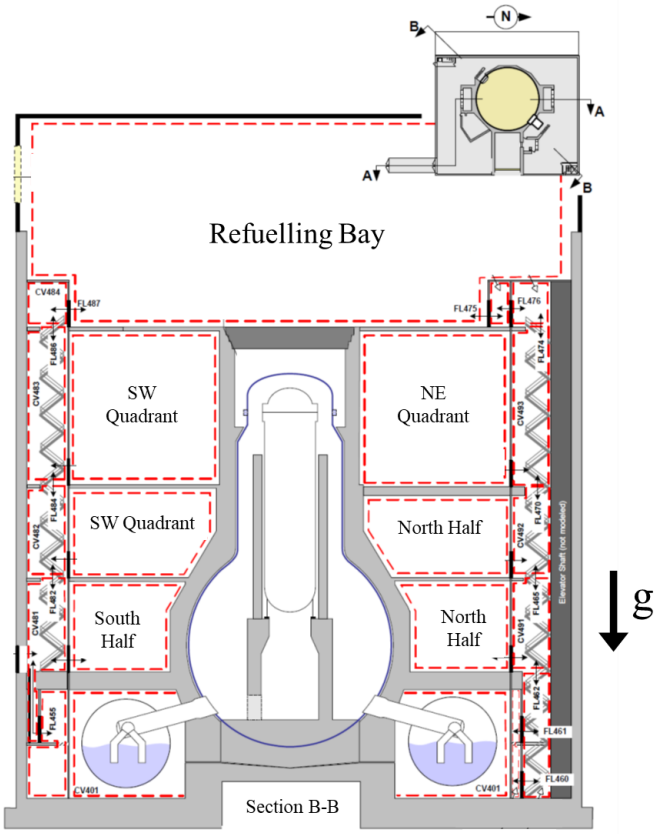


Figure 2-5 BWR4 Mark-1 primary containment vessel and reactor building.

Physical layout of the BWR from the pressure vessel to the primary containment and surrounding reactor building is established and shown in Figure 2-5. However, it is crucial to examine how the plant responds to operational transients. Specific safety systems are designed for heat removal in the event of a normal reactor shutdown or a design-basis accident. An integrated understanding of both the power plant's general layout and these interconnected safety systems is essential for accurately modelling the plant and conducting realistic severe accident analyses.

Considered power plant in the thesis Peach Bottom Unit-2 is a General Electric design BWR4 nuclear reactor with Mark-1 containment type. The plant received its operational license in 1973 on the site closer to the Lancaster PA in U.S. Description of the safety systems which are designed to withstand design basis accidents, reactivity control, coolant and containment systems is given USNRC publication (U.S. Nuclear Regulatory Commission, 2021).

Reactivity control in a BWR is ensured by the Control Rod System and the movement of the control rods within the active core area. In addition, the design of the BWR and the resulting production of steam in the core cause under-moderation due to the presence of steam, which has

a lower density compared to liquid water. Increasing the recirculation water flow and the liquid flow rate relative to steam as well as considering water rods inside the fuel assemblies plays an important role in increasing moderation and power in BWRs (Lahey and Moody, 1993). This reactivity insertion and power control mechanism is also an option in BWR design.

During a normal BWR shutdown process, the residual heat is removed by bypassing the turbine and transferring the extracted steam directly to the main condenser. In case of transients or accidents e.g., core isolation, heat removal from the core is achieved by shutdown heat removal systems consisting of a high-pressure system and a low-pressure system. Reactor Core Isolation Cooling (RCIC) is the high-pressure shutdown heat removal system that ensures the cooling and depressurization of the core. After that, the Residual Heat Removal (RHR) system, which is the low-pressure heat removal system, continues the low-pressure, long-term cooling of the core.

The RCIC system consists of one train containing one turbine, one turbine-driven pump, connection piping, valves, and control units; its basic layout is given in Figure 2-6. Extracted steam from the core is directed to the RCIC turbine, and the power generated by the turbine is distributed to the system pump. The Condensate Storage Tank (CST) ensures the water intake for the RCIC pump, and pressurized water is introduced through the feedwater line. In case of a reduction of the water inventory in the CST storage or a water level increase in the suppression chamber, the water source for the RCIC can be switched from the CST to the suppression chamber.

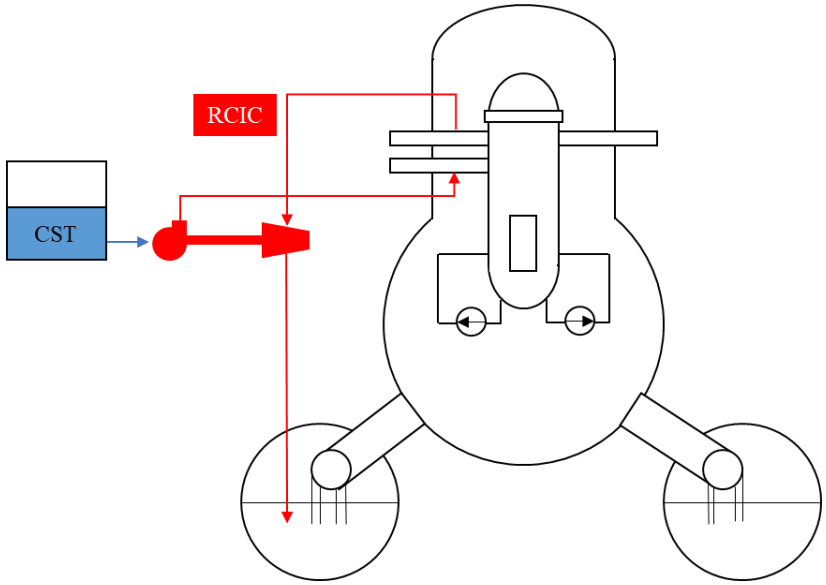


Figure 2-6 General Electric BWR/4 Reactor Core Isolation Cooling System.

The passive RCIC does not require any additional power source to operate. The system turbine, which produces power by using extracted steam from the core, is sufficient to operate the system. Only DC power is required to control the system valves on the connection pipes.

The Residual Heat Removal (RHR) System consists of four sub-systems: the shutdown cooling system, containment cooling system, suppression pool cooling system, and low-pressure coolant injection (LPCI) system. After depressurization of the core, reactor core cooling at low pressure is ensured by the RHR shutdown cooling system.

Once the pressure of the vessel is decreased during the shutdown and cooldown of the reactor, the cooling process is carried out by the RHR shutdown cooling system. Reactor coolant is removed from one of the recirculation lines, and the coolant is then transferred to the RHR heat exchangers. Excess heat is transferred in the heat exchangers to the service water. Through the appropriate connections, the cooled water is injected back into the recirculation lines.

During normal operational conditions, shutdown states, or design-basis accidents, the containment cooling system prevents temperature and pressure rises in the containment. Temperature control of the Suppression Chamber (SC) is important because the pool acts as a heat sink, and a rising temperature causes pressure increases in both the wetwell and drywell. In order to prevent pressure build-up in the containment, water removed from the SC is cooled through the RHR heat exchangers and then returned to the SC through a spray system. In addition, cooled water in the RHR heat exchangers can be used in the drywell by spray spargers to condense the accumulated steam.

The RHR system consists of two trains, and each one has two pumps. Each RHR pump includes its own heat exchanger, related connection piping, and valves. The pumps and motor-operated valves of the RHR require AC power to work, which can be supplied from off-site sources or on-site sources. The basic layout of the systems and connections of the RHR is given below in Figure 2-7.

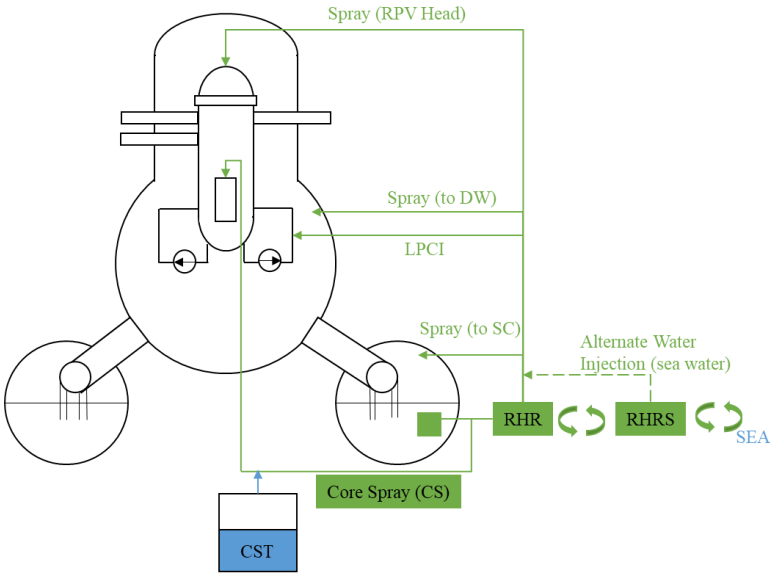


Figure 2-7 General Electric BWR/4 Residual Heat Removal System.

The Emergency Core Cooling Systems (ECCS) are designed to ensure reactor cooling to mitigate or limit fuel cladding failure in case a design-basis accident occurs. If inadequate core cooling occurs, fuel damage and core melting can begin, leading to a beyond-design-basis accident spectrum that includes severe accident transients. The ECCS consists of the High-Pressure Coolant Injection System (HPCI), Automatic Depressurization System (ADS), Core Spray System, and Low-Pressure Coolant Injection (LPCI) System.

The HPCI system provides adequate core cooling during small LOCA transients to maintain cladding and fuel rod integrity. In addition, the core cooling helps to depressurize the RPV, and the reduced pressure allows the low-pressure ECCS systems to be activated to continue core cooling.

The HPCI system is similar to the RCIC shutdown heat removal system; in the event of RCIC failure, the HPCI system can also fulfil the task of heat removal during shutdown. One train of the HPCI system, with 100% capacity for decay heat removal from the core, consists of one turbine, one turbine-driven pump, connecting pipes, and control units. The layout of the system is given in Figure 2-8.

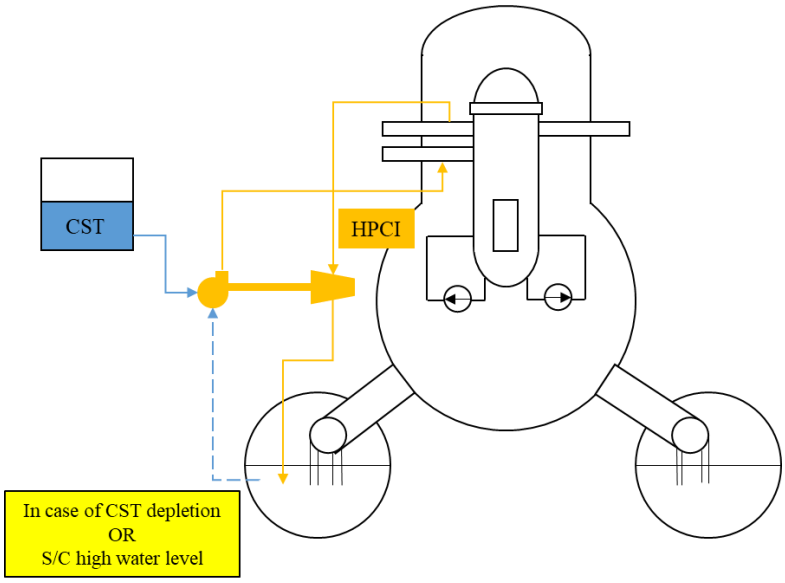


Figure 2-8 General Electric BWR/4 High Pressure Coolant Injection System.

The CST ensures the water intake for the HPCI pump, and pressurized water is introduced through the feedwater line. In case of a reduction of water inventory in the CST storage or a water level increase in the suppression chamber, the water source for the HPCI can be switched from the CST to the suppression chamber.

The HPCI does not require an additional power source to operate. The system turbine, which generates power using steam extracted from the core, is sufficient to operate the system. Only DC power is required to start the system and to control the system valves on the connecting pipes.

The pressure relief system ensures the prevention of over-pressurization of the pressure vessel in order to maintain the integrity of the safety barrier in case of a radioactive material release from the core. The system consists of 11 Safety Relief Valves (SRV) and 3 Safety Valves (SV), which are located on the main steam line before the main steam line isolation valves. The safety relief valve connections are routed to the SC bottom elevations inside the water pool. Steam released through the relief valves is condensed inside the SC pool. The safety valve connections are directed to the open drywell space as an additional safety measure. The connection points of the safety and safety relief valves are shown in Figure 2-9.

Safety relief valves are spring-type valves that have two operation modes: a safety mode and a relief mode. High pressure of the reactor coolant can actuate the safety mode when the pressure set point is exceeded, causing the valve to open and release steam to the SC. In order to perform the relief mode at lower pressures, pressurized nitrogen is directed into nitrogen cylinders controlled by a solenoid valve, and this applied pressure enables the main valve to open to

discharge steam to the SC. In order to actuate the relief mode of the SRVs, DC power to activate the solenoid valves and the availability of a compressed gas supply are required. The activation of the relief mode by operators is also called the Automatic Depressurization System (ADS) function of the SRVs.

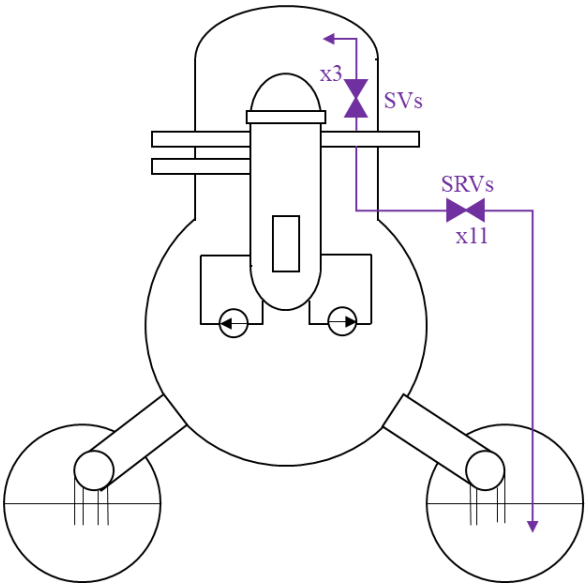


Figure 2-9 General Electric BWR/4 Safety and Safety Relief Valves.

The SRVs of the pressure relief system have both manual and automatic operation. Each valve has a pressure set point which actuates the valve to open when it is reached. The pressure set points of the valves are given in Table 2-1. Relief valves do not have a requirement for AC power to operate; in order to control the valves, DC power is sufficient. In addition to that, operators can manually open the valves, or the automatic system allows them to actuate at lower pressures.

Table 2-1 Pressure Relief System relief valves specifications (Carbajo, 1993).

Valve no.	Bank no.	Opening Pressure (MPa)	Closing Pressure (MPa)	Rated flow (kg/s)	Rated Pressure (MPa)	Rated density (kg/m^3)	ADS
1	1	7.687	7.253	109	7.722	40.8	yes
2	1	7.708	7.101	109	7.722	40.8	yes
3	1	7.722	7.184	109	7.722	40.8	yes
4	1	7.756	6.991	109	7.722	40.8	no
5	2	7.763	7.053	110	7.791	41.2	yes
6	2	7.791	7.322	110	7.791	41.2	yes
7	2	7.797	7.184	110	7.791	41.2	no
8	2	7.825	7.246	110	7.791	41.2	no
9	3	7.846	7.391	111	7.86	41.6	no
10	3	7.86	7.115	111	7.86	41.6	no
11	3	7.867	7.308	111	7.86	41.6	no

In the event of HPCI failure, the ADS function of the pressure relief system performs the RPV depressurization action as a back-up system. The ADS function performs the depressurization action via 5 relief valves. Relief valves of Unit-2 can start steam discharge from main steam line to SC to achieve depressurization function. Low pressure injection systems and sprays can then operate to cool the core.

During a medium or large break LOCA transient, when the RPV pressure has decreased considerably, the Core Spray (CS) system provides water at low pressure to the RPV. Water from the SC is transferred to the reactor core as make-up water. In addition, the water intake could be switched from the SC to the CST in the CS system. The CS is activated by a low water level signal inside the RPV or a high DW pressure with low vessel pressure. In the case of an ADS action during a small break LOCA, the core spray system can be used as well.

The core spray system has two independent loops. Each loop consists of two pumps which have 50% capacity each, connection pipes, motor-operated valves, spargers over the top of the core, and control units. Initiation and operation of the CS system require AC power (electric motors for pumps) and DC power (control valves). The core spray is a branch of the RHR system, and a presentation of the layout is given in Figure 2-10.

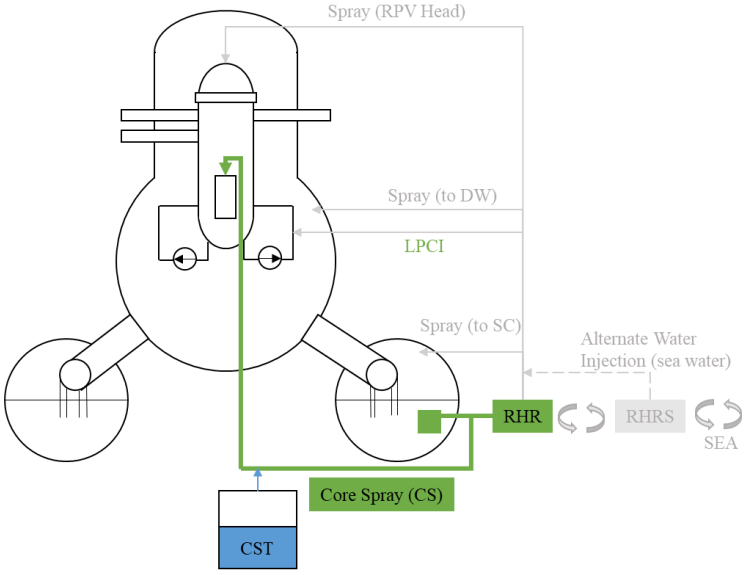


Figure 2-10 General Electric BWR/4 Core Spray System.

Low vessel pressure and high drywell pressure, or a low water level, activates the Low-Pressure Coolant Injection (LPCI) system operation to continue the ECCS long-term cooling action. Low-pressure make-up water is taken from the SC and transferred to the RPV through the recirculation line to provide a sufficient water level inside the core after a LOCA.

In case the pressure level is high after the operation of the HPCI system, depressurization is achieved by the ADS. The LPCI system provides low-pressure, high-flow-rate water injection to the core to maintain the water level at a minimum of two-thirds of the core height. After that, only one system pump is sufficient to maintain the water level.

LPCI is a working mode of the RHR system, which means it is a branch of the RHR system connected to the recirculation line. The two trains of the LPCI system consist of two pumps, each with 33% capacity, connecting pipes, and control valves. The initiation and operation of the LPCI require AC power (pump motors and motor-operated valves) and DC power (control units), as the system itself is a part of the RHR. The system connection and basic representation are given in Figure 2-11.

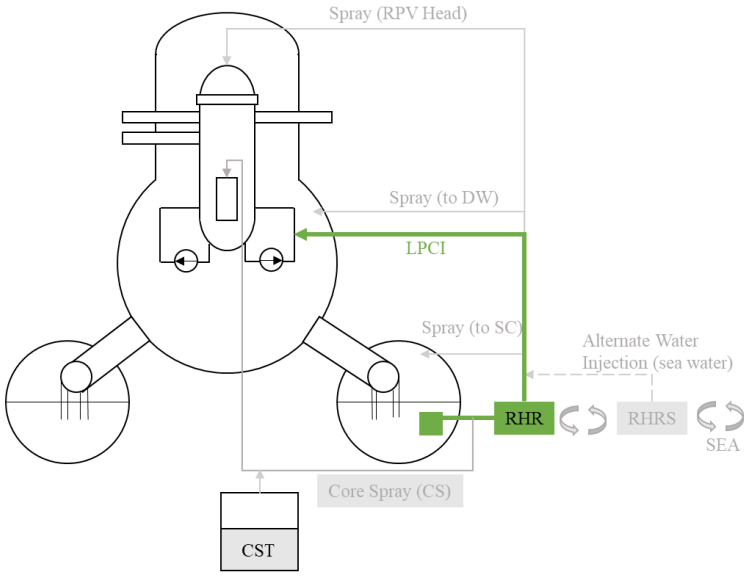


Figure 2-11 General Electric BWR/4 Low Pressure Coolant Injection System.

The BWR/4 design of an NPP consists of two main components in the PCV design. The Drywell, the Suppression Chamber (SC), and the connection between them constitute the total PCV structure. At the time of accident initiation, the main steam isolation valves block the pathway of steam to the turbines, and the safety valves direct the steam flow to the SC. The suppression chamber holds a large amount of water, which helps to condense the extracted steam and decrease its pressure. In addition to that, in case the fuel element integrity is lost, radioisotopes could spread and travel through the flow path. The large water supply of the SC can also be used as a filter for the transported radioisotopes.

In order to manage possible hydrogen accumulation inside the containment section, nitrogen gas is filled inside the PCV. Also, hydrogen catalytic recombiners inside the PCV serve as an

additional hydrogen build-up countermeasure to prevent hydrogen detonations. Maintaining the integrity of the containment of the plant is crucial since the PCV is the last safety barrier after RPV integrity is lost in case of severe accident transients.

A venting system is implemented in the PCV to maintain its integrity by releasing gas outside when gas accumulates and over-pressurizes the inside of the PCV. The containment vent system consists of two pathways to perform the ventilation process. Release from the SC is the preferred pathway because of the filter function of the water supply inside of it, but in case of high-pressure readings in the Drywell, the pathway from the Drywell could also be used. A rupture disk at the end is implemented to prevent premature depressurization.

Even though the PCV is considered the final barrier for the safety of the NPP, the reactor building also has features to help contain any radiological release if the integrity of the containment is lost. The Stand-by Gas Treatment System (SGTS), which is AC powered, filters the air inside the reactor building and keeps the pressure below atmospheric pressure to prevent the release of possible leaks to the outside world. The general layout of the system is given in Figure 2-12.

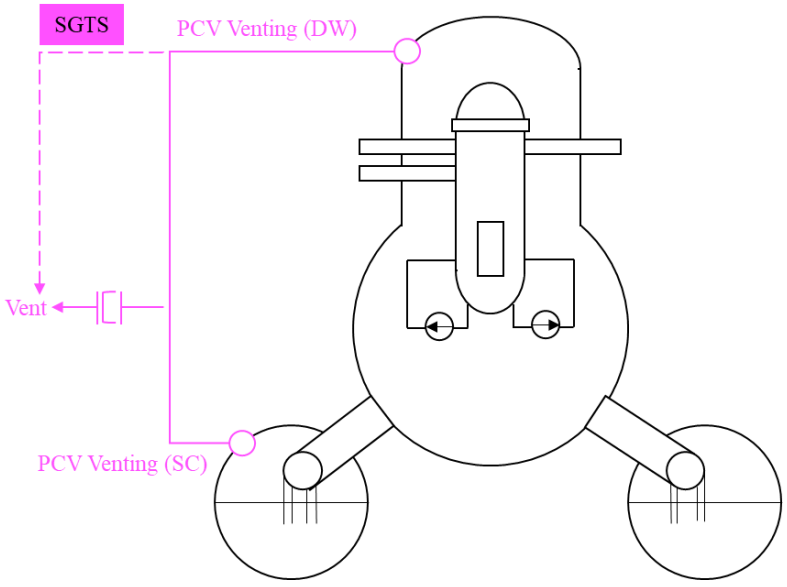


Figure 2-12 General Electric BWR/4 Venting and Stand-by Gas Treatment System.

The complex interaction between these various injection, depressurization, and containment venting systems defines the boundary conditions for any severe accident scenario. In the context of developing an integrated simulation route, accurately modeling the availability, capacities, and

failure thresholds of these specific BWR/4 Mark-1 systems in the ASTEC code are a mandatory prerequisite for generating a realistic radiological source term.

2.2 Key severe accident phenomena in BWRs

The accident progression in a BWR is strongly dependent of the design peculiarities of the whole nuclear power plant i.e., core layout, RPV, water circuit, heat removal systems, containment design, and of the available safety systems. The core loading of BWR consist of a larger number of fuel assemblies than the one of PWR and larger fuel rod diameter and height. In addition, BWR cores consist of absorber blades located in the bypass area between fuel assemblies and channel boxes enclosing the fuel rods and water rods represent additional structures in the core. This structure layout potentially may get oxidized generating hydrogen and additional mass that may melt and start eutectic interactions with the fuel rods during a severe accident.

The imbalance between the heat production and heat removal from the core will start a severe accident progression and rate of the imbalance will determine the timing of failure of the safety barriers. Furthermore, fuel channel boxes prevent cross-flow between fuel assemblies within the active core region, leading to the localized failure of fuel and material structures within the closed fuel channel box region. After the subsequent failure of the core structures depending of their melting point, chemical reactions such as eutectic interactions of molten material with fuel rod cladding (e.g., absorber material) or molten zircaloy (e.g., cladding) with uranium oxide occur leading to molten pools formations and later on relocation to the lower plenum. The control rod drive mechanisms located at the lower part of the core introduce additional material mass to this region that may melt and get mixed with relocated material from the core. The failure of the control rod drive mechanism connections on the lower plenum wall could also represent a unique failure path specific to BWRs. The material composition and local distribution of the molten material in the lower plenum, its mixed thermophysical properties as well as the amount of it, will determine the time and failure mode of the RPV wall driven by chemical, thermal, mechanical, and pressure loads on the inner wall of the RPV lower plenum.

Hereafter, starting of the severe accident event and during the progression of the accident details of material interactions and accident progression during the early in-vessel phase are given (Sehgal, 2012) (Lamarsh and Baratta, 2001).

The failure of the core cooling systems and the subsequent inadequate heat removal from the core mark the starting point of these accidents. Fission products in the fuel material are produced

during plant operation, and their accumulation in the fuel depends on the burnup level. These fission products are responsible for the residual heat generated after reactor shutdown in the form of decay heat and radioactivity in the core. For this reason, the amount of fission products and variations in nuclide isotopes serve as the driving force for the accident progression. Not only decay heat, but also exothermic chemical reactions of metals with steam can lead to increased energy production in the core. The in-vessel core heat up, failure of structures, melting and relocation to the lower plenum depend on the thermohydraulic conditions of the core, the complex geometry, the material heterogeneity, and the chemical interactions; together, these parameters determine the in-vessel accident progression.

Oxidation reactions make a significant contribution to heat production during severe accident conditions in the core. BWR core loading and structures consist of a larger amount of zircaloy and steel material compared to the PWR design, and the resulting hydrogen generation during the oxidation of zircaloy can also threaten the integrity of the containment through potential accumulation and detonation. In order to provide some perspective on the quantities involved, a generic 900 MW PWR contains around 20 tons of zircaloy, compared to a 1300 MW BWR-72 plant, which has around 40 tons of zircaloy in its fuel assemblies. The zircaloy in the fuel channel boxes of a BWR plant adds an additional 35 tons of material. The rate of zircaloy oxidation increases significantly above 1200 °C, and the production of heat results in even higher temperatures where the reaction occurs. Temperature levels can ramp up to the melting point of zircaloy (around 1800 °C) and even up to the fuel melting point (around 2800 °C). Possible limiting factors for the oxidation of zircaloy include steam starvation conditions, local failure and relocation of the cladding to colder sections, and the local formation of hydrogen, which halts the diffusion of oxygen through the cladding.

On the other hand, at lower temperatures, severe accidents in BWRs involve the formation of eutectic mixtures, particularly between control blade materials (steel cladding and boron carbide) and fuel assembly structural components. These eutectic interactions cause solid materials to melt at significantly lower temperatures than their respective individual melting points. This results in the premature relocation of solid structures and the formation of blockages in the lower core regions. Boron carbide (B_4C) is housed within stainless steel tubes inside the control blade wings. Although stainless steel typically melts at 1450 °C and B_4C remains solid up to around 2400 °C, contact between these materials triggers a rapid eutectic reaction starting at around 1150 °C. In BWR fuel assemblies, the zircaloy cladding and fuel channel boxes are in physical contact with stainless steel plates and spacer grids, which may also be made of Inconel. A eutectic reaction between zirconium and iron/nickel can initiate at temperatures as low as 940–980 °C. This dictates the peak temperature of the spacer grids and channel box walls in the early phase. Rather

than heating up to their standard melting points, the materials liquefy and relocate in the early stages of an accident. When the molten B_4C-SS mixture from the failing control blade comes into contact with the zircaloy fuel channel box, secondary eutectic interactions occur. The boron-rich melt attacks the zircaloy wall, accelerating its failure (Hofmann, 1999).

The oxidation of the neutron absorber control element (B_4C material) has an impact on the in-vessel accident progression as well. The energy release and hydrogen production rate of boron carbide oxidation is higher than those of zircaloy oxidation, and the production of CO, CO2, and boron compounds after oxidation also affects the fission product chemistry.

During the heat-up process of the core, the ballooning and rupture of the zircaloy cladding can be observed at around 800-1000 °C. Depending on the core pressure and the oxidation thickness of the cladding, rupture may occur earlier or later. The consequences of this rupture include releasing fission products into the vessel atmosphere and creating possible local blockages in the core due to the fragmentation of the ruptured cladding material.

The oxidation thickness of the zircaloy structure defines its liquefaction and relocation process. The progression of the oxide layer thickness leading up to the melting of the structure can be considered in two categories for zircaloy. In the case of slow temperature increases during severe accidents, such as 0.3 °C/s and lower rates, the formation of a ZrO_2 oxide layer, which has a higher melting point (around 2700 °C), prevents zircaloy melting, and the oxidation reactions continue in place. The ZrO_2 oxide layer that ensures cladding integrity at higher temperature levels results in the formation of a Zr melt between the UO_2 and ZrO_2 material matrix. Molten zircaloy can dissolve the UO_2 and ZrO_2 materials, causing the liquefaction of UO_2 and ZrO_2 at temperatures 1000 °C lower than their standard melting points. After the failure of the ZrO_2 layer, the molten mixture can relocate to the lower sections. During the relocation of this mixture, exposure to the steam atmosphere can contribute to further oxidation since the molten material contains metallic Zr melt.

On the other hand, faster temperature increases, such as those greater than 0.5 °C/s, reach the melting point of the zircaloy and result in material relocation to the lower sections before the formation of a protective ZrO_2 oxide layer. The zircaloy-rich molten mixture that relocates to the lower sections contains a smaller fraction of oxide compared to the slower heat-up case. Being exposed to the steam atmosphere as a metallic Zr-rich molten material during relocation to the lower, colder sections can contribute to rapid oxidation and hydrogen generation as well. This concludes that not only the capability of heat extraction, but also how fast the heat is produced, is one of the key elements defining accident progression.

The freezing of the molten mixture and the formation of blockages can be observed after the molten mixture comes into contact with colder sections close to the water level. The molten mixture that accumulates at the lower sections of the core results in large blockages, and relocated molten materials and mixtures pile up over the clogged sections. The freezing of the melt may result in the development of a surrounding crust region. This solid crust layer keeps the molten mixture contained as a pool in the inner sections. In the absence of water and cooling capability, the molten pool can extend beyond the border of the reactor core. Due to the limitation of heat extraction from the melt caused by the surrounding crust layer, alongside a weakened flow path in the core, the melt relocation moves downward to the lower plenum even if the water inventory in the core is above the top of the active fuel. The presence of cooling water may change the progression and timing of this molten material movement.

After the failure of the surrounding crust layer, the molten material relocates to the lower plenum. Molten material movement to the lower plenum opens another chapter in the severe accident progression, since the last barrier of the pressure vessel is the lower head wall itself. Corium in the lower plenum, which contains fission products and their respective decay heat, has the potential to attack and generate a breach on the lower head wall. Accident progression and lower head failure depend on the material composition in the molten mixture, the relocation timing to the lower plenum, and complex chemical interactions between the structures. The general composition of the materials that relocate to the lower plenum consists of a liquid layer of oxides (UO_2, ZrO_2), metallic forms, and solid debris forms of oxides and metals. Metallic structures are introduced into the molten material as a consequence of the degradation of the structural material around the fuel.

After the interaction of the molten material with the residual water inventory in the lower plenum, the cool-down of the oxide layer starts. Since the melting points of the metallic structures are below the solidus temperature of the oxide, the formation of a crust begins around the oxide pool. The crust layer starts to thicken at the hemispherical part of the molten pool where the pool has contact with the vessel wall. The crust layer around the oxide pool has a weak capability for heat transfer compared to the liquid melt mixture. For this reason, the temperature gradient in the pool initiates natural circulation due to the inhomogeneous crust layer and heat flux. This natural convection and movement mean that the heat fluxes around the periphery of the crust are not homogenously distributed. The highest heat fluxes are expected at the top of the pool, while the peripheral sections of the pool experience heat fluxes that are lower compared to the top section. Half of the residual power is transmitted upward, and the other half is distributed to the hemispherical part of the pool.

The separation of the metallic layer from the oxide pool is also observed at the top, since the density of the metallic mixture is lower than that of the heavy metals and oxides. In such a situation, the metallic layer receives half of the residual power from the oxide pool and transfers it to the water inventory in the lower plenum. In the event of the depletion of the water source in the lower head, heat is transferred to the vessel through the contact zone between the metal layer and the vessel wall. Depending on the metallic layer's thickness, the heat flux can be greater, since the flux is inversely proportional to the thickness of the layer, which relates to the heat transfer area. A higher heat flux resulting from a thinner metallic layer sitting above the oxide pool threatens the integrity of the vessel wall, and this phenomenon is called the focusing effect.

In order to extract the heat through the metallic layer and cool down the molten material inside the lower head, external cooling from outside the lower head may be considered. The efforts regarding In-Vessel Melt Retention (IVMR) strategies and the modelling of this physical phenomenon have been extensively studied (Carénini, Fichot and Seignour, 2018). In the case of external heating, the critical heat flux is also a point that needs to be avoided to achieve effective cooling.

The last step of the in-vessel accident progression is the loss of integrity of the lower head and the movement of molten material outside of the vessel. The presence of corium in the lower plenum and its residual power creates a pressure increase and heat load that leads to creep formation on the vessel wall. Depending on the magnitude of the thermal loads, which are dependent on the layer depths of the molten materials in the hemispherical volume, the creep process and failure time may vary, as the cylindrical part of the pressure vessel structure is less durable to these loads compared to the hemispherical part. For this reason, a larger amount of molten material and a higher axial location of thermal loads present a higher potential to conclude in vessel failure.

After vessel failure, the accumulated molten material and fission products transfer to the cavity space below the pressure vessel. The Molten Core-Concrete Interaction (MCCI), which is the chemical interaction between the molten material and the concrete in the structure, results in further hydrogen generation and structural ablation. In the event of a breach in the final containment barrier, fission products will be released from the plant into the environment.

2.3 Key radiological dispersion phenomena following a severe accident

The release of fission products into the environment jeopardizes the safety of the population and the surrounding ecosystem. Depending on the amount and duration of the release, evacuation and long-term mitigation measures may be required around the plant. Following the Fukushima NPP accidents, benchmark studies focused on the severe accidents to investigate the progression within the plant (OECD and Nuclear Energy Agency, 2021). Because of the station blackout after the earthquake and tsunami, there was no reliable information available for the operators in the control room, meaning the operation of the plant was carried out blindly. As a result, attempts to restore core cooling were unsuccessful, and initial damage to the reactors and releases to the environment were observed in Unit 1. The release of steam, hydrogen, and fission products led to pressure build-up and the subsequent failure of the head flange in the PCV. The final investigation showed that 80 percent of the initial core inventory of 154 kg of the Cesium element and 12 kg of the Iodine element was released into the environment. Understanding the mechanisms of how such major releases are dispersed through the atmosphere around the site is essential for assessing and mitigating public risk.

When a radiological release from a NPP after a core melt accident occurs, the released radioisotopes travel through the environment dictated by local weather conditions. Wind direction and speed, atmospheric stability, and precipitation rates play crucial roles in the transport of the radiological plume. The settling of particles on surfaces driven by precipitation causes wet deposition, which can result in the accumulation of radioisotopes and significantly higher local contamination rates. Conversely, heavy precipitation may also wash radioisotopes off surfaces and into the surrounding soil. In the absence of precipitation, surface roughness and wind speed act as driving forces for dry deposition, spreading radioisotope contamination over surfaces and soils.

The population can receive radiation doses from "cloud shine" (external exposure from the passing radioactive cloud) or "ground shine" (external exposure from radioisotopes deposited on the ground). Particles deposited directly on human skin cause further external doses, while human activity may cause the resuspension and subsequent transfer of radioactive dust. Furthermore, the inhalation and ingestion of this radioactive dust result in internal exposure.

Contamination of agricultural products constitutes another pathway for radioisotope intake by the public. Plants and fields located along the passage of the radioactive plume can become contaminated, and certain isotopes, such as cesium, can be absorbed directly into the plant system through its leaves. In addition to this foliar uptake, plant roots can absorb contaminated water and

soil from underground depositions. Moreover, dairy and farm animals can receive contamination directly from the plume or indirectly through the consumption of contaminated feed, allowing the radioactivity to be transferred into milk and meat products.

Upon the detection of radioactive dispersion by monitoring systems located around the nuclear power plant, responsible emergency teams initiate immediate actions to protect the public from high radiation doses during the early phase of the release. First, the evacuation of planned regions and contaminated areas is initiated, and sheltering is ordered for parts of the population to protect them from cloud shine and inhalation doses. The distribution of iodine tablets to prevent the thyroid uptake of radioactive iodine is also executed. In the long term, once the radioactive release stops and contaminated areas are delineated, soil remediation and shielding precautions can be implemented. The decontamination of facilities and the removal of contaminated grass and vegetation serve as complementary actions to prevent long-term health effects and public exposure.

The decisions of the emergency teams are based on measurements and information (timing, expected dose) about the radiological consequences of severe accidents that only dedicated computer codes can predict. In addition, optimal countermeasures to mitigate the consequences initiated by the emergency teams are based on predictive radiological dispersion tools demonstrating their central role on protecting people and environment in case of severe accidents with radiological consequences.

2.4 Validation of severe accident codes

Severe accident analysis codes like ASTEC rely heavily on validation against separate-effect and integral-effect tests to ensure the appropriateness of their computational models. Historically, the continuous development and validation of the ASTEC integral code have been predominantly focused on PWR design. The most recent validation matrix for the ASTEC V2.2 version is extensive, comprising over 300 experimental tests conducted at various scales in more than 50 different facilities worldwide (Chatelard and Laborde, 2023). However, only part of the validation work done for PWR models e.g., the oxidation and degradation of fuel rods is applicable to BWRs.

Unlike PWRs, BWR fuel assemblies are enclosed in zircaloy channel boxes. These channel boxes prevent cross-flow in the active core region and act as pathways for relocating molten cladding (Gauntt, Gasser and Ott, 1989). Furthermore, the oxidation of the B_4C used in BWR control blades is highly exothermic and has the potential to induce early melt relocation. Boron

carbide oxidation produces significantly more hydrogen per unit mass than zircaloy and generates CO and CO_2 that heavily influence fission product chemistry. Additionally, eutectic interactions between B_4C-Fe, B_4C-Zr, and Fe-Zr occur between 1200–1500 °C, leading to the liquefaction and relocation of solid structures well below the melting point of the fuel itself.

To address these distinct phenomena, the ASTEC V2.2 version introduced new core degradation models specifically designed to cope with BWR canister and sub-channel configurations. Despite these modelling advancements, the experimental database used to validate these specific BWR features remains limited compared to the robust PWR matrix. The assessment of early-phase degradation in a BWR core geometry relies almost exclusively on the QUENCH-20 integral experiment.

In this dissertation, the validation of the BWR related models implemented in ASTEC focus on the early in-vessel phase will be done with the QUENCH-20 BWR experiment that combines a prototypic BWR geometry with B_4C control blade, channel box, and water rod degradation. The focus of this validation is on fundamental phenomena like oxidation of overheated structures including the BWR-specific ones, heat transfer phenomena, eutectic-interactions, molten material formation and relocation during the early in-vessel phase. Since severe accident progression is driven by local interactions e.g., B_4C oxidation, eutectic liquefaction, validating the ASTEC code against QUENCH-20 ensures that the fundamental source terms of heat and hydrogen generated during the accident progression are correctly calculated by the ASTEC models at the bundle level and so at core level.

By demonstrating a good performance of ASTEC in prediction of the BWR bundle behaviour in QUENCH-20 test, subsequent application if ASTEC to simulate severe accident sequences in full scale BWR is justified. This phenomenological validation forms a critical scientific bridge, ensuring that the source term generated for the environmental risk assessment is done used at least partly validated codes. In the following chapter, the validation of ASTEC BWR-related models for the early in-vessel phase of severe accidents will be presented and using the QUENCH-20 experimental data.

3 Design of a First-of-the-kind Computational Route for the Prediction of Radiological Consequences after Severe Accidents in BWRs

3.1 Introduction

The ultimate objective of nuclear reactor safety analysis is the protection of the public and the environment from the consequences of potential severe accidents. In order to achieve this, it is not sufficient to merely evaluate the thermal-hydraulic and physical degradation of the reactor core and containment structures. A comprehensive assessment must quantify the actual radiological impact on the surrounding population. Therefore, an end-to-end computational route is required. This integrated sequence requires three fundamental pillars: a burnup analysis code to determine the initial nuclide inventory within the fuel, an integral severe accident simulation tool to describe the severe accident progression and calculate the time-dependent radiological source term released to the environment and atmospheric dispersion analysis tool to translate this released source term into public dose metrics.

Historically, many safety evaluations stop at the determination of the source term. However, without the final radiological dispersion phase, a severe accident analysis remains fundamentally incomplete and without practical importance for emergency teams. Only the mass of released fission products does not provide the necessary context to draw meaningful conclusions regarding public safety, evacuation zoning, or long-term environmental habitability.

Furthermore, while comprehensive computational chains have been explored for other reactor technologies, a continuous, integrated computational route specifically tailored for BWR designs is currently missing. Addressing this critical gap, this chapter establishes a first-of-a-kind computational methodology by sequentially coupling the ORIGEN/CASMO5 inventory codes, the ASTEC severe accident evaluation code, and the JRODOS decision support system. Doing so, development of an end-to-end computational route capable of predicting the full spectrum of severe accident sequences and their radiological consequences for modern BWRs is envisaged.

As established in the previous sections, assessing the environmental and public impact of a severe accident requires a seamless translation of in-vessel degradation physics into ex-vessel phenomena in the containment as well as containment failure modes (release paths) so that finally reliable radiological dispersion data can be estimated. To achieve this, a deterministic computational chain must be constructed. This chain must accurately predict the nuclide inventory based on specific fuel burnup, simulate the transient thermohydraulic and degradation behavior of the NPP, track the fission product release into the containment, and finally, model the

atmospheric dispersion of these radioactive substances. Prediction this complex, multi-physics and multi-scale phenomena taking place during multiple severe accident sequences of specific nuclear power plants requires the combination and coupling of highly specialized computer codes. In this doctoral thesis, the following computational tools were selected to form the backbone of the integrated computational route to be developed

3.2 Key elements of the computational route

In order to perform a comprehensive severe accident analysis, starting from the initial radionuclide inventory calculation and ending with the radiological dispersion analysis for public safety assessment, a complete computational route was established. This route chains three major codes together: CASMO5 (or ORIGEN), ASTEC, and JRODOS. To ensure that these codes can communicate with each other, dedicated Python scripts were developed to act as data interfaces. These scripts automatically convert the output data of one program into the specific input format required by the next. In this way, the codes and their outputs are chained together to expand the frame of the severe accident analysis.

The first step of the computational route is the determination of the initial core inventory. The CASMO5 code uses the core geometry, material composition, and power information to perform a burnup analysis of the fuel assemblies, generating a detailed isotope inventory provided in the dimension of atomic density (atoms per cm^3). To bridge the gap between the tools, a dedicated Python script extracts this atomic density information and converts it into a suitable format for the ASTEC input deck. This formatted data is passed to ASTEC to define the initial radionuclide information in the core. ASTEC relies on this realistic isotope data to accurately calculate the decay heat production, which drives the accident progression, and to determine the available source term in the core before degradation begins.

Using the realistic inventory provided by this first data transfer, ASTEC performs the severe accident analysis, calculating the core meltdown, the failure of the reactor pressure vessel, and the transport of materials into the containment. Ultimately, ASTEC produces the time-dependent released isotopes to the environment in the format of mass (kilograms). However, the radiological dispersion code, JRODOS, can not directly use mass information; it requires the source term to be defined as radiological activity and divided into specific time step windows. A second Python script was created to resolve this incompatibility. This script takes the time-dependent mass output from ASTEC, applies the specific half-lives of each isotope to convert the mass into activity (Becquerel), and organizes the data into the defined time step windows. This creates an input deck fully compatible with JRODOS, which then utilizes the dynamic activity data to simulate

atmospheric dispersion and assess public safety. Total computational chain from starting to end is given in Figure 3-1.

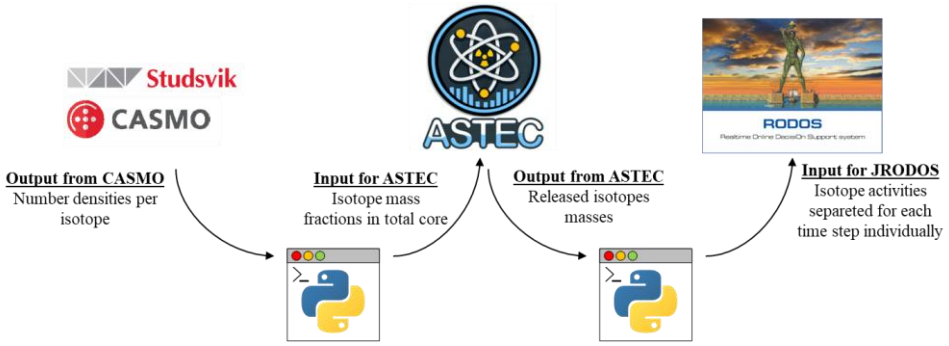


Figure 3-1 Computational route starting from nuclide inventory calculation to radiological dispersion analysis.

This integrated computational route offers significant advantages over the traditional decoupled approach, which often relies on manual data manipulation, simplified assumptions like lumped release fractions, or generic decay heat curves rather than real burnup data. By linking CASMO5, ASTEC, and JRODOS through automated interfaces, the continuous, time-dependent nature of the accident is preserved. The specific operational history of the fuel is carried over automatically into the severe accident progression and ultimately into the environmental consequence analysis with high fidelity and without manual transfer errors. Furthermore, this automation allows JRODOS to process a dynamic, time-dependent release profile rather than a static release, leading to highly realistic plume dispersion mapping. Ultimately, instead of analyzing core physics, plant degradation, and public evacuation zones as isolated problems, this expanded computational route evaluates them as a single connected sequence, providing a highly reliable information database for emergency response teams.

3.2.1 Tools for the nuclide inventory prediction of the core loading: ORIGEN, CASMO5

ORIGEN module of the SCALE code system is responsible for fuel inventory and burnup calculations of the nuclear power plant core from the fuel rod to the fuel assembly scale (Wieselquist, Lefebvre and Jessee, 2020). Problem dependent cross sections can be utilized for each specific problem and interpolated libraries can be constructed depend on the problem requirements. At the foundation of the code Bateman rate equations are taken into account in order to determine the isotope fractions in the defined volume after undergo fission, decay or transmutation.

CASMO5 code is an advanced two-dimensional transport code capable to predict the depletion of core loadings at fuel assembly and pin level (Hykes, Ferrer and Rhodes, 2022). Compared to ORIGEN, it can handle heterogeneous core configurations of modern core loading with burnable absorbers in different configurations. It employs a multigroup energy discretization and features a comprehensive nuclear data library. The prediction of the change in time of the nuclide inventory in the core during operation at any cycle, Bateman equation is solved using predictor-corrector approach.

3.2.2 Integral severe accident code: ASTEC

The Accident Source Term Evaluation Code (ASTEC) is the European reference severe accident code developed by ASNR (Chatelard *et al.*, 2016) for the analysis of the severe accident sequences in Light Water Reactors (LWRs) including the release of fission products in the core and their transport into the environment. Similar to the ASTEC, there are codes with capabilities for conducting severe accident analyses, such as MELCOR (Humphries *et al.*, 2017), MAAP (ERIN Engineering and Research, Inc., 2010), AC2 (Wielenberg *et al.*, 2019) which are also used in practice.

For a realistic prediction of the release and transport of the fission products from the core into the environment, ASTEC needs the initial nuclide inventory for a realistic core loading considering the most relevant burnup state of the core from the risk perspective. These key-data is provided by CAMOS5 or ORIGEN. Then a realistic material composition of the core loading can be considered in ASTEC when predicting the severe accident progression.

As the code is developed according to the needs of the French NPP fleet, which consists only of PWR design, the capability and development of the code is mainly focused on the PWR design direction. After the Fukushima severe accidents ASNR started to extend the ASTEC model capabilities for BWR structures as well, such as fuel channel boxes, absorber crosses and water rods in order to simulate their behavior during the in-vessel phase of severe accidents. The main reason for the selection of the ASTEC is the need for validation of the recently implemented BWR related models using experimental data available at KIT (Steinbrück, 2019) as well as to apply the partly validated code to simulate BWR severe accident sequences with the focus on the radiological source term prediction and its dispersion around the NPP as the ultimate goal. The ASTEC modular structure and mechanistic simulation approach allow a detailed representation and simulation of different LWR-designs and severe accident sequences.

3.2.3 Tool for the prediction of dispersion of radioactive isotopes: JRODOS

Java based Real-time Online Decision Support code (JRODOS) (Ievdin *et al.*, 2010), developed at the Karlsruhe Institute of Technology, is a versatile tool for the estimation of dispersion of the radioactive isotopes released from a NPP after a severe accident with core meltdown. Radiological source term predicted by the integral severe accident codes like ASTEC for a specific severe accident sequence is needed in the proper format and time series. Based on the obtained results from the dispersion analysis; assessment of the emergency response activities, description of the evacuation zones, determination of the short- and long-term effects of the radioactive isotopes on the members of the public can be accomplished.

JRODOS decision support system uses connected modules which are Local Scale Model Chain (LSMC) for near locations and MATCH module for far range dispersion calculations. The module EMERSIM simulates early emergency countermeasures and DEPOM module deals with environmental deposition calculations. Besides the DEPOM, FDMT module also includes food chain and dose evaluations based on that. The core of the dispersion calculations handled with LSMC and included atmospheric models such as RIMPUFF, DIPCOT and LASAT which simulates radioactive plume movement using meteorological data like wind speed, wind direction, atmospheric stability and precipitation. Transport of the plume calculated by solving advection-diffusion equations where wind fields drive the material on the wind direction (advection) and atmospheric turbulences causes the plume spread outwards (diffusion).

4 Validation of ASTEC Using QUENCH-20 BWR Test

4.1 Introduction

In order to establish the integrated computational route proposed in this thesis, it is first necessary to ensure the reliability of the severe accident code (ASTEC). Before predicting a radiological source term for environmental dispersion, the core degradation models must be validated against representative experimental data.

The QUENCH-20 experiment was selected because it specifically investigates a BWR type fuel assembly behavior under severe accident conditions, including the unique B_4C control blades, channel box and water rods. This chapter details the ASTEC modeling of the QUENCH-20 test and evaluates its prediction accuracy. Validating the code at this experimental scale provides the scientific justification and confidence needed to broaden the analysis to a full-scale nuclear power plant in the subsequent chapters.

4.2 The QUENCH-20 BWR test description

The QUENCH facility test section is housed within an Argon-filled containment vessel, which has a height of 2.9 m and a diameter of approximately 800 mm. Connections for the applied DC power are placed at the top and bottom sections of the containment. Steam and argon (Ar) injection channels, as well as quenching tubes, are located at the bottom of the test bundle. The injected steam, carrier Ar gas, and the produced hydrogen during the oxidation of hot structures pass through the test bundle and exit via the exhaust tube at the top. The hydrogen generated during the test is measured using two different systems: the Balzers "GAM 300" mass spectrometer located at the off-gas pipe, and the "Caldos 7G" hydrogen detection system located at the condenser section, to which the off-gas pipeline is connected. After the steam is separated from the non-condensable gases (argon and hydrogen), condensation takes place, and the resulting water is delivered to a storage tank. Additionally, there is an emergency cooling circuit, an off-gas pipe cooling system at the top, and a water-cooling system at the bottom. The general layout of the QUENCH facility test section is illustrated in Figure 4-1.

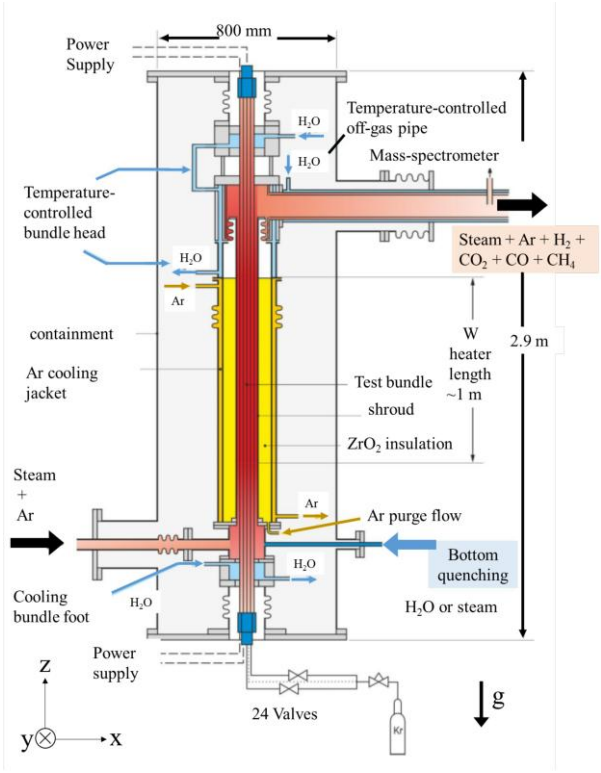


Figure 4-1 QUENCH Facility test section (Stuckert *et al.*, 2005).

The test section is equipped with several measurement devices to monitor the temperature, pressure and mass flow of the fluid as well as the temperature of the bundle components e.g. fuel rod simulators, shroud, at different axial and radial positions for code validation. The numbering and elevation points of the thermocouples are indicated in Figure 4-2.

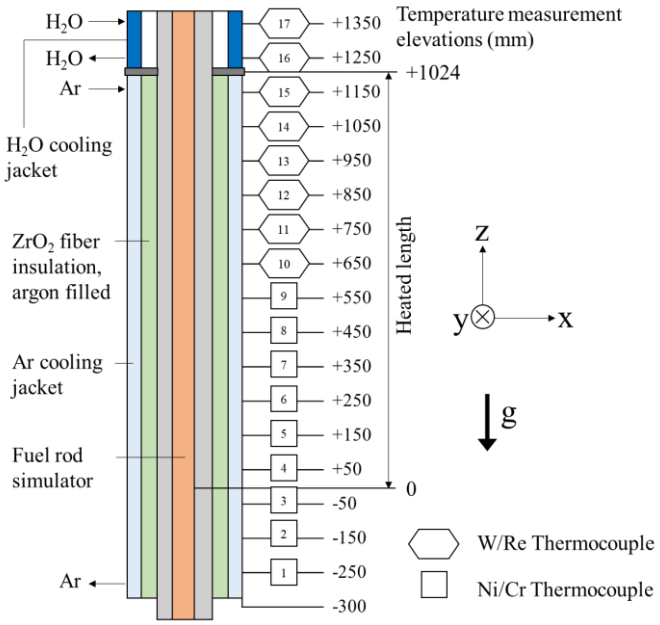


Figure 4-2 Thermocouple axial locations alongside the QUENCH test section (Stuckert *et al.*, 2005).

4.2.1 **BWR test bundle**

The selected BWR fuel assembly type for the QUENCH-20 test is SVEA-96 Optima-2. Because of the size limitations in the test facility, only one quarter of the fuel assembly was tested. The presence of fuel channel boxes, water rods and enveloped with cross shaped control blades is a specific design feature of a BWR core; this unique material mass and geometrical placement make the design critical to analyze in terms of degradation during severe accident progression. For this reason, it must be emphasized that conducting this test and its subsequent simulation are essential to investigate the applicability of ASTEC for BWR designs. The shape of the assembly and the selected test section are shown in Figure 4-3.

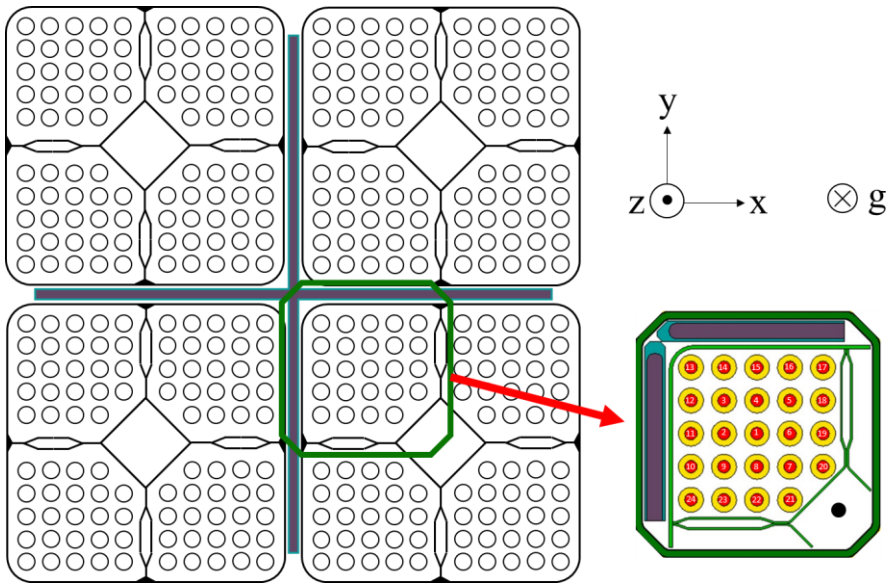


Figure 4-3 SVEA-96 Optima-2 BWR fuel assemblies arrangement and selected quarter of the assembly for the QUENCH-20 test (Steinbrück, 2019).

DC power connections are provided through the top and bottom contact points. Two heated fuel rod simulator groups were utilized during the test and their corresponding divisions are given in Figure 4-4 at the right. Total 24 electrically heated rods have 1024 mm tungsten section in the middle. A molybdenum electrode is located at the top of the tungsten part. At the bottom of the tungsten section molybdenum and copper parts are placed. The axial divisions of the heated rods within the test bundle are illustrated in Figure 4-5. The annular pellets around the heated section are made of ZrO_2 and the surrounding cladding is Zircalloy-2. In order to keep the rods in position five Inconel X750 spacer grids are distributed throughout the assembly. The fuel channel box is made of ZIRLO and it creates a sub-channel for the fuel rods and separates the heated water from the bypass flow. In order to track the oxidation process and oxide thickness along the rods one Zircaloy corner rod is placed at the corner of the test assembly. The control blades are represented by the two stainless steel blade parts which hold the neutron absorber, boron carbides. A

zirconium shroud encloses the test bundle at the outermost section. Thermal insulation made of ZrO_2 material is placed around the shroud, and an Inconel cooling jacket surrounds the bundle and insulation layer. An argon (Ar) flow is maintained within the cooling jacket. The dimensions of the test section and the design characteristics of the QUENCH-20 test bundle are summarized in Table 4-1.

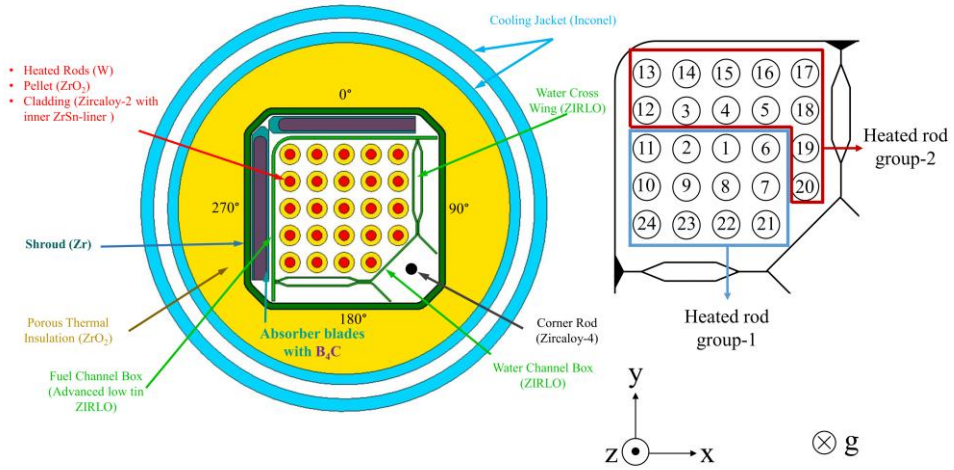


Figure 4-4 Cross section of the test bundle of QUENCH-20 (left) and heated rod groups of the bundle (right) (Murat *et al.*, 2020).

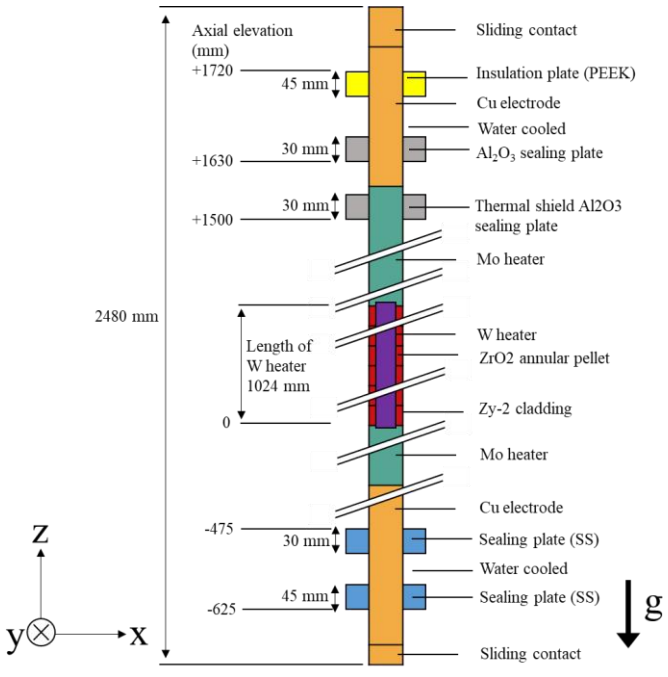


Figure 4-5 Heated rod simulator of QUENCH test bundle (Stuckert *et al.*, 2005).

Table 4-1 Design characteristics of QUENCH-20 test bundle (Steinbrück, 2019).

Bundle type		BWR ¼ SVEA-96 OPTIMA2
Bundle size (# of rods)		25
Number of heated rods		24
Bundle pitch		12.898 mm
Cladding outer diameter		9.84 mm
Cladding thickness		0.605 mm
Cladding material		Zircaloy-2 with ZrSn liner
Rod length		2480 mm
Heater material		tungsten (W)
Heater length		1024 mm
Heater outside diameter		5.25 mm
Annular pellet	material	ZrO_2
	internal diameter	5.45 mm
	outside diameter	8.48 mm
	length	11 mm
Corner rod	material	Zircaloy-4
	outside diameter	6 mm
	length	2505 mm
Fuel Channel Box	material	Zirlo
	length	1560 mm
Shroud	material	Zircaloy-4
	distance between inner wall surfaces of the long shroud sides	90 mm
	distance between inner wall surfaces of the short shroud sides	114 mm
	wall thickness	3 mm
	length	1600 mm
Shroud insulation	material	ZrO_2 fiber
Absorber blades	material	B_4C covered with stainless steel
	thickness	8.05 mm
	width	73 mm
	length	1560 mm
	diameter of B_4C rods	6 mm
	rod pitch of B_4C rods	8 mm
Grid spacer	material	Inconel X750
	locations	-200 mm
		50 mm
		550 mm
		1050 mm
		1410 mm
Cooling jacket	material	Inconel
	Inner tube inside diameter	158.3 mm
	inner tube outside diameter	168.3 mm
	outer tube inside diameter	181.7 mm
	outer tube outside diameter	193.7 mm

4.2.2 **The QUENCH-20 BWR test conduction**

The experimental progression of the QUENCH-20 test is divided into three distinct phases: pre-oxidation, transient, and quench. These phases are defined based on the applied electrical power and the injection rates of the inlet gases and water. First, the pre-oxidation phase started with a 3 g/s Ar and 3 g/s steam injection from the bottom of the test bundle. The electrical power was gradually increased to approximately 7.5 kW over the first 2290 seconds. This power level was maintained up to 14400 seconds, marking the end of the pre-oxidation phase. At this point, the corner rod was withdrawn from the test bundle. Subsequently, the transient phase began, during which an electrical power increase from 7.5 kW to approximately 18.2 kW was applied between 14400 seconds and 15890 seconds. A rapid increase in both power and bundle temperature was observed during this phase. Finally, at 15890 seconds, the quench phase was initiated. The steam injection was stopped, and a 50 g/s quench water injection was actuated from the bottom. The temperature of the injected quench water was approximately 22 °C. The power level was decreased sharply from 18.2 kW to 3.5 kW at the beginning of this phase. Over the following 1000 seconds, the quench water injection continued while the power was gradually decreased to zero. After this, the insertion of quench water was stopped, and only the argon injection was maintained. A schematic of these phases, along with the corresponding flow inlets and power levels, is given in Figure 4-6.

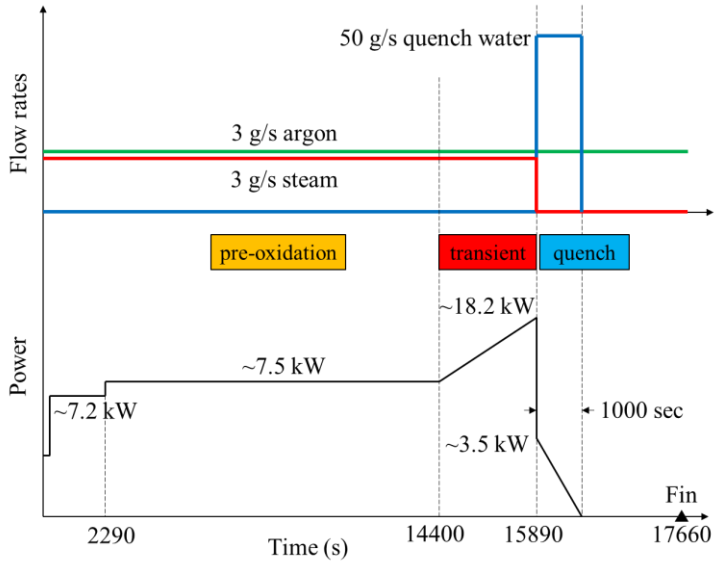


Figure 4-6 Electrical power, intake flow rates of the QUENCH-20 experiment (Murat *et al.*, 2020).

4.3 Development of an ASTEC-model for QUENCH-20 BWR test

The QUENCH-20 experiment was modelled using ASTEC version 2.2b, developed by IRSN. This version contains models for the oxidation, melting, melt relocation, and eutectic interaction of BWR core components such as fuel channel boxes, absorber crosses, and water rods which were recently implemented and are not yet fully validated (Chatelard *et al.*, 2016). In this work, the ICARE and CESAR modules of ASTEC were used to represent the bundle's main components and their internal thermal-hydraulic flows, as well as the chemical interactions, degradation processes, and material relocations that occurred during the experimental transient.

4.3.1 Test section model

The flow area inside the fuel channel box is divided radially into three rings, with 1, 8, and 15 representative heated rods placed in each respective channel. From the innermost to the outermost, these channels are named “Channel-1”, “Channel-2”, and “Channel-3”. A separate channel, designated as “CORE”, is defined between the fuel channel box and the shroud to represent the bypass flow around the fuel channel box, the water channel box, and the cross-wing control rod. Since the modelling capability of ASTEC only accommodates cylindrical objects, one solid cylindrical object is defined to represent the fuel channel box, the water channel box, and the cross wings collectively. An insulator structure is placed around the shroud, and an Inconel cooling jacket is located at the outermost region. The radial dimensions of the channels and structures are given in Table 4-2.

Table 4-2 Radial dimensions of ASTEC model of QUENCH-20 test bundle.

Radius of Channel-1	7.277 mm
Radius of Channel-2	21.83 mm
Radius of Channel-3	36.83 mm
Inner diameter of fuel channel box	73.66 mm
Outer diameter of fuel channel box	76.46 mm
Inner diameter of Zr shroud	100.44 mm
Outer diameter of Zr shroud	106.44 mm
Inner diameter of inconel cooling jacket	158.30 mm
Outer diameter of inconel cooling jacket	168.30 mm

The absorber blade structures were placed in the “CORE” channel as cylindrical structures because the available physical interaction models in ASTEC are restricted to cylindrical geometries. In order to accurately represent the control blades in terms of mass and heat transfer area, two distinct cylindrical structures were defined. The first structure contains only stainless

steel with a weighting factor of 2, while the other cylindrical object includes boron carbide with a stainless steel cladding and is assigned a weighting factor of 10.

Table 4-3 Heated rod and control rod model specifications in ASTEC model of QUENCH-20 test bundle.

Heated Rods	
Diameter of Mo and Cu	7.85 mm
Diameter of tungsten	5.25 mm
Clad inside diameter	8.63 mm
Clad outside diameter	9.84 mm
Dimensions of ZrO_2 pellet	8.25 mm outside dia. (from -0.475 to 0 m) 8.48 mm outside dia. (0 to 1.024 m) 8.25 mm outside dia. (1.024 to 1.5 m)
Kr gas pressure between ZrO_2 and cladding	5 bars
Control Rods	
Diameter of stainless steel only rods	18.75 mm
Diameter of boron carbide inner part of B_4C + SS rods	6.907 mm
Diameter of stainless-steel outer part of B_4C + SS rods	8.907 mm

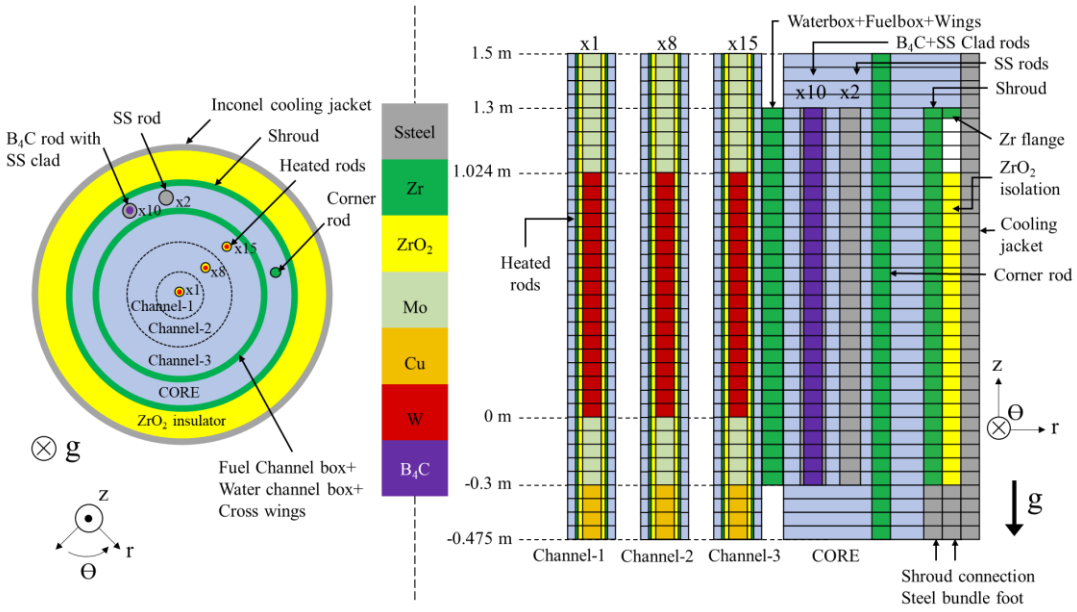


Figure 4-7 Radial (left) and axial (right) cross section of ASTEC model of the QUENCH-20 test bundle (Murat *et al.*, 2020).

4.3.2 Initial and boundary conditions

The time-dependent boundary conditions derived from the QUENCH-20 experiment description were utilized in the ASTEC simulation. First, the electrical power supplied to all 24 electrically heated rods was defined individually, taking their specific heating groups into account. Additionally, the test pressure measured at the outlet of the bundle was applied as a pressure boundary condition. At the inlet of the model, the temperature and mass flow rates of the injected superheated steam and argon carrier gas were specified. Furthermore, the specific quench water temperature and flow rate during the quench phase of the test were incorporated. Finally, the time-dependent temperature at the outer surface of the cooling jacket, along its axial height, was prescribed for the enclosing medium exactly as measured during the experimental transient.

4.3.3 Selected ASTEC-models relevant for early in-vessel phase of severe accidents

Thermal conductive heat transfer within the structures was activated using the COND model in the ICARE module. The GAP model in ICARE addresses the heat transfer across the gap formed between the cladding and the ZrO2 pellets. Convective heat transfer was activated using the CONV model, which was applied to all structure surfaces in contact with the fluid flow. Finally, radiative heat transfer was defined using the RADB module. The specific models and their corresponding structures are summarized in Table 4-4.

The fuel bundles, enclosed by the fuel channel box and the shroud, create a highly complex geometry for radiative heat exchange. In this environment, the emissivity and view factors of the heated surfaces play a major role in radial radiative heat losses. Within the RADB model, the positions of the heated fuel rods, along with their weighting factors, were defined using 2D Cartesian coordinates. To better approximate the radiative heat transfer inside the test bundle, anisotropic factors for the surface structures were also considered. Because the geometric arrangement of the QUENCH-20 test bundle precludes the assumption of isotropic radiative heat transfer, recommended anisotropic factors were employed in the model. Specifically, an anisotropic factor of 0.5 was selected for the rods, and 0.15 was selected for the shroud and fuel channel box in this study (Tien *et al.*, 1979).

Table 4-4 Described heat exchanges models in ASTEC model of QUENCH-20 experiment.

COND, CONDAUTO	• Electrical heated part and ZrO_2 material, cladding of heated rods, corner rod, water channel box, absorber rods, cladding of absorber rods, zirconium shroud, ZrO_2 isolation, Ar cooling jacket, top part of cooling jacket (water cooling jacket), lower part entrance and bottom seal plate. • Between upper face of Ar cooling jacket and down face of water-cooling jacket. • Between bottom seal plate upper face and isolation fiber down part face. • Between lower part entrance upper face and shroud down face. • All faces of magma to all structures.
GAP, GAPAUTO	• Radial cond. heat transfer between external face of electrical heated part of rod and internal face of ZrO_2 pellet. • Radial cond. heat transfer between external face of ZrO_2 pellet and internal face of cladding. • Radial cond. heat transfer between external face of cladding and internal face of spacer grids. • Radial cond. heat transfer between external face of B_4C absorber rod and internal face of absorber rod cladding. • Radial cond. heat transfer between external face of shroud and internal face of ZrO_2 isolation fiber. • Radial cond. heat transfer between external face of ZrO_2 isolation fiber and internal face of Ar cooling jacket. • Radial cond. heat transfer between external face of shroud and internal face of Zr flange. • Radial cond. heat transfer between external face of Zr flange and internal face of Ar cooling jacket. • Radial cond. heat transfer between external face of bottom seal plate and internal face of Ar cooling jacket. • Radial cond. heat transfer between external face of lower part entrance and internal face of bottom seal plate.
CONV, CONVAUTO	• External faces of spacer grids, claddings, corner rod, absorber rods, lower part entrance, magma and water channel box. • Internal face of water channel box, zirconium shroud and water-cooling jacket at the top. • Upper face of zirconium flange.

Chemical interaction models are divided into two groups, which consider rod-like geometries and magma. Each activated module and its corresponding structures are given in Table 4-5. The rod-like geometry category accounts for all cylindrical structures. The first selected module for rod-like geometries, ZROX, was used to activate Zircaloy oxidation, and the recommended option for higher temperatures, “BEST-FIT”, was selected (Schanz, Adroguer and Volchek, 2004). In order to describe the oxidation of stainless steel, the FEOX model correlation “MATPRO” was selected. This default correlation was validated using 304L stainless steel (White, 1968). The oxidation of the B_4C material was activated with the BCOX module, and the “BEST-FIT” option

was selected. Based on the experimental database which covers lower temperatures of less than 1000 °C (Litz and Mercuri, 1963), temperatures up to 1300 °C (Sato, Haryu and Endo, 1988) and even higher temperature levels (Steinbrück, 2005) were considered with this chosen option. The module BCSS and corresponding correlation (Nagase, Uetsuka and Otomo, 1997) were activated for eutectic interaction between B_4C and stainless steel materials. Finally, the oxidation of the molten mixed material, referred to as magma, was simulated using the UZOXMAG module.

Table 4-5 Described chemical interaction models in ASTEC model of QUENCH-20 experiment.

Rod-like geometry (rods, shroud, grids)	ZROX	Claddings of heated rods, corner rod, water channel box, zirconium shroud.
	FEOX	External face of absorber rod cladding and spacer grids.
	BCOX	External face of B_4C absorber rods.
	BCSS	Between B_4C absorber rods and stainless-steel absorber rod cladding.
Magma	UZOXMAG	Magma structure to simulate Zr-O-U oxidation.

During the experimental phases, the shapes of the structures could change due to severe thermal and pressure loads. These deformed structures can block existing flow paths or create new pathways depending on how their shapes are altered. To account for these geometrical variations, ASTEC automatically enables the CYCLAUTO model.

The CREE model simulates cladding creep up to the point of failure; hence, it was applied to all heated rods within the test section. The structural integrity of the fuel rod simulator claddings, the fuel channel box, the shroud, and the B_4C absorber cladding was evaluated using the INTE model. The temperature and oxide thickness dependent integrity criteria for these structures were employed on previous experimental databases (Barrachin *et al.*, 2013) (Hofmann *et al.*, 1999). For Zircaloy materials, if the temperature of the structure exceeded 2300 K and the thickness of the ZrO2 layer was less than 300 micrometers, the structural condition changed to "DISLOCAT", indicating the onset of material dislocation. Additionally, if the temperature exceeded 2500 K regardless of oxide thickness, the condition also changed to "DISLOCAT". Regarding the stainless steel cladding of the control rods, the loss-of-integrity point was defined at a liquefaction temperature of 1730 K, with the structural condition changing to "DISLOCAT" above this limit.

By activating these specific chemical and thermal models, the ASTEC code can calculate the timing of structural failure and the rate of hydrogen generation. Accurately capturing these physical phenomena at the bundle scale is a crucial prerequisite for generating a reliable radiological source term at the full plant scale.

4.4 Comparison of ASTEC predictions with experimental data

An axial temperature profile comparison between the ASTEC predictions and the QUENCH-20 experimental data was made at specific phases of the test. In the comparison figures, solid lines represent the ASTEC predictions, while markers correspond to the test thermocouple readings. Consistent color coding was used for the structures, and specific marker selections were made to indicate the corresponding edges of the test bundle.

The initial conditions for the ASTEC model were established using the initial readings from the test thermocouples. In cases where multiple thermocouples were located at the same elevation but at different azimuthal edges of the test bundle, their average reading was used to define the initial state for the code. A comparison between the initial axial temperature profile of the test section structures predicted by ASTEC and the measured data is presented in Figure 4-8. At this initial state, the highest temperature was recorded between the 750 mm and 1000 mm axial positions for Rod 18, which is situated at the outermost section of the bundle. Additionally, thermocouples located at the 0-degree and 270-degree edges, for both the fuel rods and the shroud, recorded the highest temperatures within their respective groups. This early temperature deviation across the bundle is attributed to the specific placement of the control blades between the shroud and cooling jacket on the 0-degree and 270-degree edges. Combined with the non-symmetric structural layout of the test bundle, this geometry induces unequal flow rates and uneven heat removal around the structures from the very beginning.

Starting from the outermost boundary, the predicted axial temperature distribution of the cooling jacket is in very good agreement with the measured data. Moving inwards, the axial shroud temperature profile predicted by ASTEC generally follows the trend of the measured data across the 0, 90, 180, and 270-degree azimuthal positions, showing particularly good agreement at 180 degrees. However, localized deviations are observed and the largest discrepancy occurs at an elevation of 950 mm, where the code underpredicts the temperature by approximately 100 K for the 270-degree position. On the other hand, overpredictions of about 40 K are observed for the shroud temperature at 270 degrees at the 50 mm and 1050 mm elevations. For the fuel channel box (canister), the predicted axial temperature is very close to the limited measured data points available between 250 mm to 500 mm elevations.

Regarding the heated rod groups, the ASTEC predictions show a strong capability to capture the general thermal behavior. The axial temperature distribution predicted for the central rod (Rod 1) is in very good agreement with the experimental data. Similarly, the agreement for the inner rod group (Rods 3, 5, 7, and 9) is very good along the entire bundle elevation, with a minor

exception at 1250 mm, where a slight underprediction for Rod 5 and an overprediction for Rod 9 are observed. For the rods situated closer to the periphery (Rods 10, 11, 16, 18, 20, 22, 23, and 24), the predicted axial temperature distribution is in good agreement with the respective measured data. The most notable exception for this group occurs around the peak temperature region at the 950 mm elevation.

These localized discrepancies, particularly the underpredictions at the 950 mm elevation for structures located at specific azimuthal angles (e.g., Rod 18 and the 270-degree shroud position), highlight the inherent limitations of employing a code that assumes an equally distributed radial heat transfer. Because the QUENCH-20 test bundle has a highly asymmetric arrangement, the resulting non-uniform coolant flow cannot be perfectly captured by the concentric ring discretization approach used in the ASTEC model. Nevertheless, the overall strong agreement across the majority of the elevations confirms the phenomenological validity of the model for capturing the global thermal response.

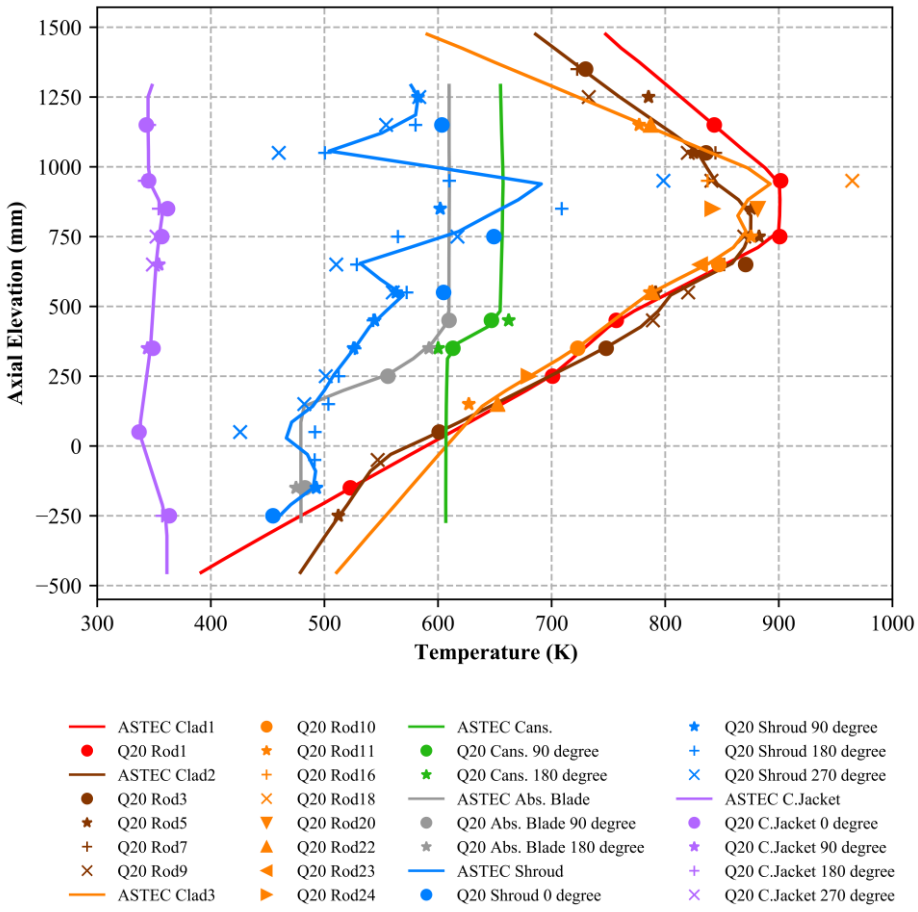


Figure 4-8 Temperature predictions of the ASTEC and QUENCH-20 experiment readings at initial condition (Murat *et al.*, 2020).

The temperature predictions of the ASTEC model and the test readings at the end of the pre-oxidation phase (14,400 seconds), following exposure to a constant steam and argon flow rate at a power level of approximately 7.5 kW, are presented in Figure 4-9. As expected, the temperature predictions for the cooling jacket perfectly followed the thermocouple readings based on the prescribed boundary conditions. However, the thermocouple readings for the shroud were highly dispersed. Between the 750 and 1000 mm axial positions, a temperature difference of approximately 200 K was observed among thermocouples located at the same axial elevation but at different azimuthal angles. While the predicted axial shroud temperature profile generally follows the trend of the data across all azimuthal positions and is in very good agreement at 180 degrees, it struggles to capture this extreme dispersion. The largest deviation is observed at the 950 mm elevation, where the code underpredicts the temperature by approximately 120 K for the 270-degree position. For the fuel channel box (canister) and absorber blades, drawing a definitive conclusion is difficult due to the limited number of thermocouples.

Regarding the heated rod groups, the ASTEC predictions show a strong capability to capture the general thermal behavior, though some radial deviations exist. The predicted axial temperature distribution for the central rod (Rod 1) is in very good agreement with the experimental data. Similarly, the agreement for the inner rod group (Rods 3, 5, 7, and 9) is very good along the entire bundle elevation, with an exception at 1250 mm and above, where an overprediction for the rods was recorded. For the outer rods (Rods 10, 11, 16, 18, 20, 22, 23, and 24), the predicted distribution is also in good agreement with the respective measured data. The most notable exception occurs at the peak temperature elevation of 950 mm, where an underprediction of about 100 K is observed for Rod 18, alongside an overprediction of around 50 K for Rod 16.

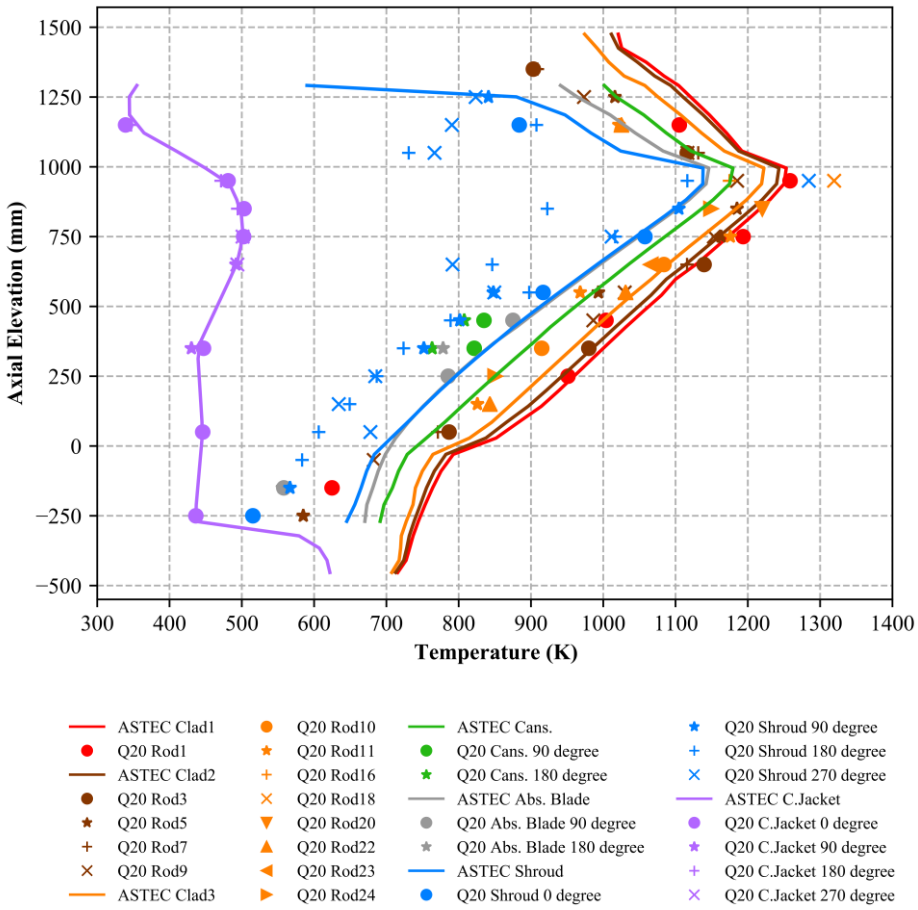


Figure 4-9 Temperature predictions of the ASTEC and QUENCH-20 experiment readings at 14400 seconds (Murat *et al.*, 2020).

From the starting point of the transient phase, the electrical power level was increased while maintaining the steam and argon flow. The power generated by exothermic chemical reactions increased alongside this rising electrical power, leading to a rapid temperature escalation in the structures. At 15,890 seconds, which marks the end of this transient phase, the temperature predictions of the ASTEC model and the experimental readings are presented in Figure 4-10. During the experiment, fuel rod cladding burst and molten material relocation were observed when the cladding temperature reached 1700 K, followed by control blade and shroud failures in the test bundle (Stuckert *et al.*, 2023).

A detailed evaluation of Figure 4-10 shows how the onset of these severe degradation phenomena impacts the agreement between the ASTEC predictions and the measured data. At the outermost boundary, the temperature predictions for the cooling jacket continue to follow the thermocouple readings perfectly based on the prescribed boundary conditions. However, moving

inwards, structural failure can be directly inferred from the highly dispersed temperature readings of the shroud. Between the 500 mm and 1000 mm axial elevations, the thermocouple readings for the shroud are extremely scattered, with some measurements exceeding the ASTEC prediction by several hundred Kelvin, while others remain much lower. For the fuel channel box (canister), the limited measured data points at the 500 mm elevation indicate a slight underprediction by the code.

Regarding the heated rod groups, the ASTEC predictions capture the global temperature escalation but struggle with localized deviations caused by the degrading geometry. At the lowest elevations (below 350 mm), the predicted axial temperatures for all rod groups remain in very good agreement with the experimental data. However, for the second rod group at an axial elevation of approximately 500 mm, the thermocouple readings show a massive difference of around 500 K compared to the ASTEC predictions. Moving to the peak temperature region (around 850 mm to 1050 mm), ASTEC predicts maximum temperatures of approximately 2000 K to 2100 K. While this predicted peak magnitude aligns well with the highest individual thermocouple readings for the rods, the experimental data shows a massive radial spread across different azimuthal angles which the code cannot capture. Finally, at the upper unheated elevations (around 1250 mm and above), ASTEC generally overpredicts the rod temperatures by approximately 200 K to 300 K.

Because many of the thermocouple readings were already well above 1700 K at the end of the transient phase, it can be concluded that material movement, melting, and severe flow path blockages were present in the test bundle at that instant. Deformations within the test bundle and a localized lack of injected cooling gases in certain blocked sub-channels likely caused the extreme 500 K discrepancy observed at the 500 mm elevation. Furthermore, as the geometry loses its original intact shape, the non-uniform coolant flow and asymmetric radiative heat transfer become even more pronounced. These massive localized discrepancies fully expose the limitations of the one-dimensional code structure of ASTEC, which evaluates thermal conditions at a single, homogenized axial level and cannot resolve the highly asymmetric, localized flow blockages and structural failures occurring within the degrading bundle.

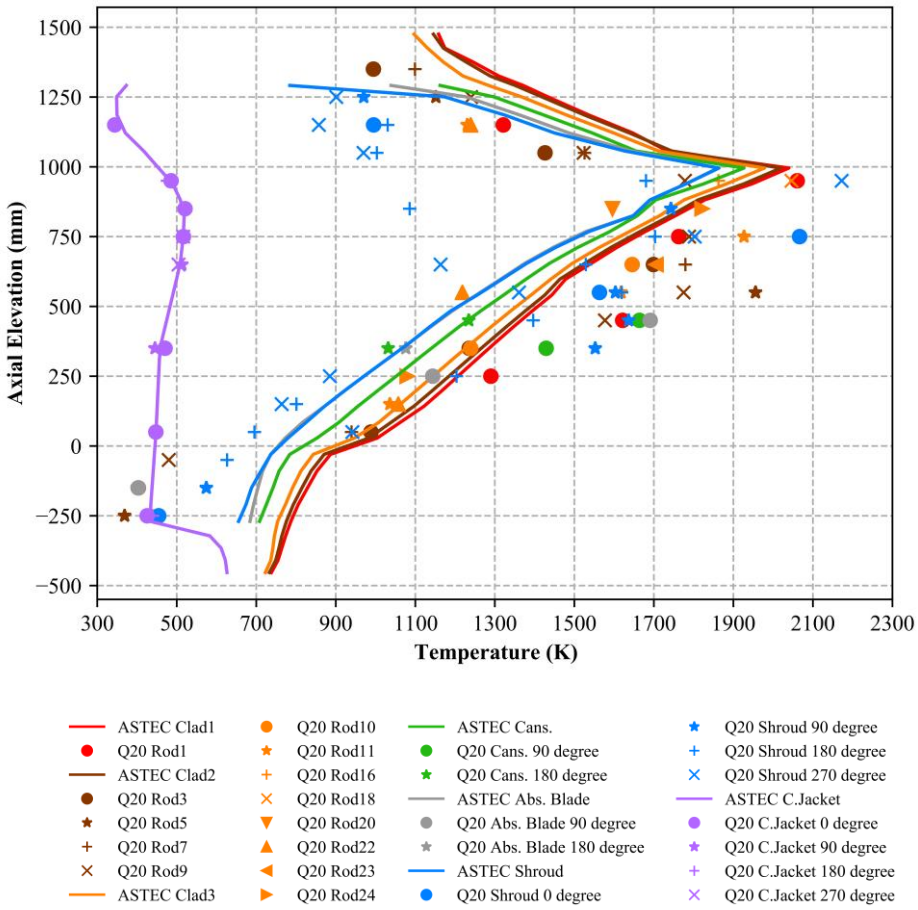


Figure 4-10 Temperature predictions of the ASTEC and QUENCH-20 experiment readings at 15890 seconds (Murat *et al.*, 2020).

At the beginning of the quench phase, the steam injection was cut, and liquid quench water was introduced into the system from the bottom of the test bundle. The temperature predictions of the ASTEC model and the test measurements exactly 20 seconds later, at 15,910 seconds, are given in Figure 4-11. Observations during the experiment indicated that immediately following this quench water injection, a strong exothermic reaction occurred, and the relocation of molten cladding along with spacer grids was recorded (Stuckert *et al.*, 2023).

A detailed evaluation of Figure 4-11 reveals stark contrasts between the one-dimensional model predictions and the highly chaotic, degraded physical reality of the bundle during this phase. At the outermost boundary, the cooling jacket temperatures remain steady and in perfect agreement with the prescribed boundary conditions. However, the shroud temperatures show extreme dispersion that ASTEC fails to capture. While the code predicts a relatively smooth shroud temperature profile peaking around 1900 K, the experimental data is strongly scattered.

Some shroud thermocouples measure temperatures above 2200 K due to localized exothermic spikes, while others at the same elevation show significant cooling.

Regarding the heated rod groups, the discrepancies are distinctly divided between the flooded lower elevations and the reacting upper elevations. Just 20 seconds after the water injection started, the actual water level in the test bundle had already reached an axial elevation of 750 mm. Temperature readings from the thermocouples attached to the rod groups up to this 750 mm elevation decreased to approximately 400 K, indicating that these sections had successfully quenched and cooled down. In sharp contrast, the ASTEC model massively overpredicts the rod temperatures in this lower region, predicting values between 800 K and 1400 K. The cooling effects of the water injection and the corresponding temperature decrease in the model were only just beginning to appear at the very bottom of the bundle.

Conversely, in the peak temperature region above the water front (850 mm to 1050 mm), the experimental data reveals severe temperature escalations, with individual rod thermocouples spiking well above 2200 K. The ASTEC temperature predictions did not show a temperature escalation as severe as the one observed in the experiment during these first 20 seconds, underpredicting these highly localized exothermic peaks.

These massive deviations can be interpreted as direct evidence of severe degradation in the flow paths and structural deformation within the test bundle. Because the ASTEC model did not predict such severe structural degradation and flow blockages prior to quenching, it could not capture the rapid, localized water rise or the intense cooling effects at the 0 degree and 270 degree edges. Furthermore, the loss of structural integrity likely resulted in the stripping of protective oxide layers upon quenching, exposing the inner metallic sections to the steam environment and causing a secondary oxidation. As structures lose their integrity, oxidation levels rise further and these degradation processes proceed by continually triggering one another, creating highly localized thermal extremes that inherently bypass the predictive capabilities of a homogenized 1D severe accident code.

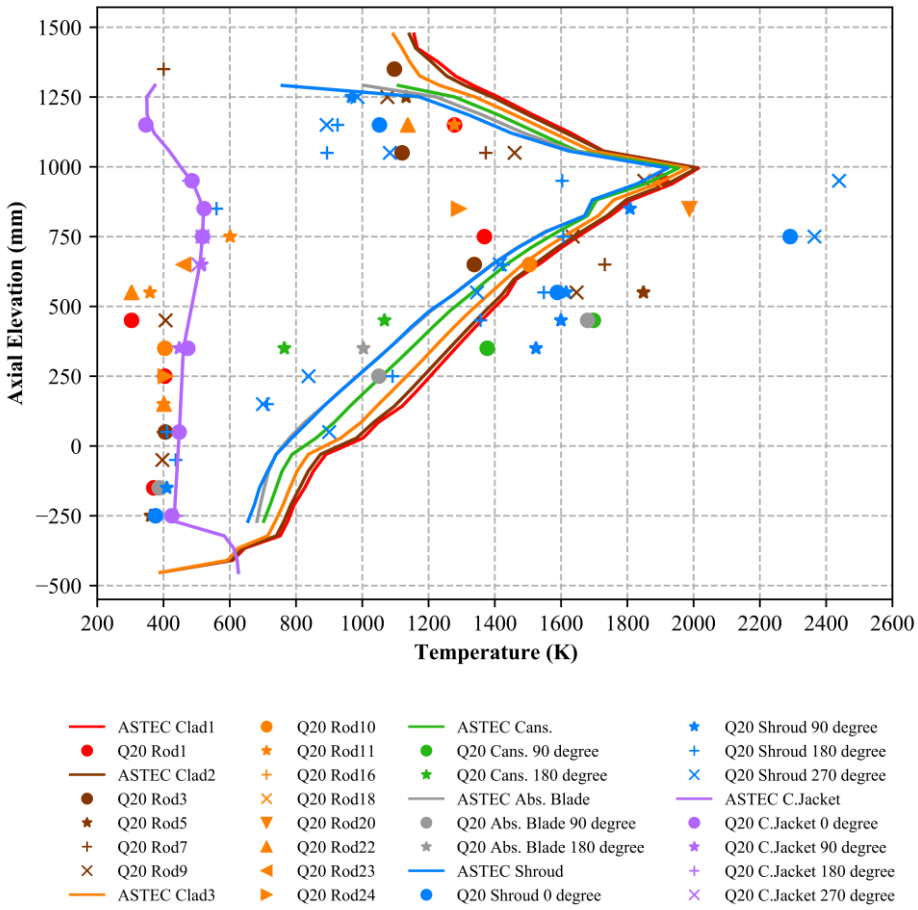


Figure 4-11 Temperature predictions of the ASTEC and QUENCH-20 experiment readings at 15910 seconds (Murat *et al.*, 2020).

The temperature predictions of the ASTEC model and the test readings at 15,990 seconds which is 100 seconds after the quench water injection began at the bottom of the bundle, are presented in Figure 4-12. By this time, the cooling effect of the injected water had become clearly visible across the lower elevations of both the experimental data and the simulation.

The Figure 4-12 illustrates how the model attempts to capture the progression of the quench front. At the outermost boundary, the cooling jacket temperatures remain in excellent agreement with the boundary conditions. Moving to the lower elevations of the heated bundle (from 0 mm to approximately 500 mm), the ASTEC model has now successfully caught up with the experimental quenching process. Both the predicted rod temperatures and the corresponding thermocouple readings in this lower region have dropped to approximately 400 K to 500 K, indicating a fully quenched and cooled state.

However, in the middle and upper elevations (above 500 mm), the physical reality of the highly degraded bundle diverges significantly from the 1D model predictions. The shroud temperatures exhibit massive dispersion; while ASTEC predicts a relatively smooth thermal gradient rising to approximately 1900 K at the 1000 mm elevation, the experimental shroud thermocouples are violently scattered, with readings ranging from 500 K up to localized hot spots exceeding 1600 K. For the heated rod groups in the peak temperature region (around 900 mm to 1000 mm), the ASTEC model predicts a steep temperature gradient peaking near 1900 K to 2000 K. While these maximum predicted temperatures appear similar to several of the individual test readings at the 1000 mm axial location, the experimental data shows extreme radial scatter, with some rods remaining much hotter and others cooling much faster. Finally, at the upper unheated elevations (1200 mm to 1500 mm), ASTEC generally overpredicts the temperatures of the rods and the shroud.

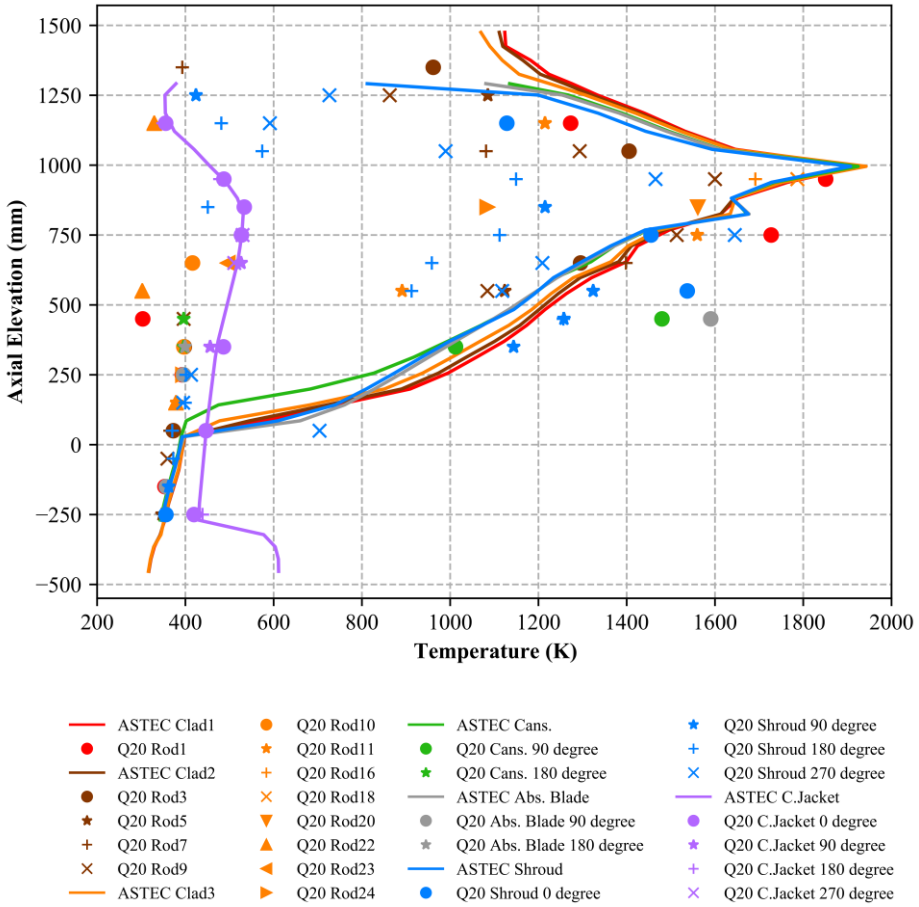


Figure 4-12 Temperature predictions of the ASTEC and QUENCH-20 experiment readings at 15990 seconds (Murat *et al.*, 2020).

The total produced hydrogen caused by the oxidation during the test transient is given in Figure 4-13. At the end of the QUENCH-20 test, 57.4 g of hydrogen was produced, with 10 g of this total originating from boron carbide oxidation. The ASTEC predictions for the total hydrogen generation and the boron carbide related amount were 53.4 g and 9.48 g, respectively. As can be seen in the figure, a very similar trend in hydrogen production, which rose steadily until the quench phase and spiked after the liquid water injection, was observed in both the simulation and the experiment. Additionally, the total production amount and the boron carbide percentage were highly comparable with the test readings. It is expected to see a slightly smaller total hydrogen production in the prediction compared to the experimental readings, because the formation of micro-cracks and the corresponding increase in surface area during the real physical transient are not accounted for in the ASTEC model.

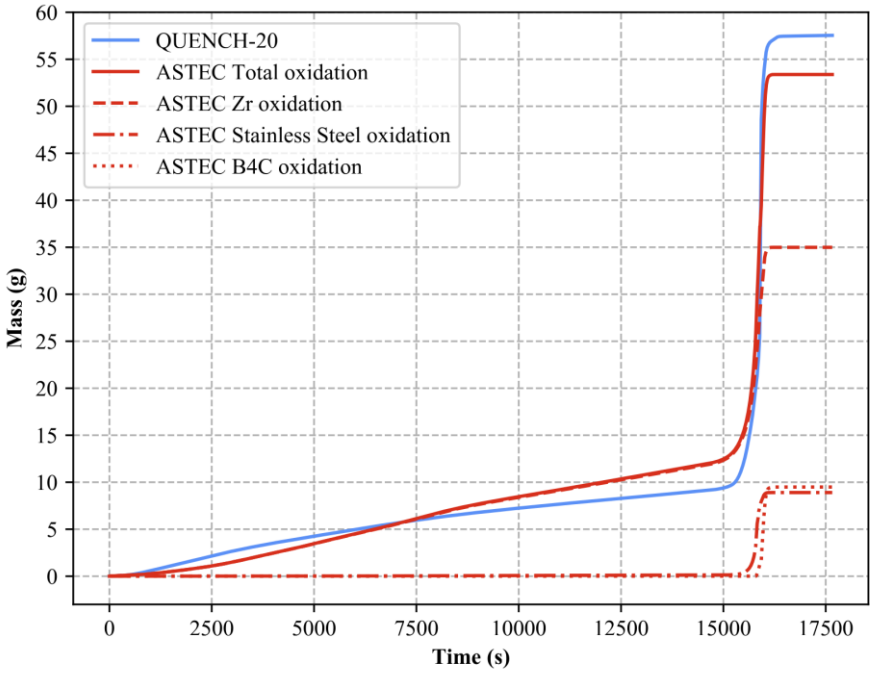


Figure 4-13 Comparison of the cumulative hydrogen generation due to oxidation of materials (Zircaloy, Stainless-Steel, Boron Carbide) in the bundle predicted with ASTEC and measured in QUENCH-20 (Murat *et al.*, 2020).

4.5 Conclusion

The primary parameter of interest observed during the experiment was the hydrogen production of the fuel rod simulators and of the BWR specific fuel channel box and absorber blade during the bundle oxidation and quench phase. The ASTEC model, developed based on the specific design characteristics of the test section, successfully reproduced this metric. Tracking this hydrogen production is a critical milestone for the validation process, as it is a significant driving factor for excess heat production during the in-vessel accident progression due to highly exothermic oxidation reactions. The oxidation kinetics of both the zircaloy structures and the B_4C material in the control blades were tracked by the code with acceptable accuracy, demonstrating ASTEC's capability to capture the contribution of control materials to total hydrogen generation.

However, the heterogeneity of the solid structure placement in the test bundle created non-symmetrical heat loading, localized failures, and clogging in the fluid flow area during the experimental transient representing a major challenge for integral codes such as ASTEC developed for the simulation of reactor cores. The ASTEC intrinsically assumes the homogenous placement of structures and an equally distributed fluid flow regime, struggled to capture these highly localized, asymmetric thermal variations and structural failures. Consequently, the model artificially preserved strong cooling capabilities around the structures. While there is room for enhancement in modeling such specific geometries, it must be noted that full plant-scale applications follow a much more homogenous core layout within the pressure vessel; extreme structural heterogeneity is primarily an artifact of partly cut-off experimental test sections.

While relying on a single integral experiment carries inherent geometric scaling limitations, the validation strategy applied in this thesis focuses on phenomenological validity. The QUENCH-20 experiment is currently the only available integral test that combines a prototypic BWR geometry with boron carbide control blade degradation. By proving that ASTEC accurately calculates the fundamental source terms of heat and hydrogen at the bundle level, the underlying physics of the early-phase degradation are successfully validated.

Demonstrating the reliability of these BWR degradation models at the experimental scale provides the scientific justification necessary for their extrapolation to the full-scale plant model. While future work should expand the validation matrix to include late-phase lower head phenomena since the major uncertainties in BWR accident progression is the behavior of the melt in the lower plenum, which contains a dense forest of control rod guide tubes. Historical experiments, such as the XR-1-1 and XR-2-1 tests (Gauntt and Humphries, 1997) (Hodge and Ott, 1997), demonstrated that molten metals from BWR control blades drain quickly and can

attack vessel penetrations before the oxide fuel even melts. Furthermore, programs like FOREVER (Sehgal *et al.*, 2003) and OLHF (NEA, 2003) emphasize the complexity of vessel wall creep failure. Expanding the validation matrix to include these late-phase lower head phenomena is a necessary future step to ensure the robust application of ASTEC to complete BWR severe accident transients.

5 Application of the computational route to predict the radiological consequences of severe accidents in BWRs

5.1 Realistic prediction of the nuclide inventory of the different core loading of the Peach Bottom Unit-2 BWR

The first step of any comprehensive severe accident analysis is the accurate determination of the reactor initial nuclide inventory at the moment of accident occurs. This inventory describes both the decay heat that drives the thermal hydraulic accident progression and the total mass of the radioisotopes available for a potential release from the degraded core which transport into the containment and the environmental release. Consequently, this section establishes the methodology for quantifying these critical source terms. First, the influence of the reactor operational history and fuel design evolution on the radiological impact is examined. Then detailed computational predictions using ORIGEN and CASMO codes are presented to quantify the exact End of Cycle (discharge level burnup) fission product inventory for both historical and modern core loading configurations.

5.1.1 Relevance of core loading and irradiation history for radiological impact

The radiological impact of a severe accident is fundamentally dictated by the initial fission product inventory in the reactor core when the accident begins. This inventory is highly sensitive to the core loading design and the specific irradiation history of the fuel. Over the operational lifespan of a nuclear power plant, fuel assembly designs evolve and thermal power levels are often upgraded, leading to significantly higher discharge burnups.

This evolution is clearly visible in the history of the Peach Bottom Unit-2 NPP. The plant received its operational license in 1973, a period when the BWR reactor fleet predominantly utilized the 7x7 fuel assembly design. Following its first authorized power level of 3923 MWth with these 7x7 assemblies, the Peach Bottom Unit-2 power level was upgraded three times: in 1994, 2014, and 2017 to 3458 MWth, 3951 MWth, and finally 4016 MWth, respectively (Exelon Generation Company, 2018). During these power upgrades, the design of the fuel assemblies was also modernized. Based on the discharged BWR fuel assembly databank (Hu *et al.*, 2016) following the latest power upgrade, the GE14 10x10 type fuel assembly is currently in operation. Additionally, recent studies (Bixler *et al.*, 2013) have taken into account the GE14 10x10 fuel assembly design for the current core loading of Peach Bottom Unit-2.

Because modern 10x10 assemblies operate at higher specific powers and achieve much higher burnups than historical 7x7 assemblies, relying on outdated core loading data would result in a severe underestimation of the radiological source term. Therefore, accurately predicting the nuclide inventory requires a precise evaluation of the modern irradiation history.

5.1.2 Nuclide inventory predictions at End of Cycle

In order to establish a baseline and compare the evolution of the fission product inventory, calculations were first performed for the historical 7x7 core using the ORIGEN code. A reference study on the Peach Bottom Plant (Carbajo, 1993) and related publication (Carbajo, 1994) only provide a general statement regarding the fission product inventory calculation. That analysis was performed for a case of long-term operation to achieve a high level of burnup. Since the exact exposure duration and burnup level in that reference were not clear, a new burnup analysis was conducted using SCALE V6.2b ORIGEN (Wieselquist, Lefebvre and Jessee, 2020).

Based on the previously referenced study, which described 168.48 tons of fuel material, it was concluded that the modeled fuel assembly likely had a 7x7 layout. The U.S. BWR fuel assembly databank (Hu *et al.*, 2016) displays the operating periods of various fuel assembly designs and the evolution of the achieved discharge burnup and this databank information is given in Figure 5-1.

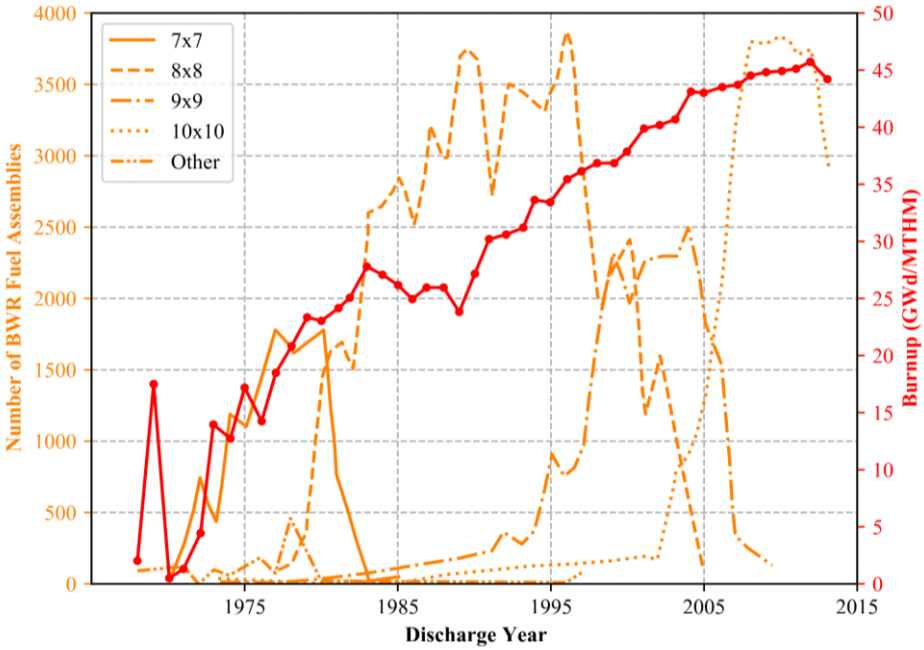


Figure 5-1 BWR fuel assembly type usage and burnup evolution from 1968 to 2013 in the United States (Hu *et al.*, 2016).

For the ORIGEN calculation, a single 7x7 fuel assembly model containing 0.1902 tons of uranium was employed. The average specific power of the fuel assemblies in the databank was recorded as 24 MW/MTU; the corresponding power level was adjusted for the fuel assembly model, and two years of operation were foreseen. Based on this model and the operational specifications, a discharge burnup level of 17.5 GWd/t was obtained. A comparison between this achieved discharge burnup and the burnup progression over the years for BWR fuel assemblies (Figure 5-1) shows that the burnup level was indeed around 15 GWd/t during the operational periods in the mid-1970s. The fission product inventory from the reference study and the one calculated using the ORIGEN code are compared in Table 5-1. The MELCOR code categorizes certain classes of fission products, and only the underlined elements in the table were taken into account in the reference study for the mass comparison.

Table 5-1 Fission product element masses in reference study and calculated with Scale ORIGEN code.

Class names in MELCOR	Member of elements	Reference Study (kg) (Carbajo, 1993)	Scale ORIGEN V6.2b (kg) (Murat *et al.*, 2023)
Noble gasses	Xe, Kr, Rn, He, Ne, Ar, H, N	463.7	446.7
Alkali metal	Cs, Rb, Li, Na, K, Fr, Cu	246.3	256.9
Alkaline metal	Ba, Sr, Be, Mg, Ca, Ra, Es, Fm	207.52	187.19
Halogens	I, Br, F, Cl, At	20.93	17.44
Chalcogens	Te, Se, S, O, Po	40.78	40.99
Platinoids	Ru, Pd, Rh, Ni, Re, Os, Ir, Pt, Au	306.99	296.6
Transition metals	Mo, Tc, Nb, Fe, Cr, Mn, B, Co, Ta, W	350.69	324.98
Tetravalents	Ce, Zr, Th, Np, Ti, Hf, Pa, Pu, C	593.65	554.22
Trivalents	La, Pm, Sm, Y, Pr, Nd, Al, Sc, Ac, Eu, Gd, Tb, Dy, Ho, Er, Tm, Yb, Lu, Am, Cm, Bk, Cf	571.03	528.0
More volatile main group metal	Cd, Hg, Pb, Zn, As, Sb, Tl, Bi	1.41	1.284
Less volatile main group metals	Sn, Ag, In, Ga, Ge	8.59	8.917

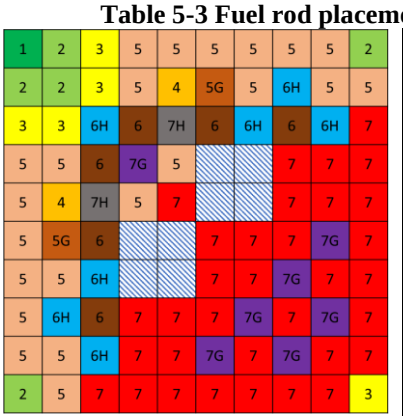
In order to predict the nuclide inventory for the modern core, the CASMO5 neutron transport code was employed to perform a detailed burnup analysis of the GE14 10x10 fuel assembly (Hykes, Ferrer and Rhodes, 2022). The dimensions of the fuel assembly, the fuel rod placement, enrichment contents, void fraction profiles, operational periods, and specific power are all

required to perform this analysis accurately. The dimensions of the fuel assembly and the fuel rods are given in Table 5-2 while the placement of the fuel rods and their respective enrichments are detailed in Table 5-3. Two large spaces in the center of the rod placement layout correspond to the water rods in the GE14 10x10 assembly, each covering an area equivalent to four fuel rods.

Table 5-2 Dimensions of the GE14 10x10 fuel assembly (Rochman *et al.*, 2022), *(Radaideh, Price and Kozlowski, 2018).

Parameter	Value (cm)
Fuel radius	0.438
Cladding inside radius	0.447
Cladding outside radius	0.513
Fuel rod pitch	1.295
Active fuel length	368.0
Part length rod length	220.8
*Water rod inside diameter	2.321
*Water rod outside diameter	2.521
*Fuel channel box inside length	13.406
*Fuel channel box outside length	13.914

Table 5-3 Fuel rod placement, enrichment and Gd content of GE14 10x10 Assembly.



Fuel Type	U-235 w/o	Gd w/o
1	1.6	0.0
2	2.8	0.0
3	3.2	0.0
4	3.6	0.0
5	3.95	0.0
6	4.4	0.0
7	4.9	0.0
5G	3.95	8.0
6H	4.4	6.0
7G	4.9	8.0
7H	4.9	6.0

The operational period data was derived from an experimental study program (Rochman *et al.*, 2022) that investigated a GE14 10x10 fuel assembly utilized in the core of the Forsmark 3 NPP in Sweden between July 2000 and May 2005. During this period, the average fuel and moderator temperatures were recorded as 792 K and 560 K, respectively. After five operational cycles, the rod average burnup and rod peak burnup were recorded as 41 MWd/kgU and 56 MWd/kgU. Furthermore, one fuel rod was extracted from the assembly, and samples from eight different axial locations were taken for detailed analysis (Gauld and Mertyurek, 2018).

The fuel assembly was used for a total of 1792 days in the core, with the five operational cycles lasting 354, 270, 320, 487, and 293 days, respectively. Refueling periods were considered between the cycles; the remaining days were equally distributed, and each refueling section was taken as 17 days. The average moderator density at the 1.91 m axial position from the bottom of

the fuel assembly was measured as 0.317 g/cm³, 0.374 g/cm³, 0.324 g/cm³, 0.540 g/cm³, and 0.584 g/cm³ for each respective cycle (Martinez *et al.*, 2015).

In order to estimate the void fraction profile, these recorded moderator densities were utilized. The expected void fraction profiles in a core loaded with GE14 10x10 fuel assemblies are shown at the top left of Figure 5-2. Depending on the assembly's position in the core, the fuel void fraction profile falls somewhere between the distributions represented by the red and blue lines. Fuel assemblies close to the center of the core exhibit distributions closer to the red line, while positions further from the center approach the blue line. At each of the 25 axial positions from bottom to top, the gap between the maximum (red) and minimum (blue) void fraction distributions was divided by the total number of fuel assemblies in the core. In this way, one representative void fraction profile was constructed for each assembly. Because the only known variable was the moderator density at the 1.91 m axial position for each cycle, the corresponding 13th axial node was used as the reference point. By using the operational pressure of 7 MPa and the density at this position, the exact void fraction was determined from among the 764 constructed profiles. The corresponding profiles for each cycle are given in Figure 5-2.

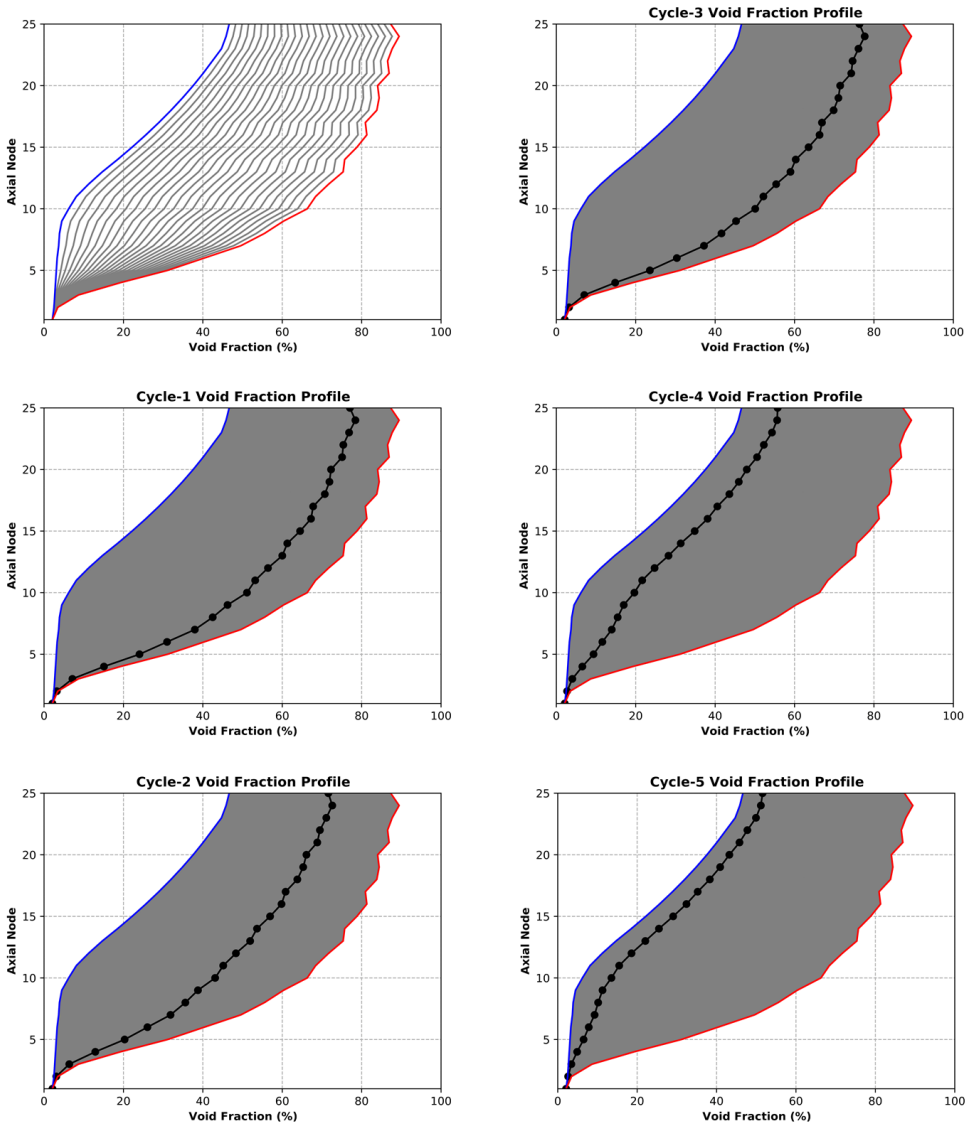


Figure 5-2 Void fraction profile sampling and selected cycle void fraction profiles (Murat *et al.*, 2024).

The average specific power of discharged BWR fuel assemblies in the U.S. is 24 MW/MTU. However, this average includes both new GE14 10x10 designs and older 7x7 and 8x8 designs. A separate criticality study dealing specifically with GE14 10x10 BWR fuel assemblies utilized an average specific power of 25 MW/MTU for this specific design (Radaideh, Price and Kozlowski, 2018). Because the current core consists entirely of GE14 10x10 assemblies, an average specific power of 25 MW/MTU was adopted for this analysis.

The shape of the burnup profile, obtained from the assembly extracted from the Forsmark NPP, is presented in Figure 5-3. The neutron flux and its axial shape during operation dictate the burnup levels at various axial positions along the rods. Based on this relationship, it was assumed

that the specific power follows the exact same shape as the burnup profile shown in the figure. This shape was then scaled by a factor to yield the target average value of 25 MW/MTU.

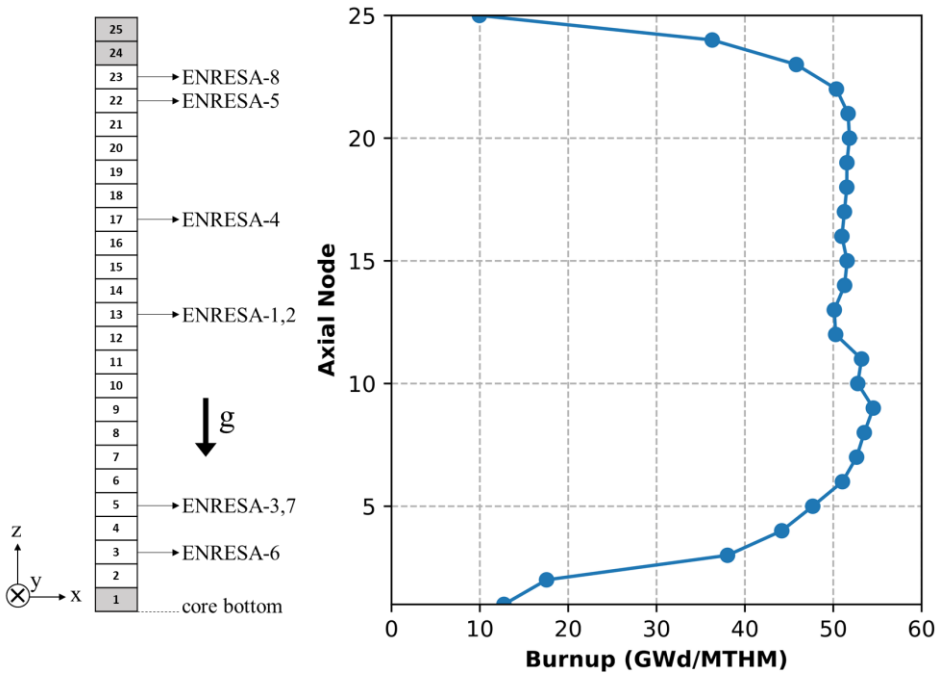


Figure 5-3 Axial burnup profile of the rod from GE14 10x10 Assembly (Marshall *et al.*, 2016).

Utilizing the provided dimensions, materials, enrichments, layout, void fractions, power distribution, and operational durations, a CASMO5 analysis was conducted for each of the 25 axial nodes of the fuel rod. A final discharge burnup of 46.47 MWd/t was obtained for the assembly. For the purposes of this source term evaluation, it was assumed that all 764 assemblies in the core were at this same burnup level, and the total End of Cycle fission product inventory for the entire core was determined based on this conservative assumption.

5.2 Development of an integral Peach Bottom Unit-2 BWR model for severe accident analysis with ASTEC

The foundation of any reliable severe accident analysis is a robust and highly detailed integral plant model. It is important to emphasize that the ASTEC model for the Peach Bottom Unit-2 reactor presented in this study was developed entirely from scratch, rather than being adapted from pre-existing legacy input decks. This ground-up development ensured that every geometric fluid volume, flow path, and structural mass was explicitly investigated and verified to accurately capture the specific physics of both the historical and modernized states of the reactor.

This section details the comprehensive development of this integral plant model. It begins with a description of the plant nodalization and geometric discretization, covering the reactor core, the pressure vessel, the explicit recirculation and jet pump systems, and the primary containment structures. Following the establishment of the physical volumes, the specific ASTEC physical models selected to model heat transfer, chemical interactions, and structural failures are outlined. Finally, in order to ensure the computational stability and physical accuracy of the developed computational route, this section concludes with a steady-state verification, demonstrating that the model successfully replicates nominal plant conditions prior to the initiation of any accident transient. After that, full-scale severe accident transient analyses were subsequently performed. These transient simulations are essential for quantifying the time-dependent release of fission products, ultimately generating the radiological source term required as the input for the subsequent atmospheric dispersion analysis.

5.2.1 **Integral ASTEC Peach Bottom Unit-2 BWR model for steady conditions**

The foundation of any reliable severe accident analysis is a robust and highly detailed integral plant model. It is vital to emphasize that the ASTEC model for the Peach Bottom Unit-2 reactor presented in this study was developed entirely from scratch, rather than being adapted from pre-existing legacy input decks. This ground-up development ensured that every geometric fluid volume, flow path, and structural mass was explicitly tailored and rigorously verified to accurately capture the specific physics of both the historical and modernized states of the reactor.

The following subsections detail this comprehensive nodalization process. First, the core geometries are defined for both the historical 7x7 and modernized 10x10 fuel assembly configurations. The structural domains then expand, detailing the reactor pressure vessel alongside the explicitly modeled recirculation systems and jet pumps. Subsequently, the primary containment structures and failure criteria are described to establish the ex-vessel boundaries. Following the geometric discretization, the specific ASTEC physical models selected to govern the thermal, chemical, and mechanical degradation phenomena are outlined. Finally, this section concludes with a steady-state verification, proving that the newly developed model successfully and stably replicated nominal plant conditions before the initiation of any severe accident transient.

5.2.2 **Core model configurations**

In order to accurately simulate the historical and modern operating states of the Peach Bottom Unit-2 reactor, two distinct core model configurations were developed.

As a first step, represent the initial operational phase of the reactor, a baseline core nodalization was constructed based on the historical 7x7 fuel assembly configuration**.** Within this model, the active core domain was radially divided into four bypass channels designated as “bypass1”, “bypass2”, “bypass3”, and “bypass4”. A newly developed BWR fuel channel box structure was placed in each channel with its respective weighting factor. Each fuel channel box encloses the space around the fuel rods, defining the internal sub-channel domains. From the innermost to the radially outermost region, these sub-channels are named “Core1”, “Core2”, “Core3”, and “Core4”. To accurately reflect the historical 7x7 fuel assembly design, a weighting factor of 49 was applied to the representative cylindrical structure within each fuel channel box.

The control rod structures, which are located in the bypass channels, were adjusted to correspond with the number of fuel channel boxes, allocating one cylindrical control structure for every four assemblies. Their assigned weighting factors, moving radially from channel bypass1 to bypass4, were 1, 15, 60, and 115, respectively. The active core region is enclosed by the shroud structure just outside the bypass4 channel. Between the shroud and the solid jet pump structures, an intermediate channel named “jet” was defined. Finally, the outermost vessel structure encapsulates all internal pressure vessel components, defining the downcomer channel. An insulator structure was also defined around the exterior of the vessel solely to establish the thermal boundary conditions.

Axially, the core region was divided into 14 sections. The fuel channel boxes span from the first axial mesh up to the top of the core. The active core components, including the UO_2 fuel and the B_4C control material along with their respective zircaloy claddings, were placed at their corresponding axial elevations. The complete radial channel division, axial meshing, placement of solid structures, and material assignments are illustrated in Figure 5-4.

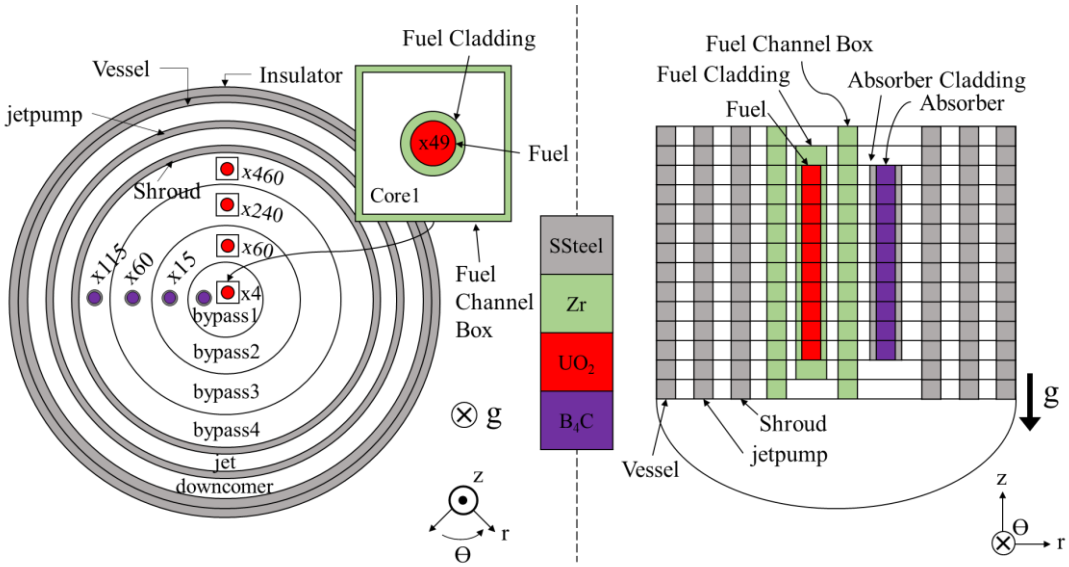


Figure 5-4 Core radial mesh (on the left) and core axial mesh (on the right) of Peach Bottom Unit-2 ASTEC Model (Murat *et al.*, 2023).

The lower plenum, located below the active core section, represents a complex geometry (Figure 5-5). Due to nodalization constraints, the fluid volume of the lower plenum was represented by a single fluid mesh; therefore, no internal axial meshing was constructed within the fluid domain itself. However, the structural wall of the lower plenum was meshed, being divided into three radial sections and 26 axial pieces from the top (0.0 m) to the bottom (-6.376 m). While the physical lower plenum contains 191 internal support columns which corresponds one for every four assemblies, representing a large fraction of solid structural mass, their precise dimensions and mass profiles are unknown. Consequently, these support structures could not be explicitly considered in the ASTEC model.

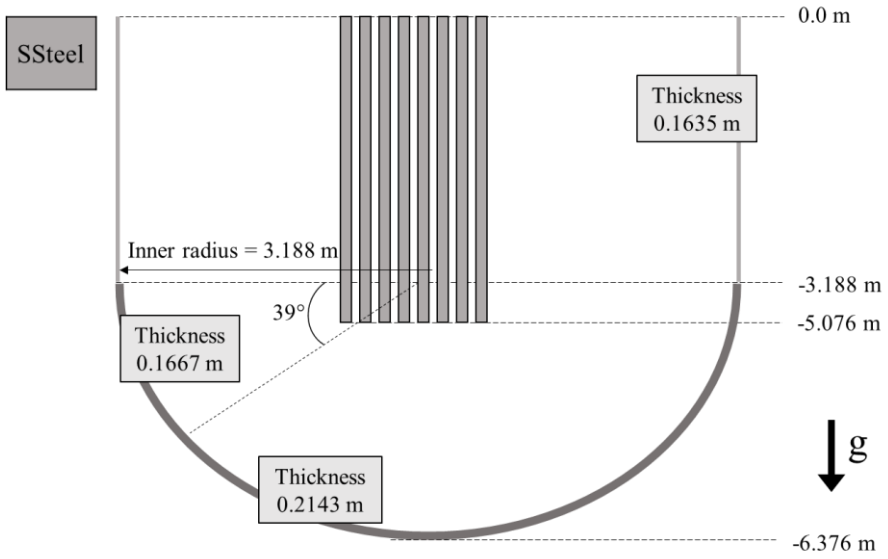


Figure 5-5 Lower plenum representation of Peach Bottom Unit-2 ASTEC Model (Murat *et al.*, 2023).

In order to evaluate the impact of structural modernizations on severe accident progression, a secondary core configuration was developed to represent the upgraded GE14 10x10 fuel assemblies. Over the operational lifetime of the power plant, fuel assembly designs were upgraded to increase achievable burnup levels (up to 45–50 MWd/kg) and improve overall economic efficiency. This modernized configuration accounts for altered fuel rod layouts, significantly different fission product inventories due to higher burnup, and the inclusion of central water rods for enhanced neutronic moderation. The transition to the 10x10 design inherently increases the total zircaloy structural mass and necessitates the addition of a new sub-channel zone within the fuel channel boxes to represent the water rods.

Furthermore, to represent the reactor recirculation lines in a more realistic manner, the radial nodalization of the ASTEC model was structurally improved. As part of these major updates, the previously defined “jet” channel was removed, allowing for a proper, unified representation of the downcomer channel between the shroud and the vessel wall. These structural changes to the fuel channel boxes and the updated radial downcomer representation are presented in Figure 5-6.

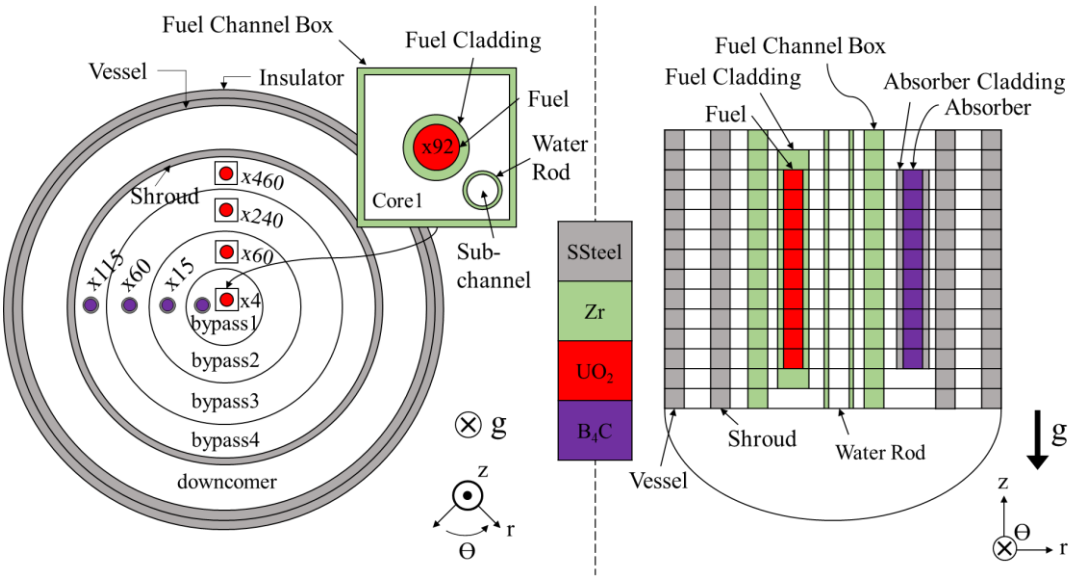


Figure 5-6 Core radial mesh (on the left) and core axial mesh (on the right) of Peach Bottom Unit-2 ASTEC Model with modern fuels and recirculation line update.

5.2.3 Reactor pressure vessel and recirculation system models

Within the ASTEC framework, the recirculation system and coolant flow paths are constructed as interconnected volume structures evaluated by the CESAR thermal-hydraulics module. Because the recirculation loops and jet pumps of a Boiling Water Reactor are physically integrated with the downcomer annulus, the reactor pressure vessel and the recirculation coolant system are described together in this subsection to provide a comprehensive, overall picture of the primary plant model.

In order to establish the baseline thermal-hydraulic volumes, the historical configuration utilized a simplified representation of the RPV and its circulation loop. After the coolant was extracted from the active core region, a designated “Separator (SEP)” volume simulated the BWR steam separator, directing the liquid flow to the upper downcomer volume. In this volume, the liquid water mixed with the incoming feedwater and was directed downward into the downcomer channel. The separated steam flowed upwards into the dryer and upper head sections, and was subsequently extracted from the steam line volumes via specified pressure boundary conditions. The remaining downstream volumes, representing the turbines and feedwater connections, were included solely to facilitate the tracking of the fission product release transient using the SOPHAEROS module of ASTEC. In this model, the entire core liquid flow was recirculated through the “JET_L” recirculation line volumes, with the total flow directed into the previously

defined, artificial “jet” channel. Subsequently, the total fluid inventory entered the lower plenum, enclosing the circulation cycle. Structure of the volumes and connections are given in Figure 5-7.

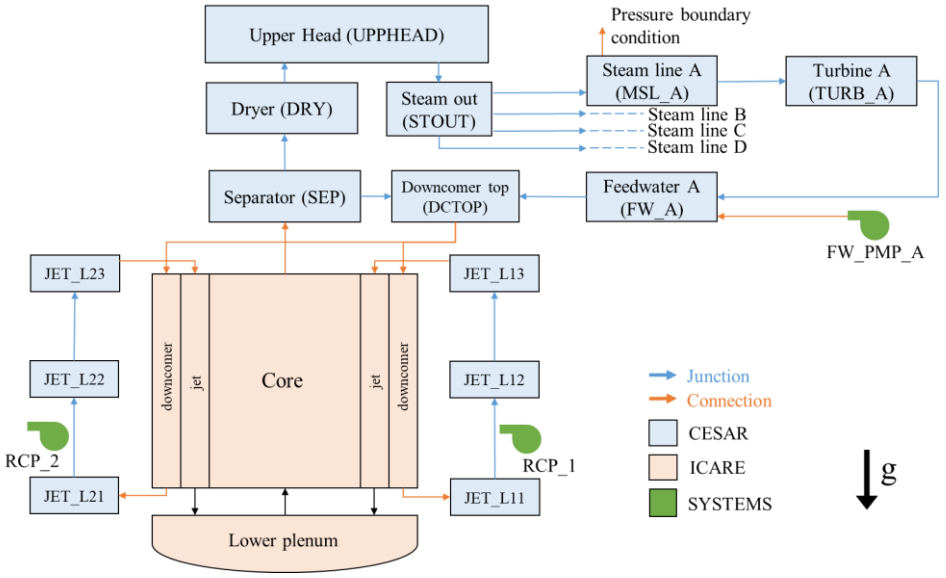


Figure 5-7 Reactor Pressure Vessel and water cycle volumes of Peach Bottom Unit-2 ASTEC Model (Murat *et al.*, 2023).

In order to improve the fidelity of the simulation and better estimate the accident progression, the modernized model introduced an explicit, structurally realistic representation of the recirculation line and jet pumps. While the upper RPV representative volumes remained consistent with the baseline model, the lower vessel and recirculation loop received significant modifications. The volumes and pipe structures of this modernized recirculation line and its connections are illustrated in Figure 5-8.

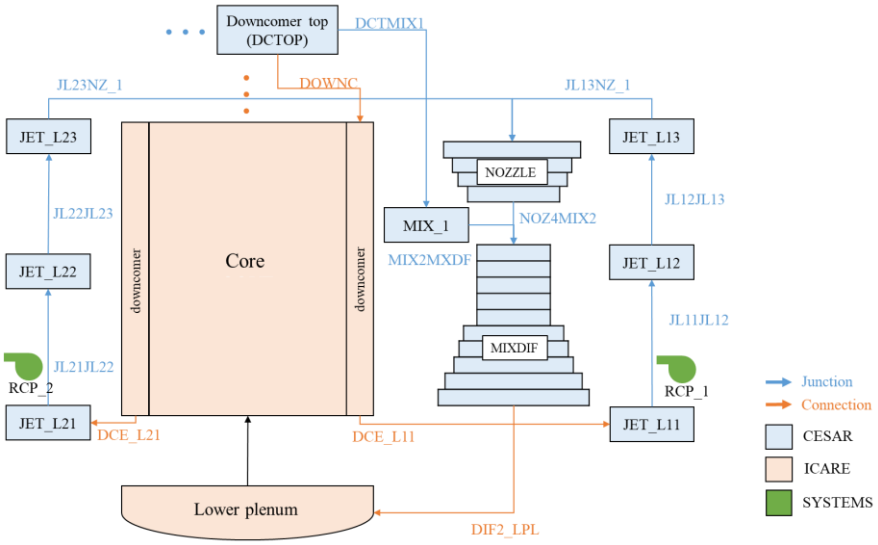


Figure 5-8 Recirculation line CESAR volumes and their connections to the core domain.

In the updated nodalization, after the liquid water was extracted from the separator into the upper downcomer, a portion of the flow was directed to the main downcomer channel, while the remainder was transferred to the new defined “MIX_1” volume and “MIXDIF” pipe structure. From the bottom of the downcomer channel, the jet pump volumes (JET_L) and the explicit recirculation pump structure increased the pressure of the recirculated flow. This pressurized fluid was injected into the “NOZZLE” pipe structure, where it mixed with the incoming liquid flow from the upper downcomer within the MIXDIF pipe. The combined total core flow was then transferred to the lower plenum, completing the recirculation loop.

This advanced modeling approach, which excluded the artificial “jet” channel from the core model, represented the actual plant water flow rates in a much more realistic manner. While the simplified circulation loop in the previous model provided a basic total flow around the core discretization, the explicit description of the jet pump model established a highly accurate core flow and an accurate water circulation profile within the vessel. This circulation profile plays a critical role in heat ejection transients from the core and directly impacts the onset and timing of core degradation.

To achieve these specific jet pump characteristics, the thermal-hydraulic behavior of the Peach Bottom plant was modeled natively in ASTEC. The hydraulic performance of the jet pumps is characterized by two dimensionless ratios: the mass flow ratio (M) and the head ratio (N). These parameters define the efficiency of momentum transfer between the high-velocity drive flow and the lower velocity suction flow (Narabayashi *et al.*, 2006). The overall efficiency of the jet pump is defined as the product of these two parameters. Specifically, the M parameter is defined as the

ratio of the suction mass flow rate to the drive mass flow rate, while the N parameter is the pressure ratio between the suction section and the driving section across the drive nozzle.

5.2.4 **Primary containment vessel and building model**

Unlike the core and recirculation systems, the containment geometry remains unaffected by the fuel assembly upgrades. Therefore, the primary and secondary containment models described in this section were applied identically to both the historical 7x7 and the modernized 10x10 core configurations.

The containment section of the ASTEC model for Peach Bottom Unit-2 was divided into two main domains: first the PCV, which comprises the drywell, the wetwell, and their connecting vent columns. Rest of the surrounding containment zones corresponds reactor building sections. To model the SRVs, a specific nodalization strategy was required due to code constraints. Because submerged relief valve pipes in the wetwell can only be constructed between two distinct containment zones in ASTEC, a transitional mock-up zone designated as “ZON_1” was defined between the main steam line volumes and the wetwell pool. General layout of the PCV and reactor building zones and their connections are given in Figure 5-9.

In order to simulate structural degradation under severe accident conditions, two distinct failure modes were defined for the containment zones. The first failure mode was established between the wetwell zone and the torus room zone (RB-TORUS), with a rupture condition triggered if the pressure within the wetwell exceeded 1.2 MPa. The second failure mode was defined between the drywell zone (DW) and the refueling bay zone in the reactor building (RB-REFUE), representing the failure of the drywell head flange. This failure criterion was dependent on both temperature and pressure. When the temperature in the drywell reached 644 K, the head flange material was assumed to lose its elasticity. Subsequently, a pressure increase to 0.565 MPa would initiate a break in the flange. This break was modeled dynamically; the size of the leakage area was pressure-dependent, expanding from 0.0 m^2 at 0.565 MPa up to a maximum of 0.04 m^2 at 1.378 MPa.

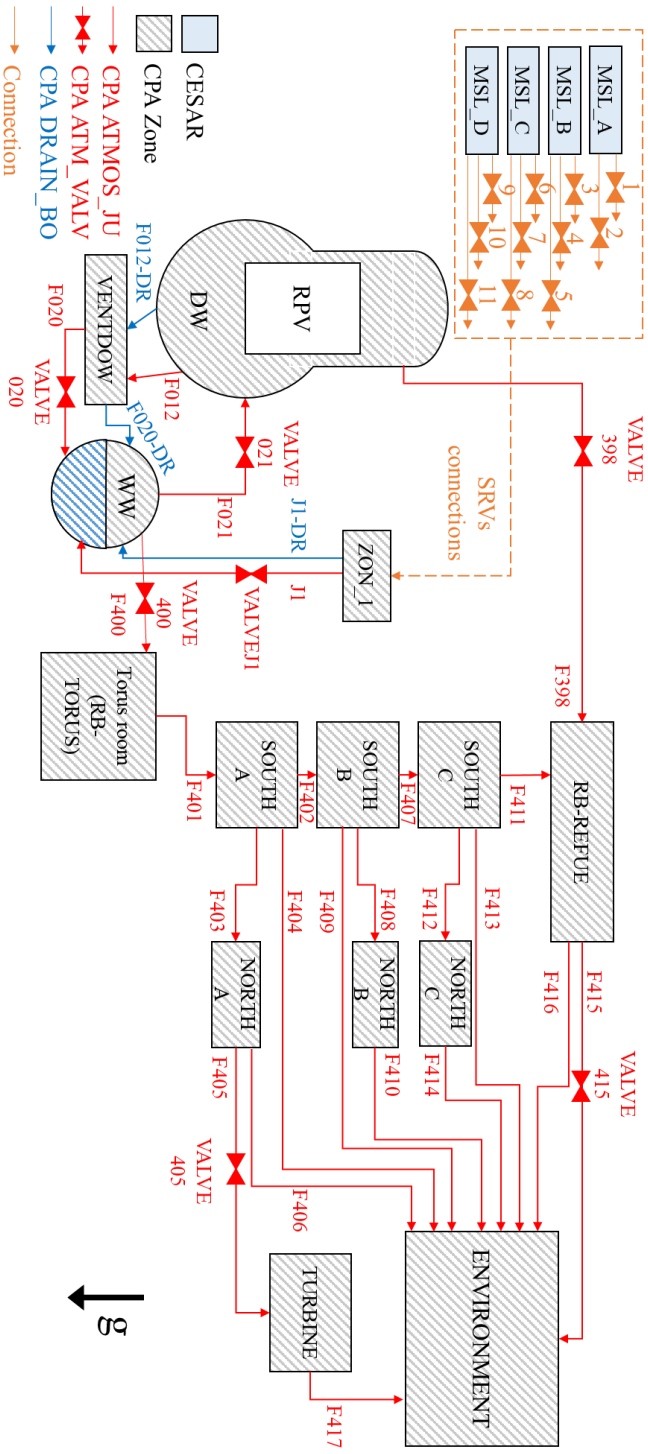


Figure 5-9 Primary Containment Vessel and reactor building zones of Peach Bottom Unit-2 ASTEC Model (Murat *et al.*, 2023).

5.2.5 Selected ASTEC-models for the simulation of key severe accident phenomena

In order to simulate conduction heat transfer within the defined solid structures and between adjacent structures in physical contact, the CONDAUTO module was activated. Convective heat transfer between the fluid flow and the surfaces of the solid structures was modeled using the CONVAUTO module. Radiative heat transfer was handled by two distinct modules: RADR and RADASSEM. Prior to material relocation and cavity formation, the RADR module simulated the radiative heat exchanges. Once a cavity formed due to degradation, the RADASSEM module took over these calculations. Finally, heat transfer within the molten pool in the lower plenum was evaluated using the POOL module with the MAYINGER option, which assumes a homogeneous temperature distribution within the pool.

The oxidation of the zircaloy, stainless steel, and boron carbide structures was modeled using the ZROX, FEOX, and BCOX modules, respectively. The eutectic interaction between the stainless steel and boron carbide was activated via the BCSS module. Additionally, the eutectic interaction between the zircaloy cladding and the UO_2 active fuel material was defined using the UZRL module; the presence of oxidized Zircaloy (ZrO_2) causes the dissolution and subsequent early relocation of the UO_2 material. Finally, the oxidation of the molten mixture, referred to as magma, was calculated using the UZOXMAG module.

Regarding the mechanical behavior of the solid structures, the CREE module was activated to simulate the creep behavior of the zircaloy fuel claddings. The broader structural integrity of the materials was evaluated using the INTE module. For the fuel material, if the temperature exceeded 2500 K, the status of the structure was set to “DISLOCAT”, indicating the onset of material dislocation and allowing for fission product transfer. This same integrity condition was applied to the zircaloy fuel channel boxes. For the zircaloy fuel cladding, the condition was set to “DISLOCAT” if the temperature exceeded 2300 K and the oxide thickness was less than 250 µm. Furthermore, the loss-of-integrity criterion for the lower plenum wall structure was based on a temperature limit derived from the reference study (Carbajo, 1993). If the temperature of any mesh along the lower plenum wall exceeded 1723 K, that specific mesh lost its integrity, resulting in localized cavity formation and structural failure at that point.

5.3 Verification of ASTEC steady state predictions against reference plant data

Before initiating any severe accident transient simulation, it is essential to verify that the integral plant model can stably and accurately reproduce the nominal operating conditions of the reactor. Achieving an acceptable steady-state initialization ensures that the starting thermal-hydraulic parameters such as mass flow rates, pressure distributions, and coolant inventories are physically correct. If these initial boundary conditions are inaccurate, the subsequent accident progression, degradation timeline, and source term release will be fundamentally not correct. Therefore, 500-second steady-state calculations were conducted to initialize and verify both the historical and modernized core configurations.

For the baseline historical model, a 500-second steady-state calculation was executed, and the resulting nominal plant parameters are summarized in Table 5-4. In this configuration, a lower pressure at the core inlet and the corresponding lower saturation temperature resulted in a higher amount of steam production and an increased overall void fraction within the core.

Table 5-4 Peach Bottom Unit-2 design parameters and ASTEC Model steady state results (Murat *et al.*, 2023).

Reference Design Parameters (Larsen, 1978)		ASTEC
Core Power (MW)	3293	3293
Feedwater mass flow rate (kg/s)	1679.68	1673.83
Total mass flow rate (kg/s)	12914.78	12914.89
Core mass flow rate (kg/s)	11336.75	11336.84
Bypass mass flow rate (kg/s)	1578.03	1578.05
Steam mass flow rate (kg/s)	1685.98	1673.83
Steam temperature at dome (K)	559.29	559.38
Core outlet temperature (K)	560.48	559.33
Core inlet temperature (K)	548.53	547.39
Feedwater temperature (K)	464.32	464.32
Dome pressure (MPa)	7.033	7.033
Core outlet pressure (MPa)	7.1564	7.0366
Pressure drop over the core (MPa)	0.152	0.1017
Core inlet pressure (MPa)	7.3084	7.1383
Core exit void fraction	0.65	0.71
Core avg. void fraction	0.304	0.43
RPV water level (m)	14.326	14.278

Because the core design and the overall plant nodalization were significantly updated to accommodate the new power level and to explicitly estimate the fluid flow, the steady-state analysis was repeated for the modernized GE14 10x10 configuration. The results of this 500-second steady-state calculation are given in Table 5-5.

Table 5-5 Peach Bottom Unit-2 updated design parameters and ASTEC Model steady state results (Murat *et al.*, 2024).

Design parameters from UFSAR		ASTEC
Core Power (MWth)	4016	4016
Feedwater mass flow rate (kg/s)	2092.69	2066.58
Total mass flow rate (kg/s)	12914.78	12924.62
Core mass flow rate (kg/s)	11336.75	11330.04
Bypass mass flow rate (kg/s)	1578.03	1577.20
Recirculation flow rate (kg/s)	4309.12	4309.10
Jet Pump N ratio	0.16	0.16
Jet Pump M ratio	1.96	1.99
Feedwater temperature (K)	468.65	468.65
Dome pressure (MPa)	7.239	7.239
Driven flow temperature (K)	548.98	547.03

During this initialization, the total mass flow rate in the revised core design was maintained at the same value established in the foundational core design and operating data report (Larsen, 1978). Furthermore, the explicit modeling of the recirculation line in the updated ASTEC input deck allowed for a direct verification of the jet pump design parameters against the calculated ASTEC model outputs.

As established in the analysis study for the BWR jet pump loop (Narabayashi *et al.*, 2006), the efficiency of the jet pump is defined by the product of its N and M ratios. The M ratio is defined as the ratio of the suction flow rate to the driving flow rate. Physically, the suction flow originates from the water inlet in the downcomer and is entrained by the driving flow, which travels through the external recirculation line. The highly pressurized flow injected from the nozzle drives this suction stream into the mixing throat, where the flow area expands as the mixed stream travels downward. At the exit of the throat section, the combined water mass flows directly into the lower plenum. The N ratio is governed by the system pressure differentials: specifically, it is the ratio of the pressure increase (from the suction region to the exit) to the pressure drop (from the injection nozzle to the exit).

5.4 Analysis of severe accident scenarios in Peach Bottom Unit-2 BWR for the source term prediction

Following development and steady-state verification of the integral ASTEC model, the computational route was deployed to simulate full-scale severe accident transients. The primary objective of these simulations was to calculate the precise radiological source term, the transient mass, timing, and isotopic composition of fission products released from the containment to the

environment. This section details the execution and comparative evaluation of these simulated transients. First, the selected accident sequences are defined, focusing on Short-Term Station Blackout (ST-SBO) events, which historical probabilistic risk assessments have identified as dominant contributors to core damage frequency for BWRs. Following the scenario descriptions, a comparison of the accident progression is presented. This analysis evaluates the thermal-hydraulic behavior, core degradation timelines, structural failure modes, and ultimate fission product releases for both the considered fuel assembly configurations.

In order to evaluate the Peach Bottom Unit-2 NPP, the ST-SBO was selected as the reference transient. Previous safety assessments (Kolaczkowski, et al., 1989) (U.S. Nuclear Regulatory Commission, 1990) indicated that the most significant contributor to the core damage frequency for this specific plant arises from a Loss of Offsite Power (LOSP) followed by the failure of the diesel generators and the rapid depletion of batteries, resulting in an SBO. Furthermore, another study (Leonard, et al., 2007) revealed that an ST-SBO involving a stuck open SRV represents a notably high-risk event. Consequently, these specific SBO transients were chosen for the ASTEC analysis, aligning with foundational reference modeling studies (Carbajo J. , 1993).

In order to comprehensively analyze the radiological source term and evaluate the impact of plant modernization, two distinct accident scenarios were simulated: an ST-SBO, and an ST-SBO with a stuck-open SRV.

5.4.1 Scenario-1: ST-SBO with core loading with 7x7 fuel assemblies

This baseline ST-SBO transient assumes a total loss of all AC power alongside the complete depletion of the required DC power except for the DC power required to start ADS system. Consequently, turbine-driven high-pressure injection systems that rely on DC control logic, such as the RCIC and HPCI systems, fail to actuate. Motor-driven low-pressure systems, such as the LPCI and Core Spray systems, are also completely unavailable due to the AC power loss. The only operational mechanism assumed available to depressurize the core is the automated cycling of the SRVs at their designated setpoints. It is considered that historical 7x7 fuel assemblies are in operation with characterized by lower discharge burnup levels.

Following the loss of all injection capabilities, the reactor pressure vessel is isolated, and decay heat causes the coolant to boil and the system pressure to rise. The SRVs cycle open and closed automatically to discharge steam to the suppression pool, controlling the RPV pressure. Because no make-up water is supplied, the continuous boil-off leads to a gradual uncovery of the core, followed by heat-up, cladding oxidation, and eventual fuel degradation under high-pressure conditions.

5.4.2 Scenario-2: ST-SBO with modern GE14 10x10 fuel assemblies

This scenario utilizes the exact same safety system failure assumptions as Scenario-1, complete loss of AC/DC power only DC power is available for ADS system, failure of all active high-pressure (RCIC/HPCI) and low-pressure (LPCI/Core Spray) injection systems, and reliance only on automated SRV cycling for pressure relief. The critical differing assumption in this scenario is the core loading. It assumes a modernized GE14 10x10 fuel assembly configuration operating at significantly higher discharge burnup levels, meaning the core contains larger initial fission product inventory and generates a higher level of decay heat.

In order to directly compare the consequences of fuel design evolution on the accident progression, this transient tracks the same sequence of events (SRV cycling and boil-off) as the historical core. However, the assumed increase in decay heat from the modern assemblies accelerates the thermal-hydraulic response. This leads to faster coolant depletion, earlier core uncovery, and a significantly accelerated and more severe degradation timeline compared to the baseline scenario.

5.4.3 Scenario-3: ST-SBO with modern GE14 10x10 fuel assemblies with stuck open SRV

This scenario assumes the same modern GE14 10x10 high-burnup core loading and the same complete initial failure of all AC/DC power and active injection systems as Scenario-2. However, an additional mechanical failure assumption is introduced based on historical high-risk event studies (Leonard, Gauntt and Powers, 2007). It is assumed that after the initial actuation of the SRVs, a mechanical fault occurs, resulting in a stuck-open SRV condition shortly after the transient begins (200 seconds after automated operation).

The assumption of a stuck-open valve causes a continuous, uncontrolled blowdown of the RPV steam inventory directly into the suppression pool. Unlike other considered transients, uncontrolled operation of the SRV and continues discharge of steam to the suppression chamber alters the accident progression significantly.

5.5 Analysis of the Scenario-1: ST-SBO with core loading with 7x7 fuel assemblies

For the baseline historical 7x7 fuel assembly configuration, the Short-Term Station Blackout (ST-SBO) scenario was simulated. The sequence of events—from the initiating Loss of Offsite Power (LOSP) and safety relief valve (SRV) operations up to the ultimate basemat rupture—is summarized in Table 5-6. The transient simulation was terminated when the erosion of the basemat concrete reached the cavity border.

Table 5-6 Peach Bottom Unit-2 ASTEC Model Short-Term Station Blackout transient instants (Murat *et al.*, 2023).

Sequence of Events	Time (s)
SRV-1 starts operation	0
SRV-1 stops operation, Manual operation of a SRV starts	200
First cladding creep rupture, start of the fission product release	1037
First material slump in lower plenum	1142
First slump of corium with fission products in lower plenum	1158
First appearance of a cavity in core	1167
Manual operation of a SRV stops, ADS actuates	3867
First total core uncovery	6772
Lower head vessel failure	13361
PCV head flange failure	13415
Basemat rupture	88142

During the first 200 seconds of the transient, automated SRV operation was simulated to represent the timeframe before operators could take manual control. Subsequently, manual SRV operation was maintained between the 6.49 and 7.18 MPa pressure set points. The pressure level within the vessel is shown in Figure 5-10; the pressure oscillations observed during the first 200 seconds correspond to the higher pressure set points of the automated SRV.

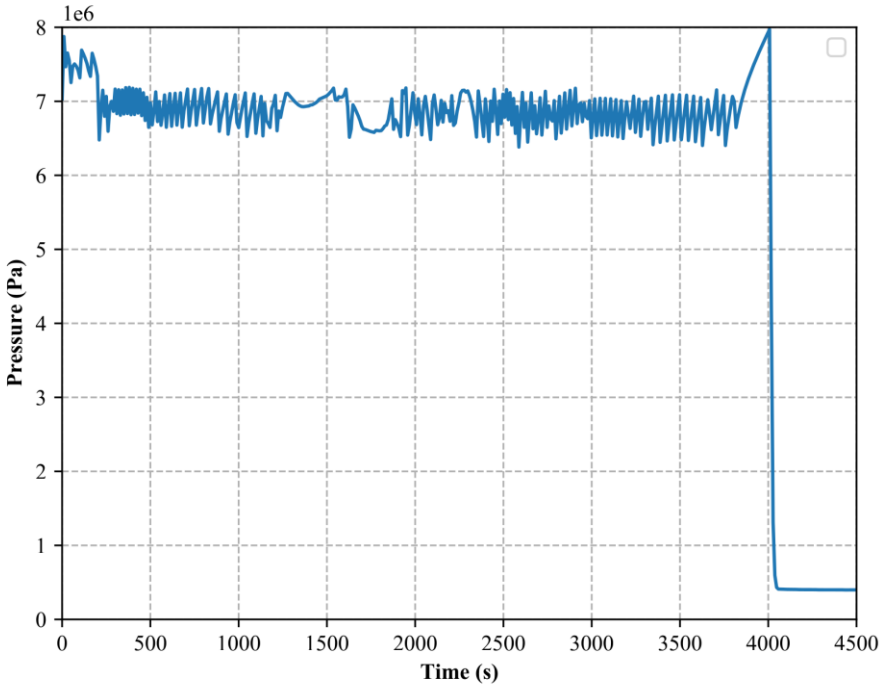


Figure 5-10 Pressure in the vessel during operation of the safety relief valve and automatic depressurization system (Murat *et al.*, 2023).

This manual SRV operation was maintained until the ADS was activated. When the water level in the core dropped to one-third of the active core height, five responsible SRVs were activated simultaneously to rapidly depressurize the vessel. Excess heat and steam were transferred to the wetwell pool through these opened valves. At 3867 seconds, the water level reached this trigger point, and SRVs 1, 2, 3, 5, and 6 were opened. As seen in Figure 5-10, a sudden and steep decrease in vessel pressure occurred as soon as the ADS activated.

The water level progression in the vessel until it dropped below the first core mesh at 6772 seconds is illustrated in Figure 5-11. The acronyms TAF and BAF refer to the Top of Active Fuel and Bottom of Active Fuel, respectively. The “DCTOP” volume above the core level contains the vessel's primary water storage. From the beginning of the transient, SRV operations led to coolant mass escaping and a corresponding drop in the water level. Once the water inventory in the DCTOP volume was depleted, the water level within the core domain began to drop. When the ADS actuated, a temporary peak in the water level was observed, immediately followed by a sudden decrease due to rapid steam flashing.

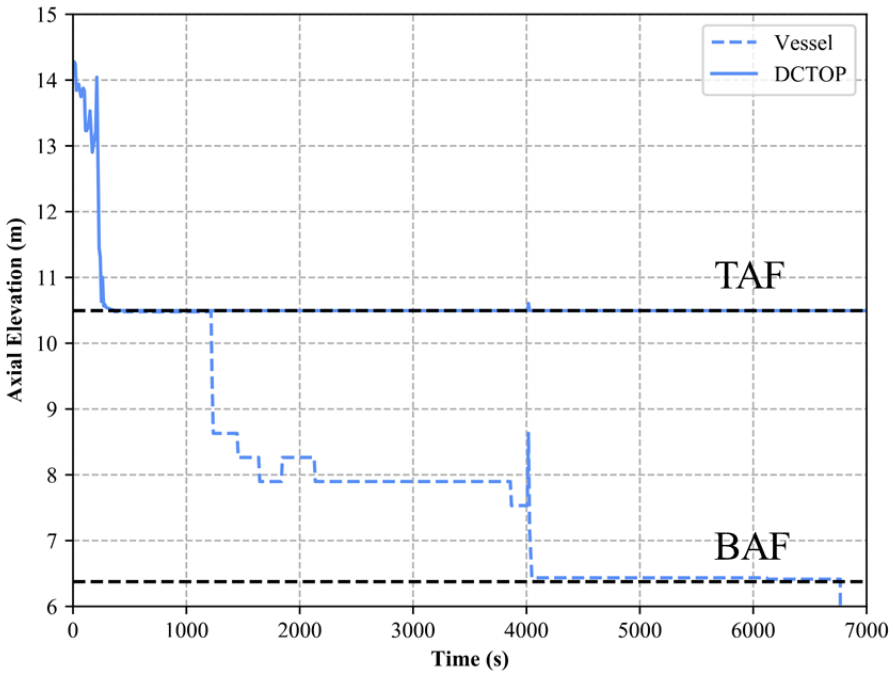


Figure 5-11 Water level in DCTOP volume and in the core up to first total uncover (Murat *et al.*, 2023).

In this high-temperature steam environment, oxidation reactions on the solid structure surfaces accelerated rapidly. These elevated temperatures led to the first zircaloy creep ruptures and the onset of severe oxidation. The hydrogen generation resulting from these oxidation reactions is presented in Figure 5-12. Following the initial cladding rupture and the formation of the first localized cavity in the core at 1000 seconds, the oxidation rate increased significantly. A subsequent surge in the reaction rate was observed after ADS actuation, as the rapid depressurization converted the remaining liquid water intake into steam. By the end of the in-vessel degradation phase, 1847.62 kg of hydrogen was produced. The BWR-specific fuel channel boxes which are made of the same Zircaloy material as the fuel cladding, introduced a large amount of additional material into the core domain. An isolated investigation of these structures revealed that the fuel channel boxes alone accounted for approximately 350 kg of the total hydrogen production (Figure 5-13). Compared to the approximately 500 kg of hydrogen generated by the fuel cladding, the channel boxes represented a highly significant proportion of the total hydrogen production.

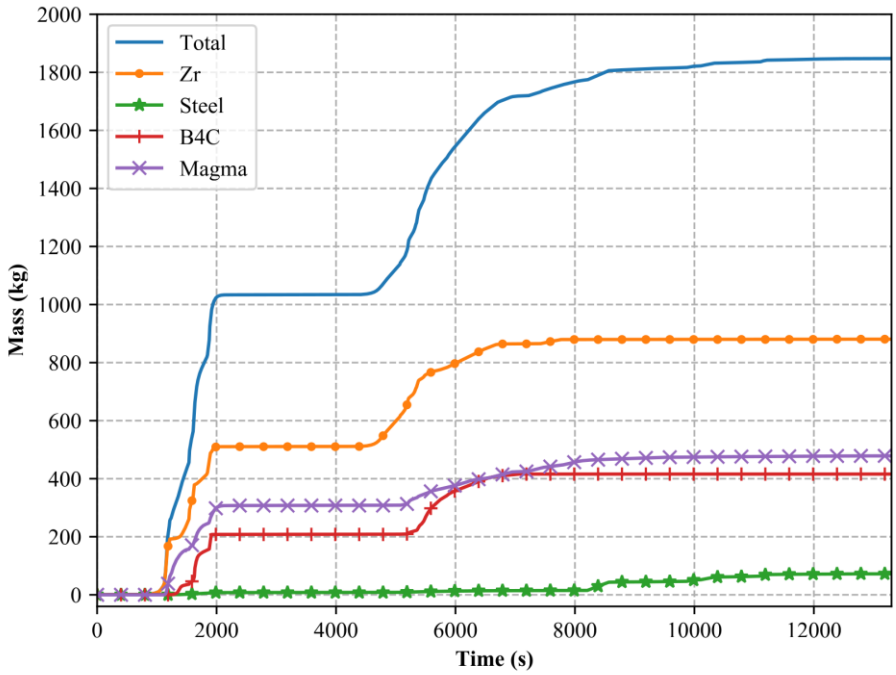


Figure 5-12 Cumulative hydrogen production resulted by the oxidation reaction in the core up to lower plenum failure (Murat *et al.*, 2023).

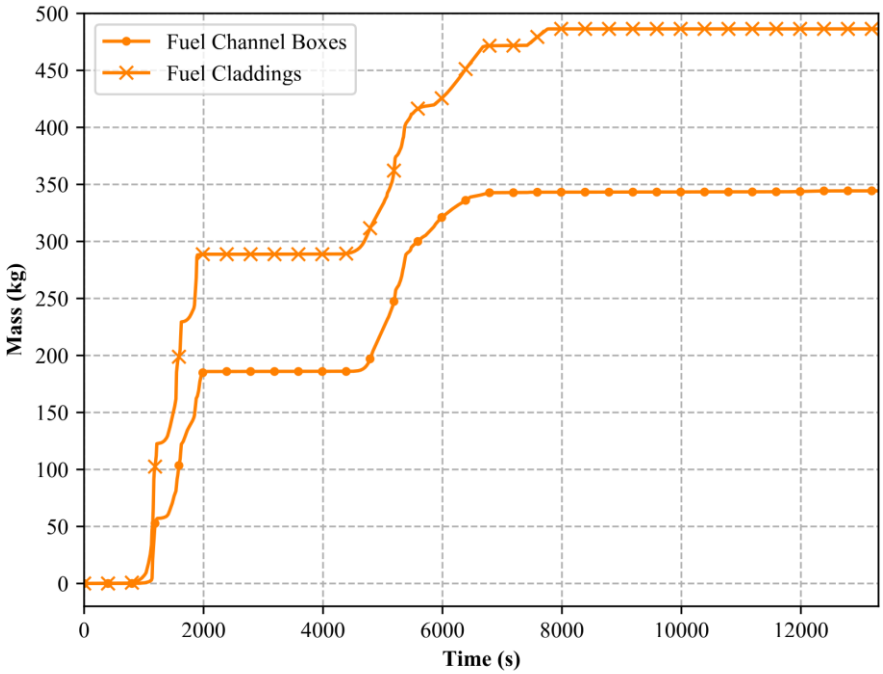


Figure 5-13 Cumulative hydrogen production resulted by the zircaloy oxidation reaction in the core up to lower plenum failure (Murat *et al.*, 2023).

Following the initial material slump into the lower plenum at 1142 seconds, molten material continued to accumulate until the lower plenum failed at 13361 seconds. The formation of corium layers and their respective masses during this in-vessel phase are detailed in Figure 5-14. The layers were defined as follows: MAGMA1 (heavy metallic layer), MAGMA2 (oxide layer), MAGMA3 (light metallic layer), and DEBRIS2 (solid debris accumulated on top of the magma layers). The temperature map of the core and lower plenum at the exact instant of lower head failure is shown in Figure 5-15. The axial location of the failure mesh was between -6.08 m and -5.88 m. Following this failure, a total of 152.34 tons of corium mass was ejected from the lower plenum.

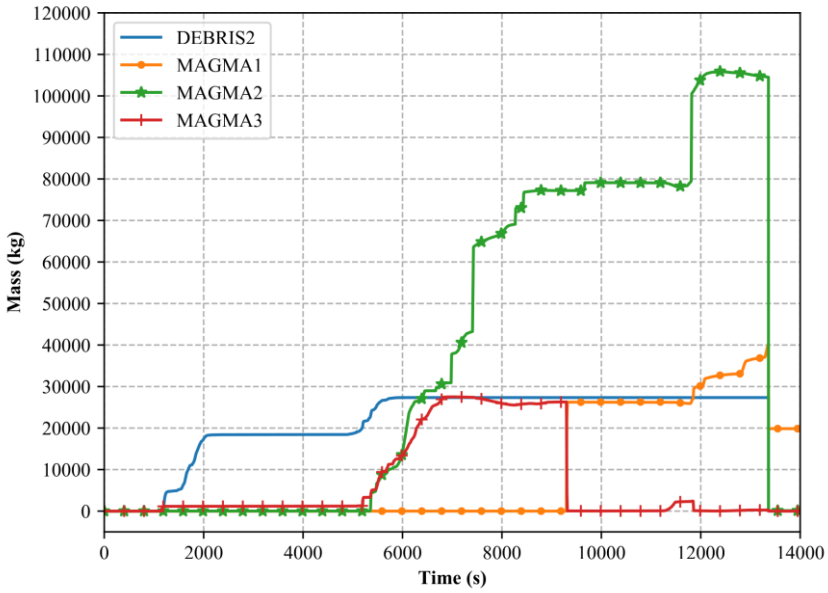


Figure 5-14 Corium layer masses in the lower plenum (Murat *et al.*, 2023).

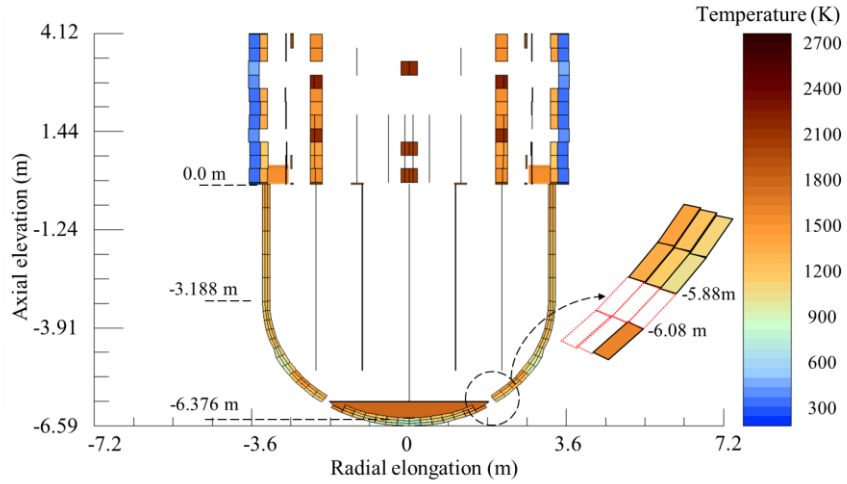


Figure 5-15 Core and lower plenum domain of the ASTEC Model of the Peach Bottom Unit-2 NPP at the lower plenum failure instant (Murat *et al.*, 2023).

This failure timeline can be compared to the reference study (Carbajo, 1993), which considered two cases: one with debris quenching in the lower plenum, and one without. In the reference case considering debris quenching, control rod drive penetration failure occurred at 17128 seconds, and total lower head failure occurred at approximately 28000 seconds, resulting in 279.52 tons of ejected material. In the reference case without quenching, total lower head failure occurred much earlier (9760 seconds) with around 180 tons of ejected material. Because the ASTEC model of Peach Bottom Unit-2 actively calculated heat transfer between the residual water and the debris layer, the resulting lower plenum failure at 13415 seconds fell between these two extremes. Furthermore, because the reference study included a larger mass of solid internal structures (greater thermal inertia) in the lower plenum, it predicted a higher total ejected mass and a delayed failure time compared to the ASTEC model.

The active operation of the SRVs transferred massive amounts of mass and energy from the vessel directly into the containment zones. Although the wetwell water pool is designed to suppress excess energy and condense steam, the continuous injection of superheated steam and non-condensable fission products caused a steady pressure increase in the wetwell and the connected drywell. The pressure level in the drywell is shown in Figure 5-16. The described failure mode for PCV, which is drywell head flange failure, was programmed to activate when the temperature reached 644 K and the pressure exceeded 0.565 MPa. Although the pressure exceeded 0.565 MPa shortly after ADS operation at 3867 seconds, the gas temperature had not yet reached 644 K. However, as soon as the lower plenum failed at 13361 seconds and corium slumped into the reactor cavity, which is part of the drywell zone, the temperature limit was exceeded. This triggered the drywell head flange failure, creating a pressure-dependent break that

allowed fission products to transfer from the Primary Containment Vessel (PCV) into the reactor building and, ultimately, the environment. At the end of the transient, corresponding with the basemat rupture, the total mass of fission products released to the environment was recorded Table 5-7.

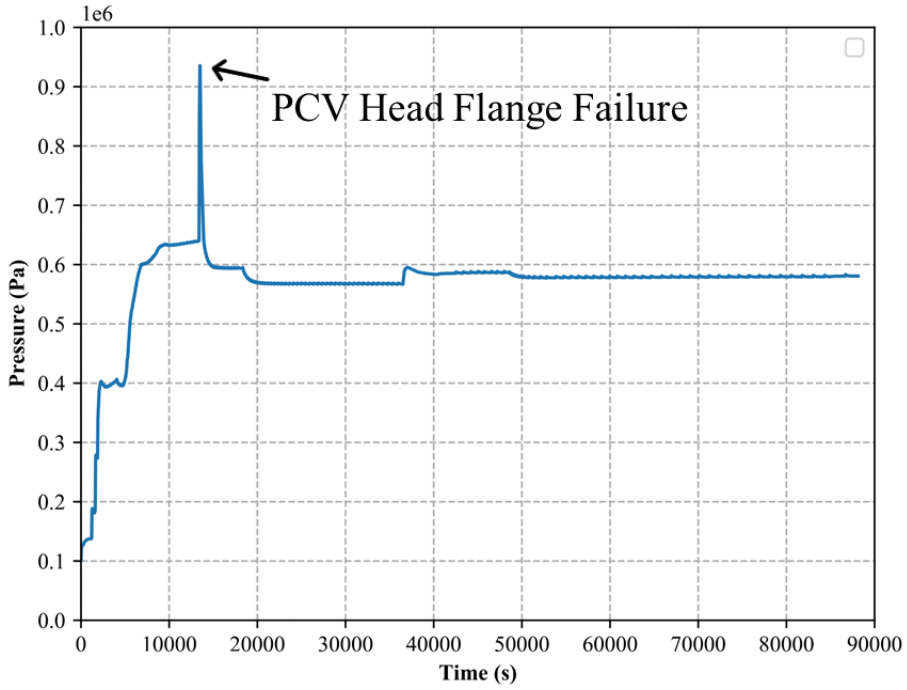


Figure 5-16 Pressure in the drywell zone (Murat *et al.*, 2023).

Table 5-7 Fission product inventory in the core at the beginning and their fractions in the specified sections at the end of the simulation.

Elements	Initial core Inventory (kg)	Primary [-]	Containment [-]	Environment [-]
Kr	30.17	0.010	0.780	0.198
Xe	416.56	0.0101	0.780	0.198
I	15.74	0.083	0.704	0.031
Sb	1.28	0.074	0.590	1.44E-3
Te	36.66	0.134	0.462	9.53E-4
Ag	5.33	0.138	0.645	1.54E-3
Cs	228.50	0.148	0.653	1.68E-3
Rh	37.39	0.0	0.0	3.57E-8
Mo	255.48	0.175	0.352	5.92E-4
Ba	110.40	0.103	0.261	2.20E-4
Sr	76.78	0.018	5.87E-3	1.81E-5
Y	39.60	1.50E-12	7.84E-21	2.97E-8
Nb	4.21	0.0	0.0	2.37E-21
Ru	183.80	0.018	0.011	2.05E-5
Ce	228.58	0.014	0.015	1.66E-5
La	97.93	1.40E-3	1.71E-3	1.65E-6
Eu	9.12	3.45E-4	6.75E-4	4.33E-7

5.6 Analysis of the Scenario-2: ST-SBO with modern GE14 10x10 fuel assemblies

In order to assess the impact of modernized core designs, the same ST-SBO sequence was simulated using the updated GE14 10x10 fuel assemblies. The sequence of events for both the historical 7x7 and modern 10x10 configurations is compared in Table 5-8.

Table 5-8 Short-Term Station Blackout sequence of events comparison between old (7x7) and new (10x10) fuel (Murat *et al.*, 2024).

Sequence of Events	Time (s) 10x10 ST-SBO	Time (s) 7x7 ST-SBO
SRV-1 starts operation	0	0
SRV-1 stops operation, lower pressure set point of a SRV operation	200	200
First cladding creep rupture, start of the fission product release	524	1037
First material slump in lower plenum	622	1142
First slump of corium with fission products in lower plenum	643	1158
First appearance of a cavity in core	648	1167
Manual operation of a SRV stops, ADS actuates	4782	3867
First total core uncovery	9959	6772
Lower head vessel failure	21616	13361
PCV head flange failure	26137	13415
Basemat rupture	100576	88142

Loss of fuel integrity occurred significantly earlier for the GE14 10x10 assemblies compared to the historical 7x7 design. Because the 10x10 assemblies operate at a much higher discharge burnup (46.47 MWd/t compared to 17.5 MWd/t), the accumulated decay heat in the core was proportionally larger, accelerating the initial temperature escalation. Figure 5-17 illustrates this difference, one hour after the reactor scram, the decay heat in the modernized core was approximately 10 MW higher than in the historical core. However, despite this earlier initial fuel failure, the total uncovery of the core, the vessel failure, and the containment failure were all delayed to later stages in the modernized model.

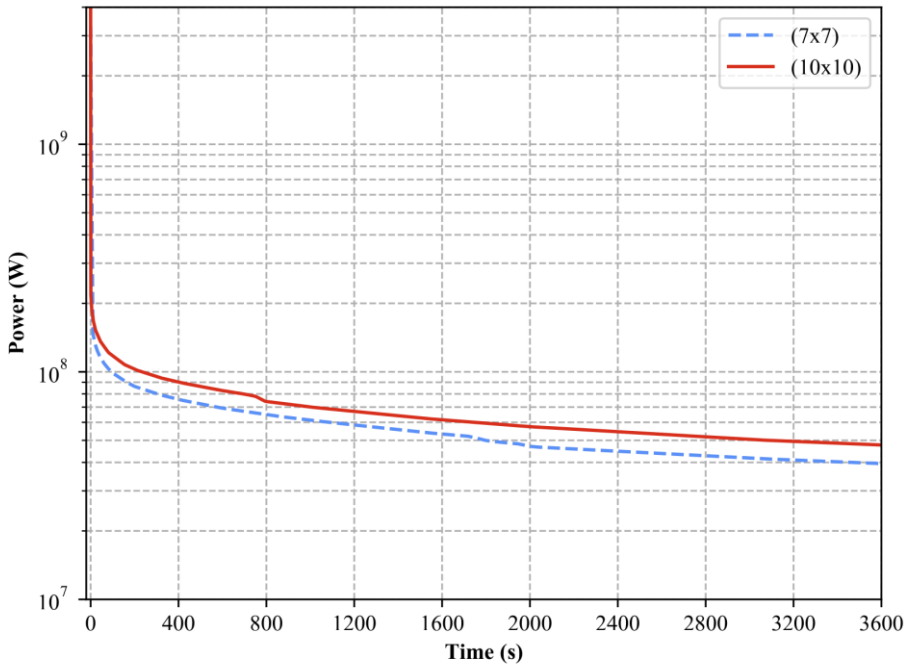


Figure 5-17 Comparison of power levels of the cores between 10x10 and 7x7 fuel assemblies (Murat *et al.*, 2024).

The vessel pressure progression for both cases is shown in Figure 5-18. Because the SRV operating ranges were identical, the vessel pressure behavior was highly similar up to the point of ADS actuation. However, the timing of the ADS activation is strictly dependent on the core water level, which progressed differently in the modernized model. The updated ASTEC nodalization allowed for a much more accurate representation of the recirculation flow. In the 7x7 model, the recirculation pumps were stopped entirely when SRV operation began. The updated 10x10 model correctly accounted for the fact that only one-third of the total core flow resides in the recirculation lines; therefore, upon scram, only that specific flow fraction was cut. This resulted in a much more gradual decrease in the core water level, meaning the modern fuel structures remained exposed to liquid water and cooling for a longer duration. Water level comparison between two model is given in Figure 5-19.

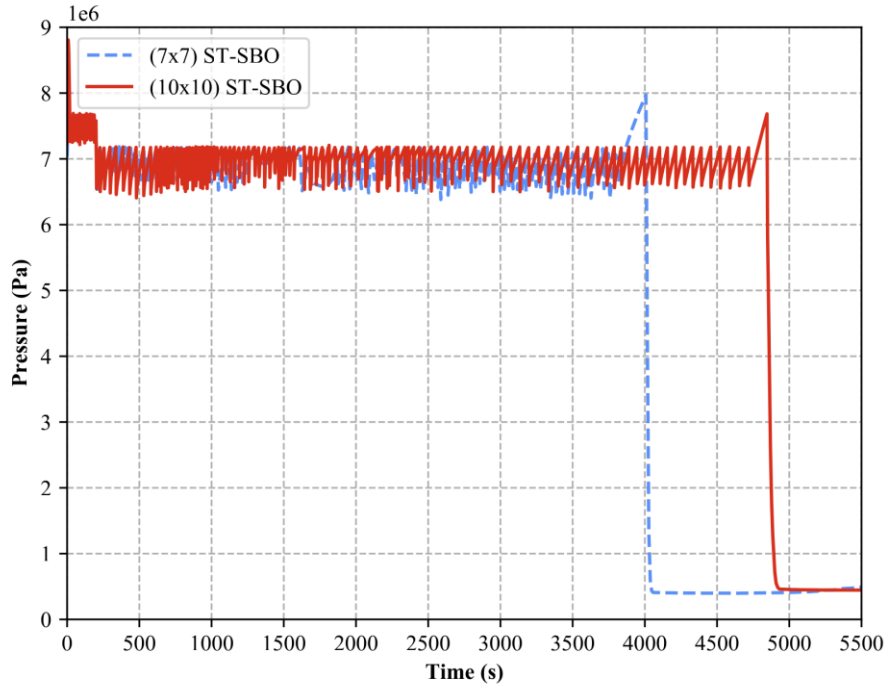


Figure 5-18 Comparison of vessel pressures between models which uses 10x10 and 7x7 fuel assemblies (Murat *et al.*, 2024).

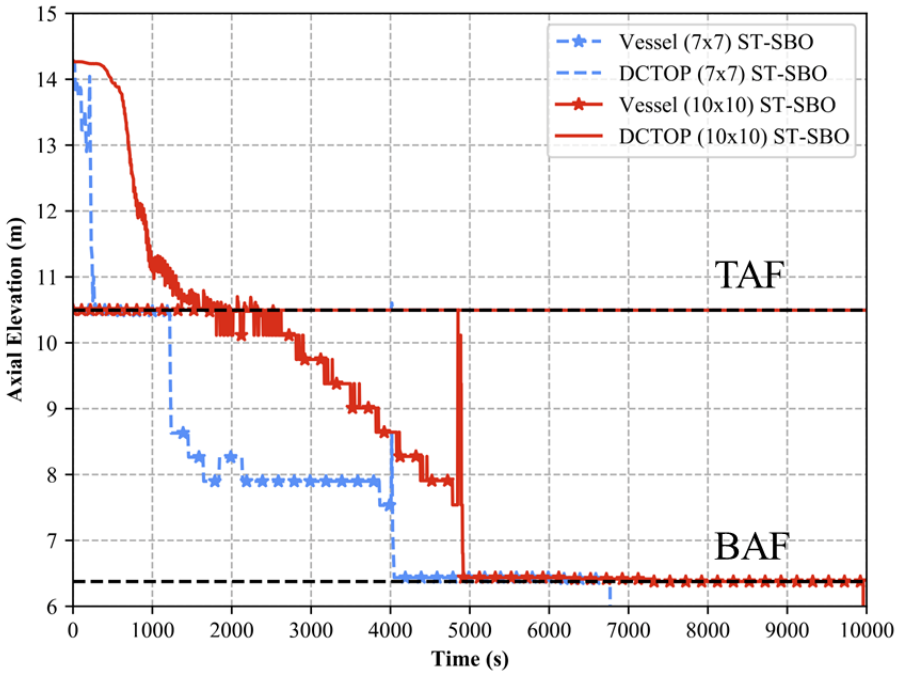


Figure 5-19 Comparison of water levels between models which uses 10x10 and 7x7 fuel assemblies (Murat *et al.*, 2024).

Because the loss of fuel integrity and slump relocation occurred earlier in the 10x10 design, the interaction between the high-temperature material surfaces and the steam environment accelerated rapidly once the water level finally dropped. A much faster ramp-up in hydrogen production was observed. Not only were the oxidation kinetics initiated earlier, but the modernized 10x10 core also contains a larger total mass of Zircaloy, providing more available surface area for oxidation. Consequently, a total hydrogen generation of 2138.31 kg was observed at the end of the in-vessel phase (Figure 5-20).

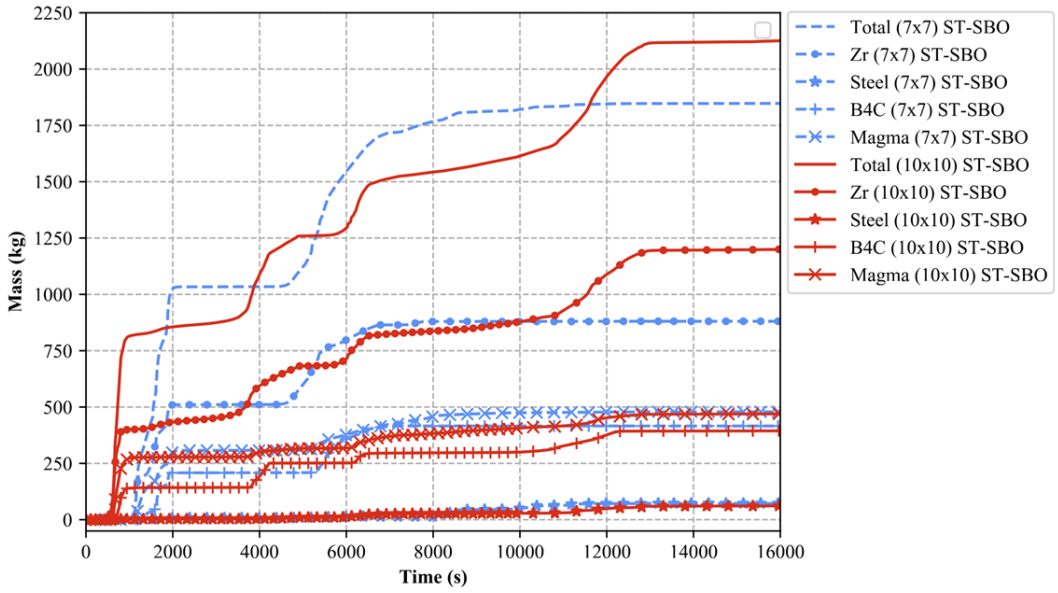


Figure 5-20 Comparison of hydrogen production resulted by oxidation between models which uses 10x10 and 7x7 fuel assemblies (Murat *et al.*, 2024).

The slump accumulation, corium layer fragmentation, and respective masses in the lower plenum for the 10x10 core are presented in Figure 5-21. During accumulation, as a molten material only MAGMA2 (oxide) and MAGMA3 (light metallic) layers formed. Upon lower plenum failure, a total of 210.48 tons of corium was ejected. However, a massive amount of molten material was retained in the in-vessel domain; as seen in Figure 5-21, more than 120 tons of the oxide layer was not transferred to the cavity. Because the modernized model predicted a higher axial failure location on the lower plenum wall compared to the previous model, complete drainage was prevented. The failure point and vessel condition at the exact instant of lower head failure are shown in Figure 5-22. As seen in the figure, a larger amount of solid material remained intact in the mid-lower core sections compared to the previous model, primarily because the modernized core was exposed to water cooling for a longer initial period.

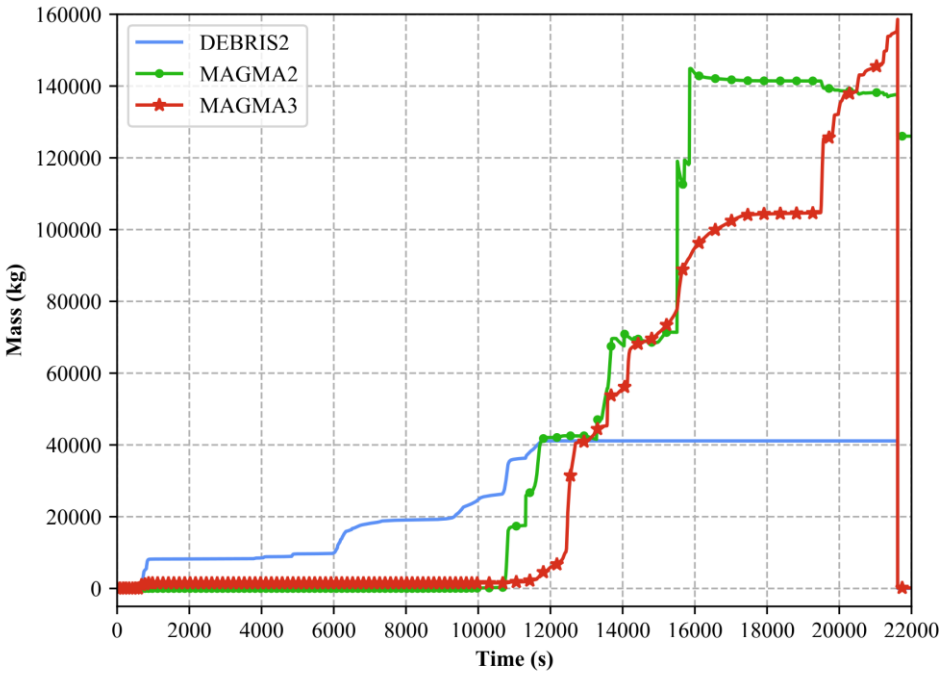


Figure 5-21 Corium layer masses in the lower plenum (Murat *et al.*, 2024).

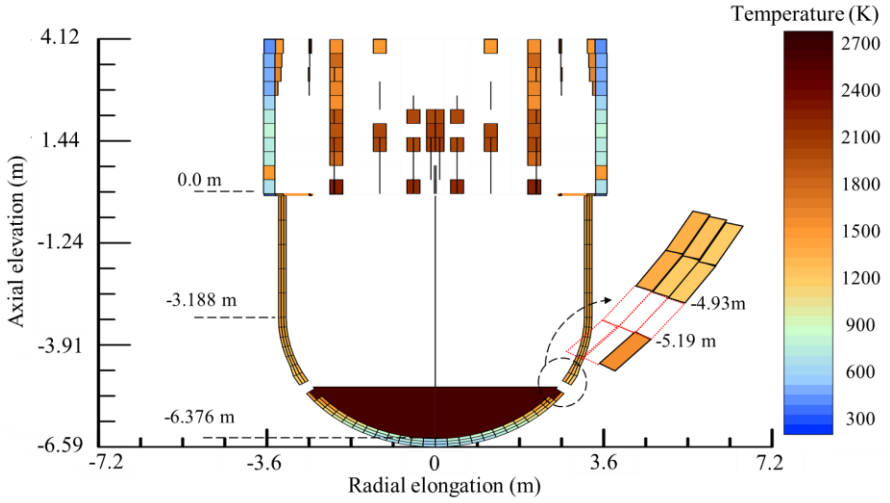


Figure 5-22 Core and lower plenum domain of the ASTEC Model of the Peach Bottom Unit-2 NPP at the lower plenum failure instant (Murat *et al.*, 2024).

Containment failure followed the same drywell head flange failure mode observed in the previous design. The earlier slump formation and corium accumulation in the cavity resulted in a slightly earlier pressure increase in the wetwell and drywell. Lower head failure was delayed to 21616 seconds in the new design and the pressure increases followed until the failure instant. Following the lower head failure, a sudden pressure jump was observed, and the 644 K

temperature limit in the drywell was reached at 26137 seconds, triggering the flange failure (Figure 5-23). Fission product releases to the environment continued until the basemat concrete rupture occurred at 100576 seconds; the final fractions of the fission product inventories in each domain are provided in Table 5-9.

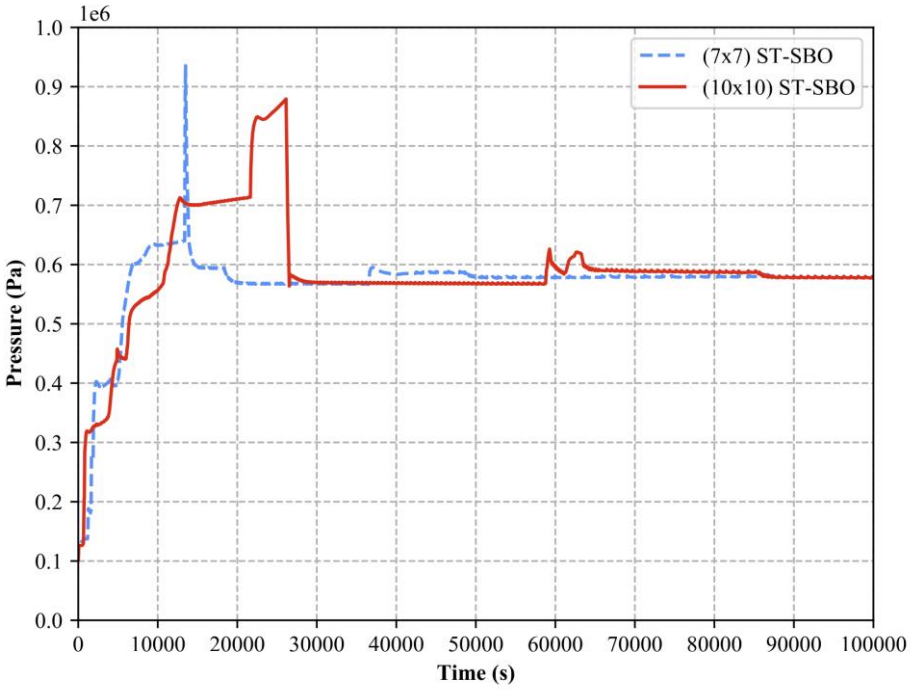


Figure 5-23 Comparison of drywell zone pressure between models which uses 10x10 and 7x7 fuel assemblies (Murat *et al.*, 2024).

Table 5-9 Fission product inventory in the core at the beginning and their fractions in the specified sections at the end of the simulation (Murat *et al.*, 2024).

Elements	Inventory (kg)	Primary	Containment	Environment
Kr	68.60	0.105	0.499	0.264
Xe	1025.79	0.105	0.499	0.264
I	36.66	0.172	0.664	0.025
Sb	2.81	0.115	0.572	5.38E-4
Te	93.41	0.141	0.449	3.95E-4
Ag	7.30	0.206	0.657	5.53E-4
Cs	556.56	0.185	0.698	6.77E-4
Rh	79.54	9.85E-5	2.02E-4	1.66E-8
Mo	644.51	0.096	0.402	2.78E-4
Ba	290.09	0.230	0.323	8.08E-5
Sr	166.72	0.152	0.029	6.59E-6
Y	87.65	9.72E-5	1.98E-5	6.21E-8
Nb	3.80	0.0	0.0	0.0
Ru	479.17	0.088	0.160	1.98E-5
Ce	502.68	0.128	0.115	2.71E-5
La	236.88	0.067	0.031	7.09E-6
Eu	27.98	0.049	0.021	4.24E-6

5.7 Analysis of the Scenario-3: ST-SBO with modern GE14 10x10 fuel assemblies with stuck open SRV

The final sequence of events, representing the ST-SBO with a stuck-open SRV, is compared against all previous cases in Table 5-10. Because the decay heat levels and initial SRV operations were identical to the standard 10x10 ST-SBO scenario, the initial failure of the fuel material showed similar timing. However, the presence of the stuck-open SRV altered the thermal-hydraulic progression, delaying both vessel and containment failure even further than the 7x7 model.

Table 5-10 Peach Bottom Unit-2 ASTEC Model Short-Term Station Blackout and Short-Term Station Blackout with Stuck Open Safety Valve sequence of events including 7x7 and 10x10 fuel assembly designs (Murat *et al.*, 2024).

Sequence of Events	Time (s) 10x10 ST-SBO SOSRV	Time (s) 10x10 ST-SBO	Time (s) 7x7 ST-SBO
SRV-1 starts operation	0	0	0
SRV-1 stops operation, lower pressure set point of a SRV operation	-	200	200
First cladding creep rupture, start of the fission product release	530	524	1037
First material slump in lower plenum	633	622	1142
First slump of corium with fission products in lower plenum	651	643	1158
First appearance of a cavity in core	662	648	1167
Manual operation of a SRV stops, ADS actuates	-	4782	3867
Stuck open SRV-1	5835	-	-
First total core uncovery	13489	9959	6772
Lower head vessel failure	22777	21616	13361
PCV head flange failure	26701	26137	13415
Basemat rupture	116575	100576	88142

In this scenario, uninterrupted SRV operation continued without manual intervention. Because the operational pressure range of SRV-1 is higher than the manual operation interval, the pressure inside the vessel was maintained at a higher level during the early transient. After 270 open-close cycles, the valve was forced into a stuck-open condition, causing the pressure to decrease rapidly (Figure 5-24).

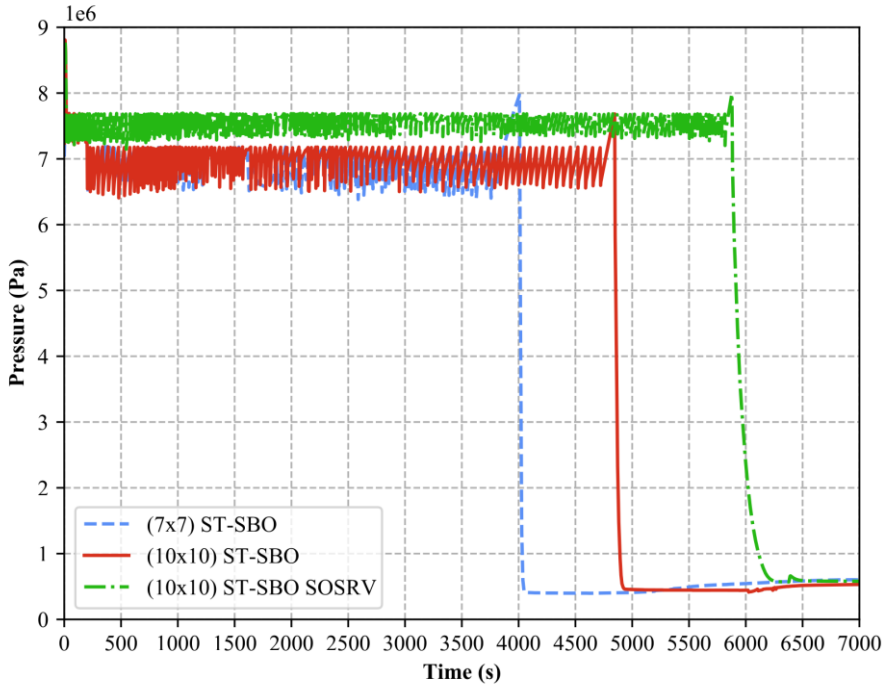


Figure 5-24 Comparison of vessel pressures between models which uses 10x10 and 7x7 fuel assemblies and ST-SBO and ST-SBO SOSRV transients (Murat *et al.*, 2024).

Following on this single stuck-open SRV rather than the sudden actuation of 5 SRVs via the ADS allowed the core to remain submerged for a significantly longer period. Initially, the water level progression was similar to the standard 10x10 ST-SBO. However, the absence of the massive ADS blowdown prevented the sudden, catastrophic drop in water level, allowing the stuck-open SRV scenario to retain liquid water in the core for approximately 1000 seconds longer (Figure 5-25).

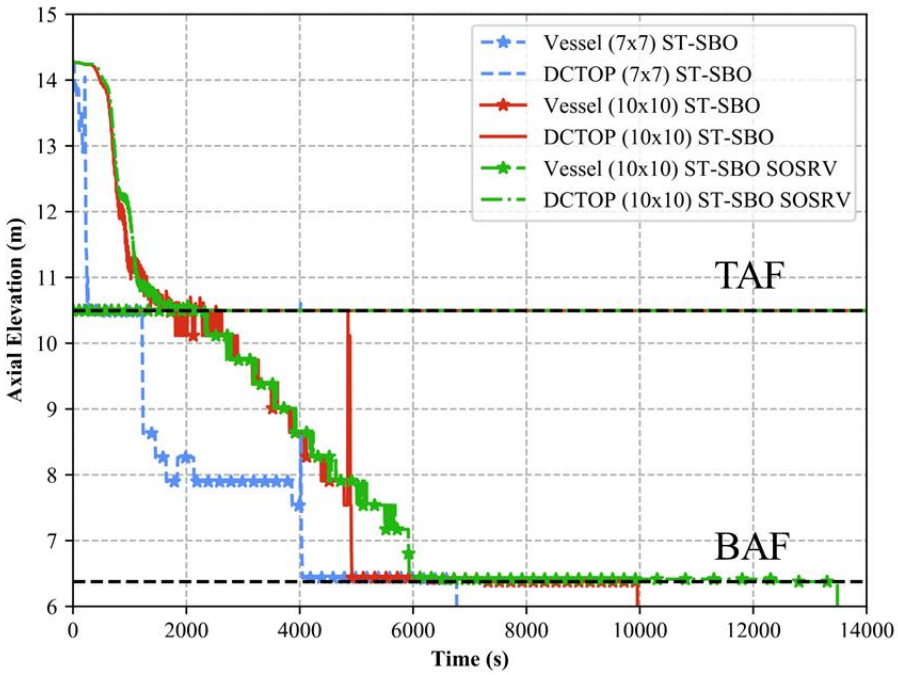


Figure 5-25 Comparison of water levels between models which uses 10x10 and 7x7 fuel assemblies and ST-SBO and ST-SBO SOSRV transients (Murat *et al.*, 2024).

This prolonged water retention heavily influenced the oxidation reaction rates. Because the core did not lose its steam and water environment as rapidly, the prolonged high-temperature steam exposure resulted in an even greater amount of hydrogen generation, totaling 2447.0 kg by the end of the in-vessel phase which its evolution is given in Figure 5-26.

The accumulation of magma layers in the lower plenum up to the point of vessel failure is shown in Figure 5-27. Only 67.26 tons of magma was transferred from the lower head to the cavity. The failure point on the lower head wall (Figure 5-28) was recorded at the highest axial elevation among all the analyzed scenarios. Consequently, only the top debris formation, the light metallic MAGMA1 layer, and a small fraction of the oxide MAGMA2 layer were ejected.

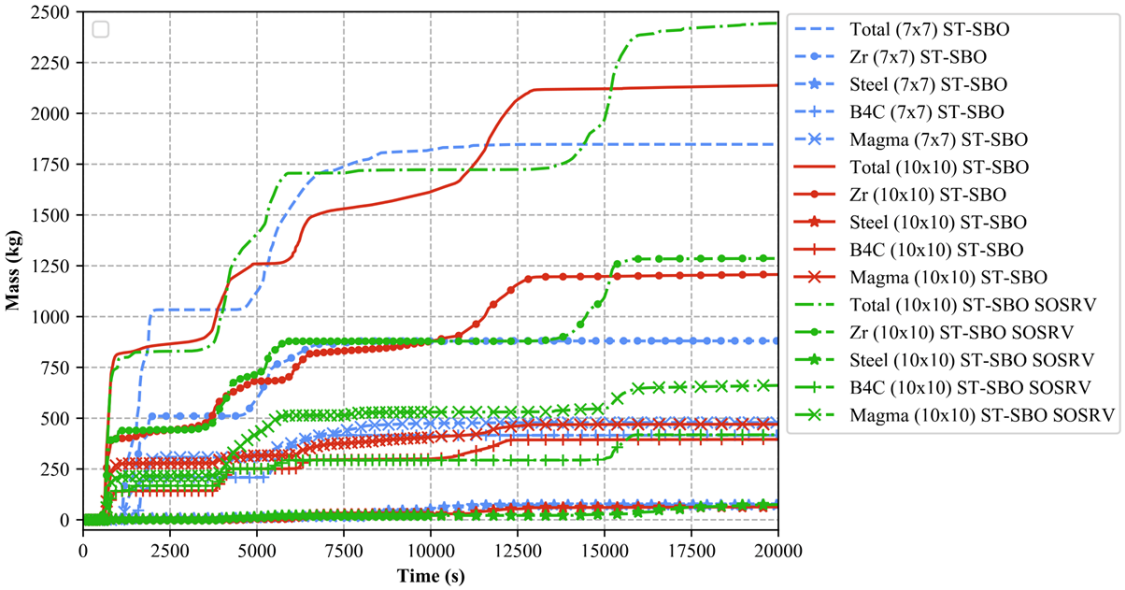


Figure 5-26 Comparison of hydrogen production resulted by oxidation between models which uses 10x10 and 7x7 fuel assemblies and ST-SBO and ST-SBO SOSRV transients (Murat *et al.*, 2024).

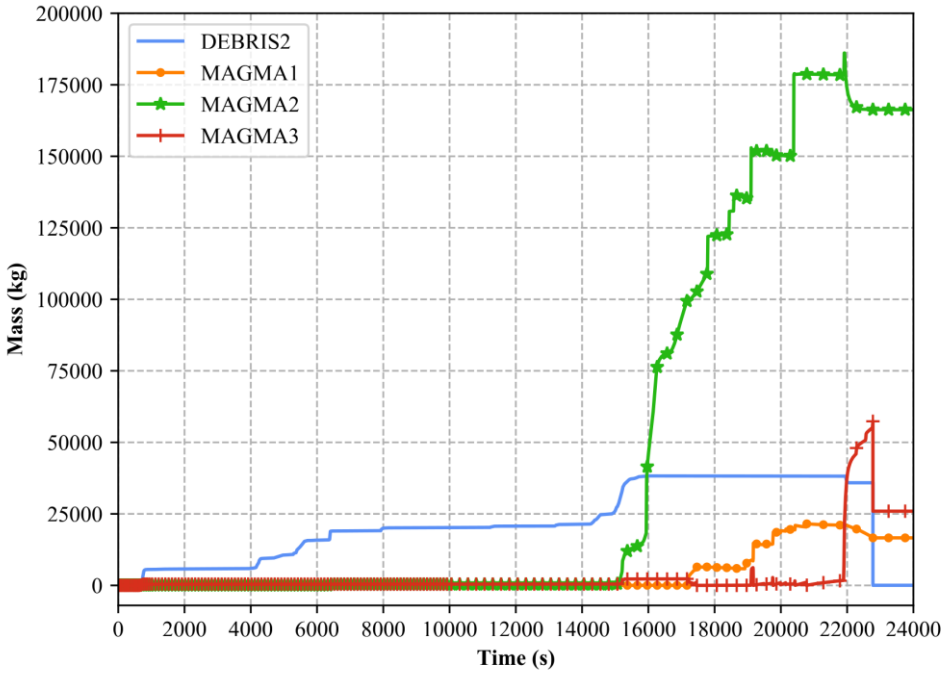


Figure 5-27 Corium layer masses in the lower plenum (Murat *et al.*, 2024).

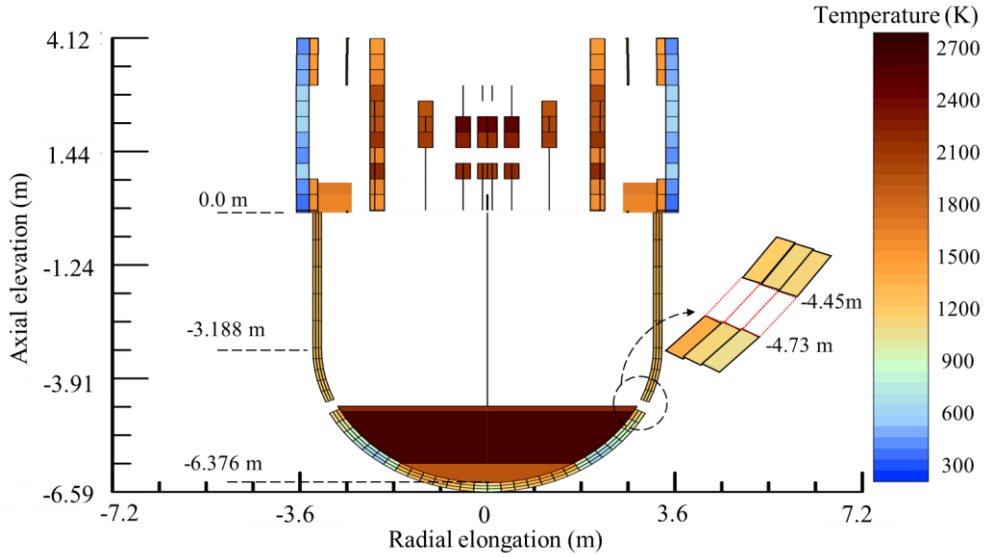


Figure 5-28 Core and lower plenum domain of the ASTEC Model of the Peach Bottom Unit-2 NPP at the lower plenum failure instant (Murat *et al.*, 2024).

The pressure loading on the PCV drywell is presented in Figure 5-29. Up to the point of the SRV failure (after 270 cycles), the pressure progression was nearly identical to the previous ST-SBO transient. From the stuck-open failure at 5835 seconds until the lower head failure at 22777 seconds, pressure accumulated steadily. A sudden pressure spike was observed upon lower head failure. Once the thermal and pressure conditions were met for the secondary containment failure criteria, the pressure-dependent drywell head flange opening occurred, initiating the transfer of fission products to the environment. At the end of the transient, when cavity ablation reached its radial limit, the final fractions of the fission product inventory distributed across each zone were recorded (Table 5-11).

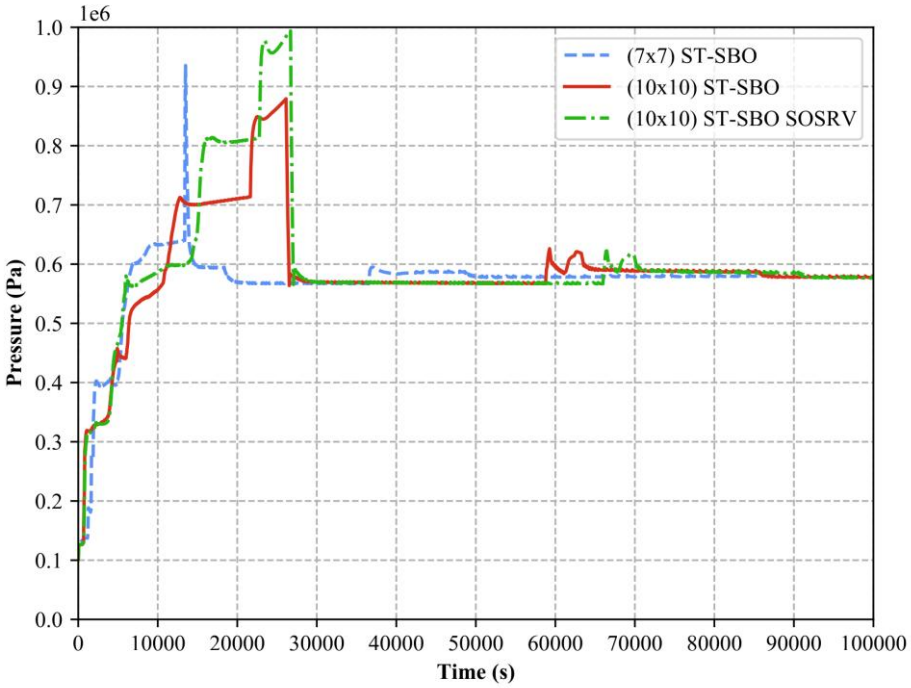


Figure 5-29 Comparison of drywell zone pressure between models which uses 10x10 and 7x7 fuel assemblies and ST-SBO and ST-SBO SOSRV transients (Murat *et al.*, 2024).

Table 5-11 Fission product inventory in the core at the beginning and their fractions in the specified sections at the end of the simulation (Murat *et al.*, 2024).

Elements	Inventory (kg)	Primary	Containment	Environment
Kr	68.60	0.011	0.491	0.356
Xe	1025.79	0.011	0.491	0.356
I	36.66	0.040	0.791	0.020
Sb	2.81	0.033	0.695	0.001
Te	93.41	0.166	0.492	8.53E-4
Ag	7.30	0.182	0.670	0.001
Cs	556.56	0.095	0.772	0.001
Rh	79.54	3.27E-5	3.91E-4	2.83E-7
Mo	644.51	0.134	0.424	4.31E-4
Ba	290.09	0.081	0.322	7.75E-4
Sr	166.72	0.060	0.013	2.8E-5
Y	87.65	4.14E-5	9.77E-6	6.95E-8
Nb	3.80	0.0	0.0	0.0
Ru	479.17	0.024	0.271	2.61E-4
Ce	502.68	0.027	0.096	2.25E-4
La	236.88	0.005	0.017	3.49E-5
Eu	27.98	0.002	0.006	1.26E-5

The ultimate objective of simulating these complex, interconnected severe accident degradation phenomena is to accurately quantify the radiological source term and its exact mass, timing, and isotopic composition released from the containment into the environment. As

demonstrated across the three analyzed scenarios, the evolution of fuel assembly designs, burnup levels, and specific transient occurrences (such as a stuck-open SRV) drastically change the retention capabilities of the reactor vessel and containment structures. The final fission product release fractions calculated at the end of these ASTEC simulations serve as the boundary conditions for assessing off-site consequences. In the following section, these environmental release data sets are directly coupled with the JRODOS decision support system to perform atmospheric dispersion analyses, evaluating the radiological impact on the surrounding public domains.

6 Prediction of the Radiological Impact After Severe Accidents

In order to evaluate the off-site consequences following the fission product release from NPP to environment, radiological dispersion analyses were conducted using the JRODOS decision support system. The following subsections detail the statistical methodology applied and the resulting environmental impact of the three previously defined severe accident scenarios.

6.1 Introduction

A critical challenge in establishing this integrated computational route is bridging the data interface between the severe accident code and the radiological dispersion tool. ASTEC outputs the released source term as time-dependent masses (in kilograms) of specific isotopes. However, the JRODOS decision support system requires input data strictly formatted as radioactive activity (in Becquerels) for individual isotopes over defined time intervals. In order to bridge this computational gap, a dedicated data processing interface was utilized. First, the time-dependent mass release results from ASTEC were extracted. Using the specific initial nuclide inventory established earlier by ORIGEN and CASMO5, isotopic activities calculated based on their specific half-lives and decay chains.

Because the ASTEC simulations predicted a continuous release duration of 20.75 hours for the standard ST-SBO scenarios, the total time scale of the JRODOS model was set to 24 hours to ensure all releases were fully captured. To synchronize the data transfer, a uniform simulation time step of 30 minutes was selected. Consequently, the converted ASTEC isotopic activity data were aggregated into corresponding 30-minute intervals. This rigorous data formatting ensures the accurate transfer of the transient source term into the JRODOS atmospheric dispersion models, successfully completing the continuous computational chain from the degrading reactor core to the environment.

In order to track the path and dispersion of the radioactive plume, real-world historical weather conditions including wind speed, precipitation, and atmospheric stability were provided to the code. A 400 km radius computational mesh grid was constructed around the Peach Bottom Unit-2 plant to adequately cover major surrounding population centers. The mesh distribution and the locations of the targeted cities are illustrated in Figure 6-1. In order to assess the worst case scenario and risk to the public, no emergency countermeasures or evacuation protocols were considered in these simulations.

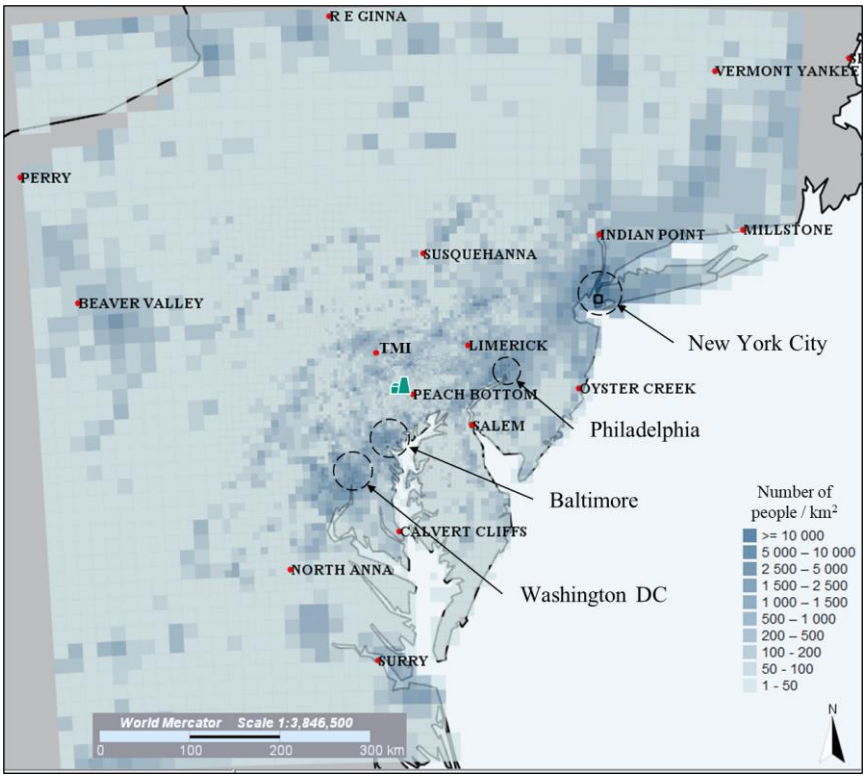


Figure 6-1 Peach Bottom NPP Site location and constructed mesh around with population density (Murat *et al.*, 2023).

Because atmospheric dispersion is highly dependent on fluctuating daily and seasonal weather conditions, performing an analysis for a single, arbitrary day does not yield statistically sufficient information regarding regional risk. Therefore, a robust statistical approach was employed. For each scenario, a random starting time was selected for every single day over a multi-year calendar period. The total effective gamma dose rate for the most populated meshes was recorded daily, allowing for a comprehensive evaluation of both the maximum potential dose and the geographic frequency of plume impacts.

6.2 Development of JRODOS-model to predict the radionuclide dispersion around BWR site

6.2.1 Scenario-1: ST-SBO with historical 7x7 fuel assemblies

For the baseline ST-SBO scenario utilizing historical 7x7 fuel assemblies, the total released radioactivity at the end of the transient was recorded as 1.836E+18 Bq. In order to put in perspective this magnitude, historical severe accidents such as Chernobyl and Fukushima Daiichi released approximately 14.0E+18 Bq (OECD and Nuclear Energy Agency, 2003) and 6.3E+17

Bq (Institute of Nuclear Power Operations (INPO), 2011) respectively. This comparison indicates that the modeled ST-SBO transient represents a massive radiological event. The activity amounts of released radioactive isotopes at the end of this transient are detailed in Table 6-1.

Table 6-1 Amount of radioactive isotopes released to the environment (Murat *et al.*, 2023).

Isotope	Half life	Release (Bq)	Isotope	Half life	Release (Bq)
Kr-85	10.7 y	1.63E+16	Mo-99	2.8 d	3.02E+15
Sb-125	2.8 y	3.50E+13	Rh-105	35.5 h	2.90E+12
Sb-127	3.8 d	3.88E+14	Ba-140	12.8 d	1.30E+15
I-131	8.0 d	1.01E+17	Sr-90	28.6 d	3.57E+12
Te-132	3.2 d	3.94E+15	Sr-91	9.5 h	1.13E+13
I-132	2.3 h	1.98E+16	Y-92	3.7 h	1.51E+12
Xe-133	5.2 d	1.32E+18	Ru-103	39 d	1.11E+14
I-133	20.8 h	1.03E+17	Ru-105	4.4 h	1.73E+12
I-134	0.9 h	3.04E+9	Ru-106	1.0 y	3.21E+13
Cs-134	2.1 y	4.28E+14	La-140	1.7 d	4.42E+14
I-135	6.6 h	1.63E+16	Ce-141	32 d	9.62E+13
Xe-135	9.1 h	2.01E+17	Ce-143	1.4 d	5.48E+13
Cs-137	30.1 y	4.90E+14	Ce-144	284 d	7.25E+13

For this baseline scenario, the statistical dispersion analysis was performed for every day of the calendar year 2021 (365 simulations). The results of this analysis are presented in Figure 6-2. The highest recorded total effective gamma dose rate was 7.2 mSv/h, occurring at the Baltimore City mesh when the simulated release began at 10:33 on February 12, 2021. The individual dispersion analysis and the total effective gamma dose rates for this specific event are shown in Figure 6-3.

To understand the severity of this result, the U.S. Nuclear Regulatory Commission (U.S. Nuclear Regulatory Commission, 1991) states that the yearly total effective dose equivalent limit is 1 mSv for the general public and 5 mSv for radiation workers. The maximum hourly rate recorded in Baltimore significantly exceeds these yearly limits. However, while Baltimore experienced the highest absolute dose rate, it did not experience the highest frequency of impacts. Out of the 365 simulated days, the plume recorded New York City 178 times, Philadelphia 98 times, Baltimore 48 times, and Washington DC 6 times. Because radiological risk is defined as magnitude multiplied by frequency, New York City faces a highly significant risk factor due to the prevailing wind patterns, despite not recording the absolute maximum dose.

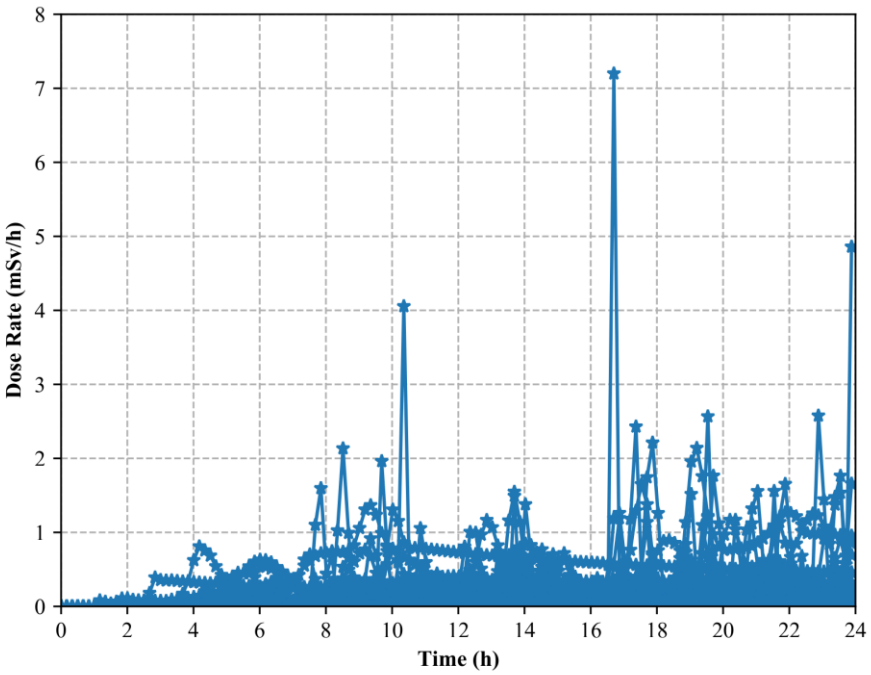


Figure 6-2 Total effective gamma dose rates of each individual one-day simulations of interested meshes for the year 2021 (Murat *et al.*, 2023).

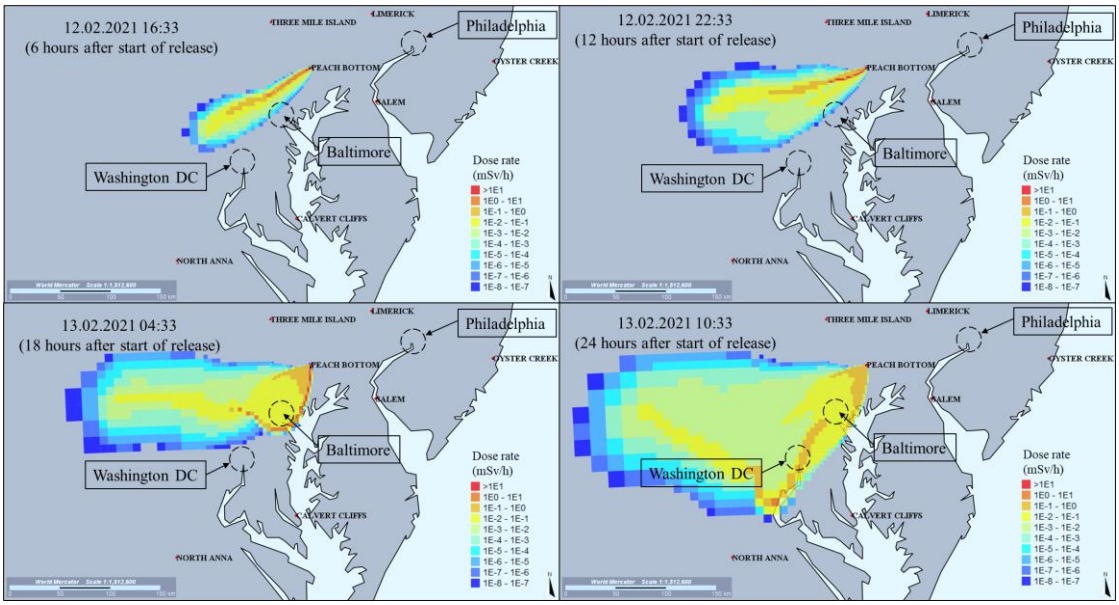


Figure 6-3 Peach Bottom Unit-2 ST-SBO accident resulted total effective gamma dose rate dispersion map when the dispersion started at 10:33 on 12th of February 2021.

6.2.2 Scenario-2: ST-SBO with modern GE14 10x10 fuel assemblies

The ST-SBO simulation utilizing the modernized GE14 10x10 fuel assemblies at a higher discharge burnup resulted in a total released activity of 2.19E+18 Bq (Table 6-2). This total released activity is significantly higher than the baseline historical analysis. The primary factor driving this increase was the higher burnup level of the modern fuel. While modern fuel assembly designs provide significant economic and operational advantages, this result clearly demonstrates that the potential radiological risk factor is proportionally larger in the event of a severe accident.

Table 6-2 Amount of radioactive isotopes released to the environment (Murat *et al.*, 2024).

Isotope	Half life	Release (Bq)	Isotope	Half life	Release (Bq)
Kr-85	10.7 y	1.63E+16	Mo-99	2.8 d	1.35E+15
Sb-125	2.8 y	2.53E+13	Rh-105	35.5 h	1.83E+12
Sb-127	3.8 d	1.54E+14	Ba-140	12.8 d	4.54E+14
I-131	8.0 d	7.98E+16	Sr-90	28.6 d	3.35E+12
Te-132	3.2 d	1.32E+15	Sr-91	9.5 h	3.24E+12
I-132	2.3 h	1.24E+16	Y-92	3.7 h	<<
Xe-133	5.2 d	1.74E+18	Ru-103	39 d	1.15E+14
I-133	20.8 h	7.07E+16	Ru-105	4.4 h	1.14E+12
I-134	0.9 h	5.70E+7	Ru-106	1.0 y	5.45E+13
Cs-134	2.1 y	6.79E+14	La-140	1.7 d	1.92E+14
I-135	6.6 h	9.07E+15	Ce-141	32 d	1.50E+14
Xe-135	9.1 h	2.48E+17	Ce-143	1.4 d	7.83E+13
Cs-137	30.1 y	4.71E+14	Ce-144	284 d	1.26E+14

For this modernized scenario, the statistical approach was expanded to cover a three-year span (from January 1, 2019, to January 1, 2022), resulting in 1,095 individual daily simulations and each individual simulation recordings on selected mesh points given in Figure 6-4. The largest recorded effective gamma dose rate occurred at the Baltimore City mesh, reaching 67.89 mSv/h when the dispersion started at 20:41 on December 13, 2019 (Figure 6-5). Even though the total released activity has increased factor of two, risk factor over the population has jumped up about factor of 10 for the recorded highest dose rate.

The frequency of plume impacts over the 1,095 simulations followed a geographic trend highly consistent with the previous analysis: New York City was impacted 529 times, Philadelphia 316 times, Baltimore 187 times, and Washington DC 45 times. This consistency confirms that while daily weather varies, the long-term prevailing meteorological conditions dictate a stable spatial distribution of risk.

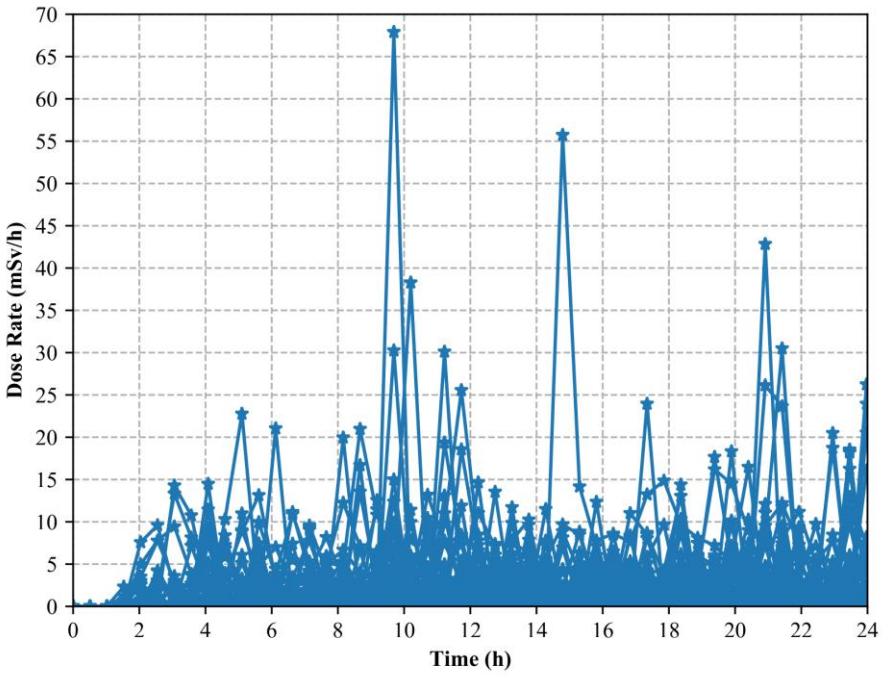


Figure 6-4 ST-SBO transient total effective gamma dose rates of each individual one-day simulations of interested meshes for the years 2019, 2020 and 2021 (Murat *et al.*, 2024).

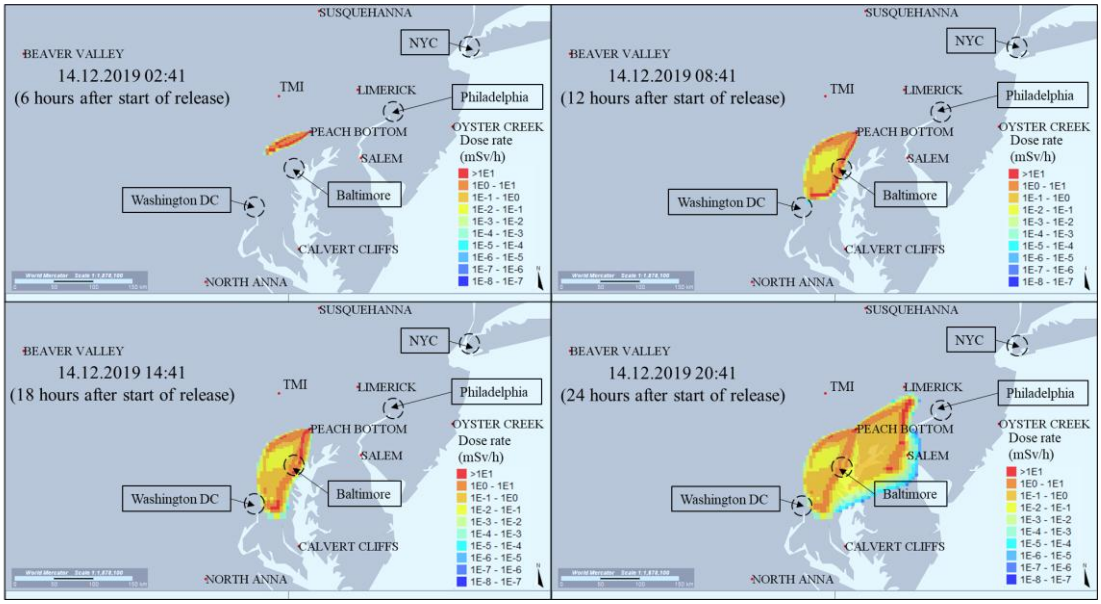


Figure 6-5 Peach Bottom Unit-2 ST-SBO accident resulted total effective gamma dose rate dispersion map when the dispersion started at 20:41 on 13th of December 2019 (Murat *et al.*, 2024).

6.2.3 Scenario-3: ST-SBO with modern GE14 10x10 fuel assemblies with stuck open SRV

The final considered scenario the ST-SBO with modernized 10x10 assemblies and a stuck-open SRV produced the most severe environmental consequences. At the end of the transient, a total released activity of 2.712E+18 Bq was recorded (Table 6-3). This value remains within the order of magnitude of historical severe accidents but represents the maximum source term generated in this study.

Table 6-3 Amount of radioactive isotopes released to the environment (Murat *et al.*, 2024).

Isotope	Half life	Release (Bq)	Isotope	Half life	Release (Bq)
Kr-85	10.7 y	2.19E+16	Mo-99	2.8 d	1.99E+15
Sb-125	2.8 y	5.51E+13	Rh-105	35.5 h	2.56E+13
Sb-127	3.8 d	3.25E+14	Ba-140	12.8 d	4.32E+15
I-131	8.0 d	6.21E+16	Sr-90	28.6 d	1.42E+13
Te-132	3.2 d	3.20E+15	Sr-91	9.5 h	1.00E+13
I-132	2.3 h	8.36E+15	Y-92	3.7 h	<<
Xe-133	5.2 d	2.29E+18	Ru-103	39 d	1.52E+15
I-133	20.8 h	4.82E+16	Ru-105	4.4 h	7.50E+12
I-134	0.9 h	1.38E+6	Ru-106	1.0 y	7.17E+14
Cs-134	2.1 y	1.59E+15	La-140	1.7 d	1.86E+15
I-135	6.6 h	4.48E+15	Ce-141	32 d	1.24E+15
Xe-135	9.1 h	2.46E+17	Ce-143	1.4 d	5.93E+14
Cs-137	30.1 y	1.11E+15	Ce-144	284 d	1.05E+15

Following the same three-year statistical methodology, the results of the 1,095 JRODOS simulations are summarized in Figure 6-6. The maximum recorded effective gamma dose rate reached an extreme 119.46 mSv/h at the Baltimore City mesh, occurring when the dispersion started at 22:55 on October 28, 2020. A visual representation of the plume dispersion for this specific maximum-dose event is provided in Figure 6-7. The general statistical trend indicated that the average received effective gamma dose rate across affected regions was around 20 mSv/h, making this scenario definitively the most hazardous to the public.

The impact frequencies for the considered cities remained consistent with the previous multi-year analysis: New York City was impacted 528 times, Philadelphia 307 times, Baltimore 199 times, and Washington DC 39 times.

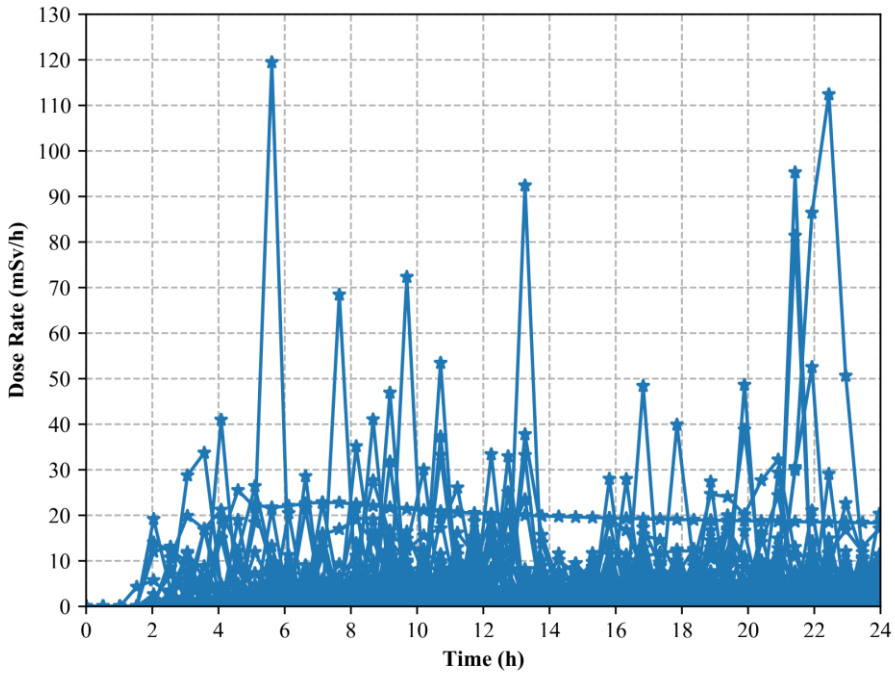


Figure 6-6 ST-SBO SOSRV transient total effective gamma dose rates of each individual one-day simulations of interested meshes for the year 2019, 2020 and 2021 (Murat *et al.*, 2024).

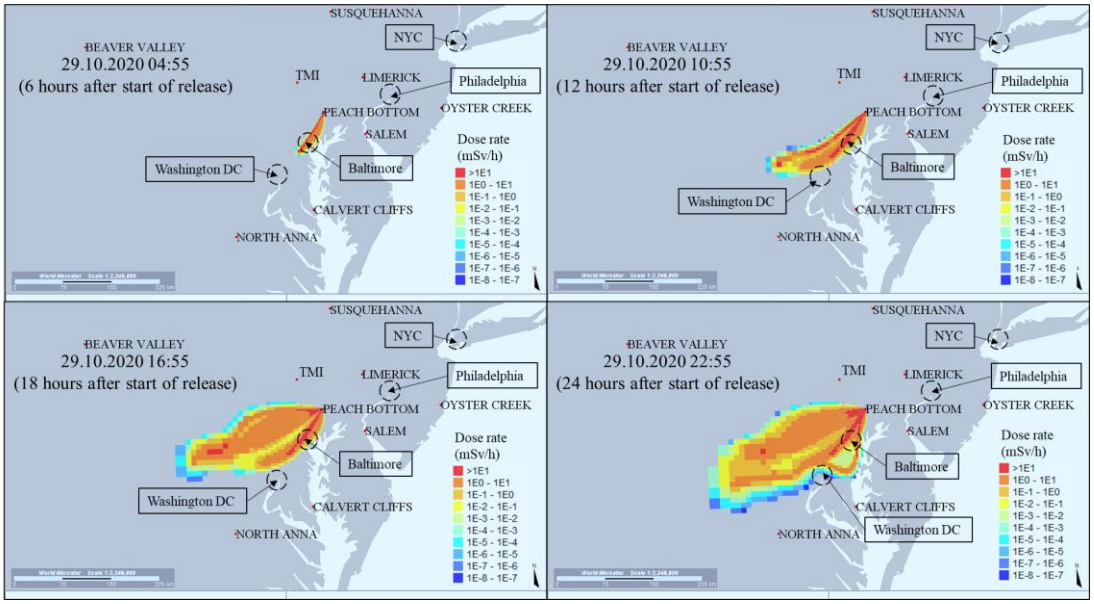


Figure 6-7 Peach Bottom Unit-2 ST-SBO accident resulted total effective gamma dose rate dispersion map when the dispersion started at 22:55 on 28th of October 2020 (Murat *et al.*, 2024).

6.3 Discussion of the main results

The comprehensive statistical analyses performed with JRODOS yielded a critical conclusion that the geographic frequency of the radioactive plume impacting specific cities (such as New York City and Philadelphia) remains relatively constant due to established regional weather patterns, regardless of the accident scenario. However, the magnitude of the resulting effective gamma dose rate varies depending on the reactor's fuel design and the specific thermal-hydraulic progression of the transient. Because overall public risk is a function of both impact frequency and dose magnitude, evaluating isolated maximum dose rates is insufficient for emergency planning. Therefore, to capture overall picture and quantify and visualize this hazard, these statistical dispersion results must be incorporated. The following chapter expands these findings through the construction of comprehensive, regional Risk Maps, providing a definitive assessment of the long-term public consequences of severe accidents at the Peach Bottom Unit-2 NPP.

6.4 Conclusion

This chapter established end-to-end computational route to evaluate the environmental consequences of severe accidents in BWRs. Computation starting from reactor physics, severe accident phenomenology to atmospheric dispersion, this integrated computational route bridged a critical gap in BWR safety analysis, proving that a severe accident assessment is only truly complete when the in-vessel degradation is translated into public health impacts.

The foundation of this computational chain was the calculation of the initial fission product inventory using the ORIGEN and CASMO codes. This step explicitly followed for the technological evolution of reactor cores, comparing historical 7x7 fuel assemblies with modernized, high-burnup GE14 10x10 designs. Subsequently, a highly detailed, integral ASTEC model of the Peach Bottom Unit-2 reactor was developed entirely from scratch. By incorporating realistic geometric nodalization, jet pump hydrodynamics, and the calculated plant-specific nuclide inventories, ASTEC successfully simulated ST-SBO transients. These simulations concluded the precise, time-dependent radiological source terms released from the containment boundaries under described failure modes. By successfully processing this ASTEC output, converting transient mass releases into appropriately formatted isotopic activities (Becquerels), a reliable data interface was established, seamlessly connecting the in-vessel physics to the ex-vessel JRODOS decision support system.

Applying these calculated source terms to the JRODOS decision support system enabled an atmospheric dispersion analysis. The execution of thousands of statistical, multi-year weather simulations revealed a critical safety finding: the modernization of fuel assemblies and their corresponding higher discharge burnups drastically increase the magnitude of the released radioactivity. The ST-SBO scenario involving a stuck-open safety relief valve and the modernized 10x10 core produced the most severe environmental impact, resulting in maximum off-site dose rates that far exceed regulatory public safety limits.

However, identifying maximum dose rates is insufficient for comprehensive emergency preparedness. The JRODOS statistical results demonstrated that while maximum exposure doses fluctuate based on the specific accident progression, the spatial frequency of radioactive plume impacts is strictly governed by established regional meteorological patterns. Because public risk is a function of both the radiological magnitude of the release and the geographic probability of plume exposure, a more detailed evaluation of these hazards is required. Therefore, the following chapter explains these extensive dispersion datasets to construct high-resolution spatial Risk Maps.

7 Development of Risk Map of Radiological Dispersion

7.1 Introduction

The analyses presented in the previous chapter demonstrated that while a deterministic severe accident simulation can accurately predict a radiological source term, relying on a single weather sequence or a limited statistical sample provides an incomplete picture of public risk. Traditional dispersion analyses often select arbitrary or worst-case meteorological starting points, which may not accurately represent the long-term, prevailing weather conditions of a specific geographic region.

To overcome the limitations of traditional, deterministic JRODOS applications, this chapter introduces a novel methodological approach: the development of probabilistic, high-resolution Risk Maps. By expanding the computational database to account for a massive array of meteorological permutations, this methodology transforms raw source term data into a comprehensive risk assessment tool. This approach not only fulfills the final goal of the proposed integrated computational route but also provides emergency preparedness teams with a significantly more robust, statistically reliable instrument for mitigating the consequences of severe radiological releases.

7.2 Development of realistic risk maps for selected region using radiological dispersion

In order to achieve a truly comprehensive risk profile, the computational database must be expanded to account for all possible release scenarios permitted by the dispersion code. JRODOS can conduct dispersion analyses with a time resolution of one minute, meaning there are 1440 potential meteorological starting points for any given day. Analyzing the dispersion at this maximum resolution would yield an exact average dose rate over the geographic grid. However, repeating this process for an entire multi-year period to capture seasonal variations demands an enormous amount of CPU power and computational time.

To resolve this computational bottleneck, a statistical sampling methodology based on the Central Limit Theorem was employed. Rather than processing the entire, exhaustive dataset, randomly selected sample groups were generated to estimate the population mean and variance of the dose rates. According to established statistical principles, the distribution of these sample means converges to a normal distribution when the sample group size is sufficiently large (typically $n \geq 30$), allowing the distribution mean to accurately approximate the true population

mean (Ewens and Brumberg, 2023). This robust approach allows for the derivation of highly accurate regional dose rate averages without the need for computationally unfeasible, minute-by-minute simulations.

In order to create the database, the year 2021 was selected. Each season in the year was separately taken into account since the average weather conditions are close to each other on seasonal days. The transient ST-SBO of Peach Bottom Unit-2 dispersion results were introduced to JRODOS, and 500 sample groups, each consisting of 30 simulations, were constructed. Consequently, each season consisted of 15,000 simulations, and yearly coverage of 2021 was achieved with a total of 60,000 simulations.

Group average total gamma dose rate information in each grid mesh was collected, and the distribution of the group averages was created. One example of the distribution of average sampling groups in a mesh can be seen in Figure 7-1. As can be seen in the figure, the average distribution of the total gamma dose rate for a selected mesh converges to a normal distribution. This convergence means that the average of the distribution also provides the population average, which includes the results of all the possible scenarios on the mesh. Even though the distribution does not perfectly fit a normal distribution, the assumption was made that the distributions over the meshes on the grid all perfectly fit the normal distribution in order to drive the next step of the approach.

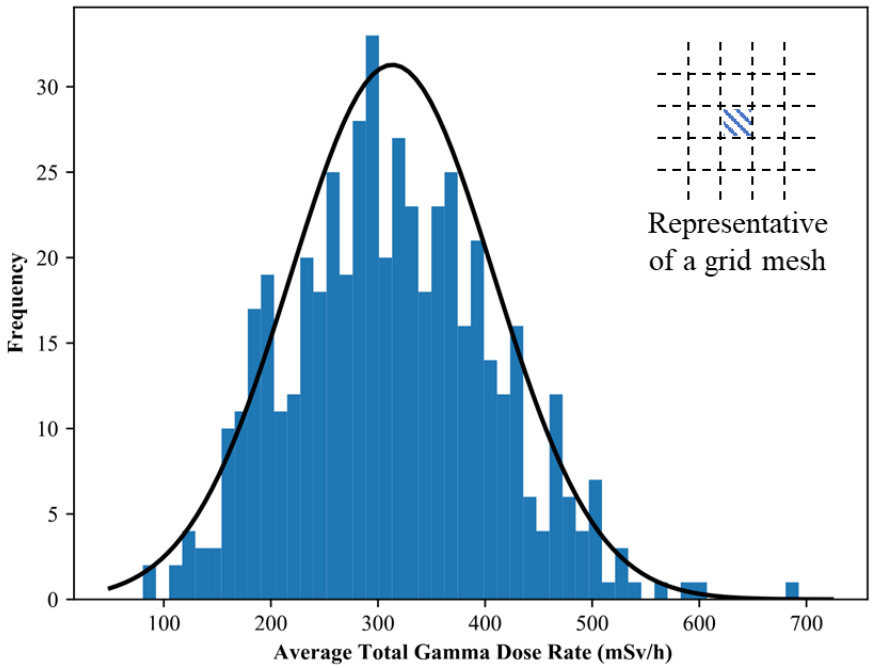


Figure 7-1 Distribution of average of sampling groups for a representative mesh.

7.3 Discussion of the main results

The resulting probabilistic dispersion maps, categorized by season, synthesize both the intensity of the total effective gamma dose rate and the geographic frequency of plume impact into a single, comprehensive visualization. As demonstrated in the generated Risk Maps (Figure 7-3, Figure 7-4, Figure 7-5 and Figure 7-6). the largest spatial dispersion of the dose rate was recorded during the winter season, driven by prevailing wind directions toward the south and southeast. Conversely, the smallest geographic extension over the considered grid was observed during the summer season, where lower average wind speeds restricted the dispersion radius.

The construction of these Risk Maps represents a significant advancement over traditional, single-scenario dispersion methodologies. By integrating the massive statistical database generated from the ASTEC source term, these maps provide emergency and preparedness teams with actionable, probabilistic intelligence. Rather than relying on isolated deterministic calculations that may skew risk perceptions, decision-makers can utilize these Risk Maps to anticipate the most statistically probable contamination zones and dose magnitudes based on seasonal weather patterns. Ultimately, this methodology fulfills the final objective of the integrated computational route, translating complex in-vessel severe accident physics into a robust, practical tool for public safety and emergency planning.

In order to clearly demonstrate the value of this advanced methodology, Figure 7-2 provides a direct comparison between a standard, single event dispersion simulation and the developed probabilistic Risk Map. A standard simulation relies on an arbitrary selection of release time and localized weather conditions, which yields a narrow, highly specific plume trajectory that may not represent the true outcome. In contrast, the constructed Risk Map includes a massive dataset to provide a comprehensive, 2-D spatial probability distribution over the entire region. By integrating both the intensity of the dose and the geographic frequency of the plume impacts, the Risk Map delivers significantly more robust and extensive information for emergency preparedness than any single deterministic simulation could provide.



Figure 7-2 Comparison of single radiological dispersion analysis (left) and created risk map (right).

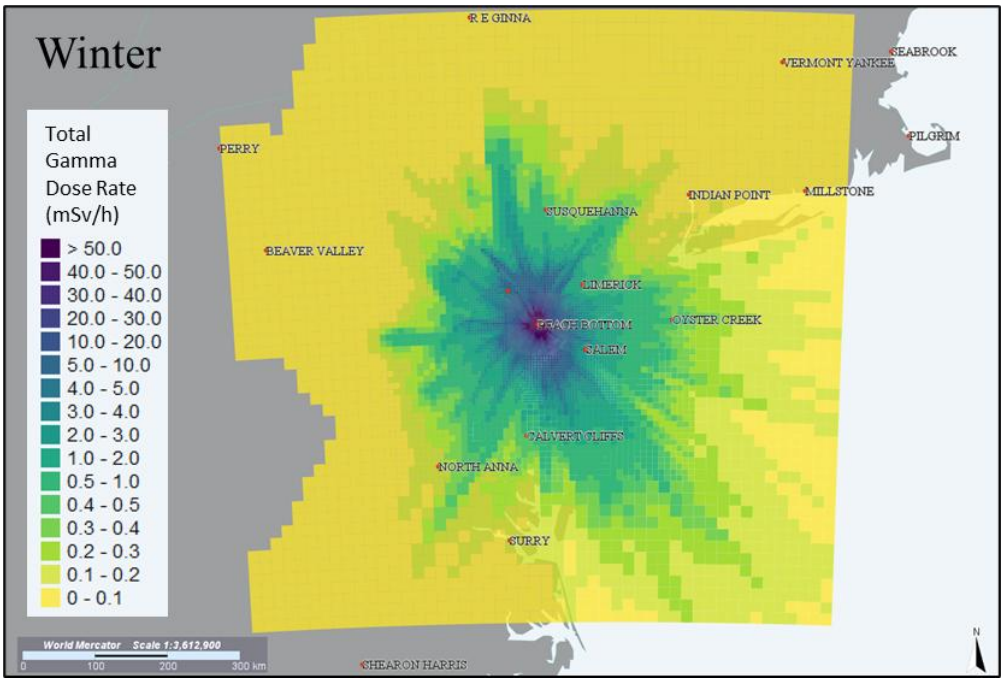


Figure 7-3 Probabilistic dispersion map of winter season of 2021 in result of station blackout transient in Peach Bottom Unit-2 Plant.

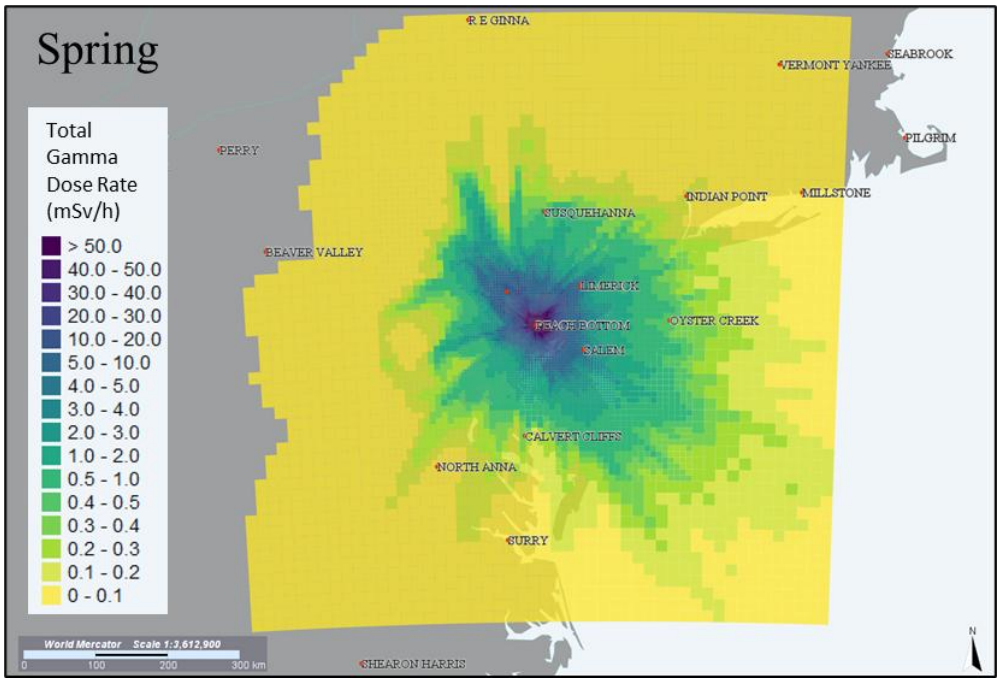


Figure 7-4 Probabilistic dispersion map of spring season of 2021 in result of station blackout transient in Peach Bottom Unit-2 Plant.

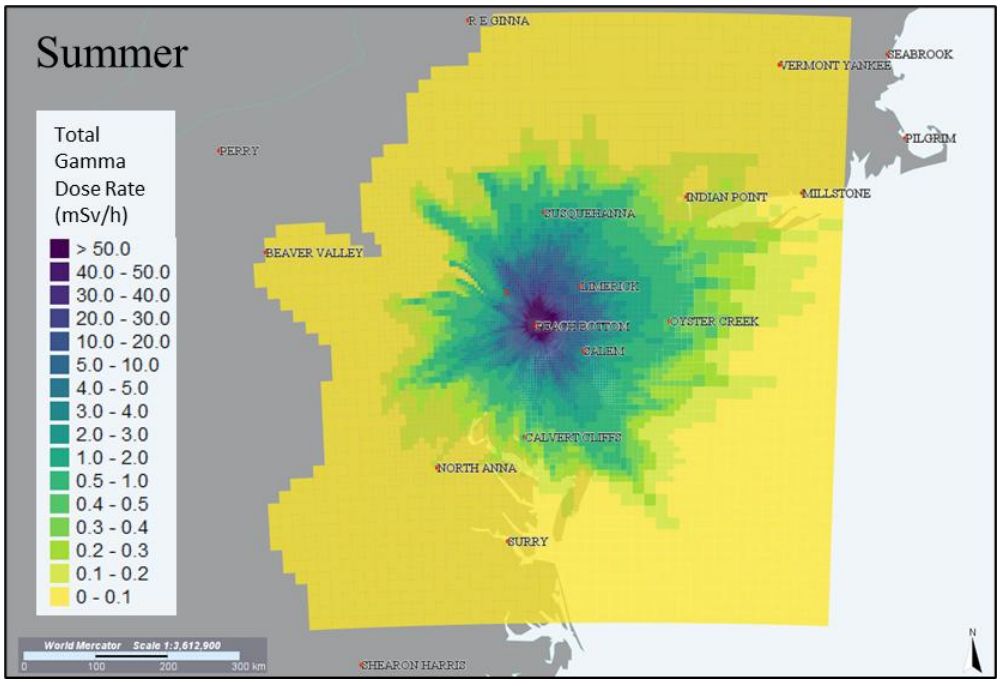


Figure 7-5 Probabilistic dispersion map of summer season of 2021 in result of station blackout transient in Peach Bottom Unit-2 Plant.

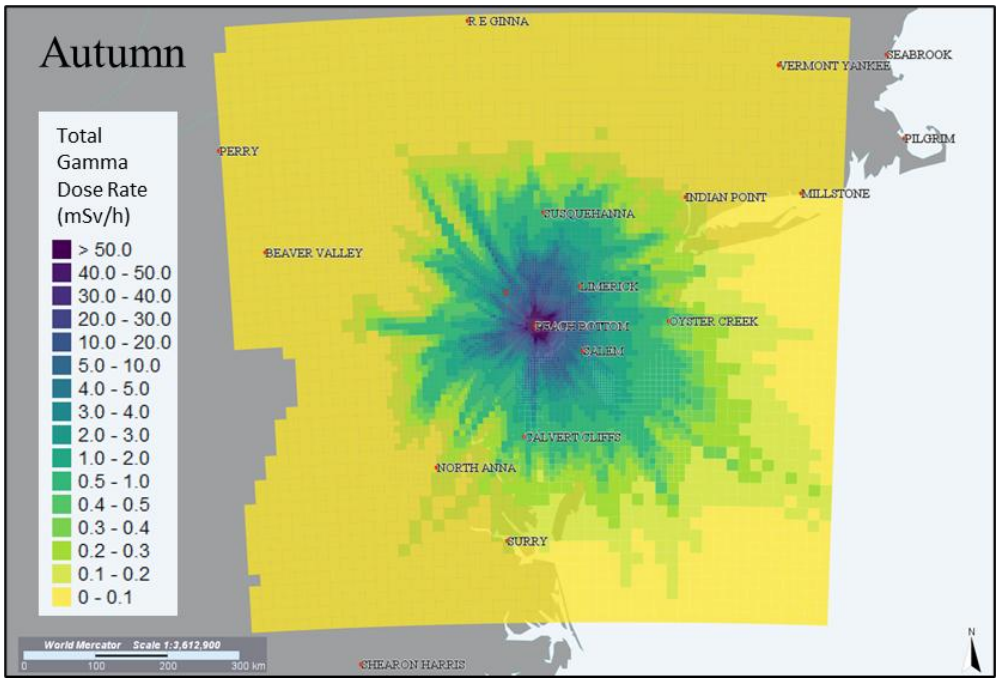


Figure 7-6 Probabilistic dispersion map of autumn season of 2021 in result of station blackout transient in Peach Bottom Unit-2 Plant.

While the developed risk maps provide critical insights into the radiological dispersion and public safety, it is important to note that they are based on the total effective gamma dose rate. Consequently, this metric alone does not present the complete picture of radioactive dispersion and public exposure. A fully comprehensive assessment must also account for long-term health effects, inhalation doses, ground shine and ingestion pathways, such as plant-based transfer mechanisms through the local agriculture. Furthermore, the implementation of emergency precautions and protective countermeasures would significantly alter the exposure scenarios. Therefore, while the current methodology yields highly valuable information for general plume tracking and initial emergency planning, these detailed exposure pathways and mitigation strategies must be incorporated in future studies to provide a comprehensive radiological risk assessment.

8 Main Conclusions

The primary objective of this doctoral thesis was to address the identified scientific gaps by developing a complete, integrated computational route for estimating the radiological impact of severe accidents in BWRs. By successfully linking tools for nuclide inventory prediction (ORIGEN/CASMO5), severe accident progression (ASTEC), and radiological dispersion (JRODOS), this work established a first-of-its-kind, end-to-end computational chain. Furthermore, to answer the research question regarding data exchange, appropriate data processing interfaces were successfully established to convert the time-dependent radiological source terms from ASTEC into the formats required by JRODOS.

As a foundational step to answer the research question regarding model reliability, the ASTEC code was validated with the QUENCH-20 experiment. This validation showed that the code predicts the global parameter of hydrogen generation in an acceptable manner. While the integral code carries some uncertainties in predicting local flow blockages and the precise timing of local degradation phenomena due to the assumption of isotropic flow, validating the fundamental oxidation physics justified stepping up to larger-scale analyses for BWR-type plants.

Within this computational route, a comprehensive ASTEC model for the BWR4 Mark-1 type reactor, Peach Bottom Unit-2, was developed entirely from scratch. The most anticipated scenario, ST-SBO, was applied to this newly developed model. Starting from the calculation of the fission product inventory in the fuel, the severe accident analysis was conducted with ASTEC up to the point of environmental release. Following this, the radiological dispersion analysis and risk assessment were completed using the JRODOS code.

The same procedure was followed for the updated model, which included the modern GE14 10x10 fuel assemblies with higher burnup and fission product inventories, as well as recirculation line improvements for a better estimation of the flow in the downcomer. The degree of the environmental release in these simulations was one order of magnitude smaller than the Fukushima Daiichi accident. Comparing the transient with Fukushima helps to contextualize the scale of the radiological release, keeping in mind that the multiple power plant failures at Fukushima Daiichi and the specific burnup levels of those fuels at the instant of the accident differ from the analyzed scenarios.

The timing of the lower head failure and the total amount of corium released from the lower plenum were scattered heavily across each case. Not only the burnup level, but also the recirculation line updates and the different considered transients affected the end point of the in-vessel accident progression. The ASTEC model's lower head failure mode considers only the loss

of integrity of the lower head wall meshes depending on the described thermal criteria. There is significant uncertainty in modeling the lower plenum of the reactor pressure vessel. While the modeling accounts for the presence of support structures, the exact thermal mass in the lower plenum plays an important role; an extensive amount of structural material in the actual plant may delay the progression of lower head failure.

It is also necessary to acknowledge the uncertainties introduced by the definition of the initial neutronic boundary conditions. The neutronic calculations used to describe the decay heat power and the fission product inventory are based on the burnup history of the core. Since the specific operating conditions assumed for the referenced plant are adapted to produce the decay and fission product inventory, the homogenized irradiation history introduces an uncertainty factor in the specific isotopic composition of the fuel. Because residual decay heat is the primary driver of the timeline for coolant boiling, core degradation, relocation of molten material, and further failure of barriers, the computed decay heat curve strongly influences the accident progression in the in-vessel and ex-vessel domains.

In order to answer the research question regarding smart alternative methods for radiological risk estimation, a novel statistical approach was developed. In order to increase the span of the radiological dispersion study, a comprehensive analysis, including the total effective gamma dose rate and a statistical assessment of geographical meshes corresponding to highly populated cities, spanned three years of weather data. While the highest recorded dose and average received doses were greater for the ST-SBO with a stuck-open safety relief valve scenario, vessel failure occurred approximately 1000 seconds later. Due to the random selection of release times in JRODOS, different results and plume pathways can occur on the same day. By increasing the number of analyses for the considered meshes and creating a pool of samples with different release times for each day, this statistical approach successfully provided a distribution of received dose rates, supporting the creation of a realistic Risk Map.

Because the assumption of a normal distribution was used to create the Risk Map, uncertainties are naturally introduced into the calculation. However, even though a perfect statistical fit is not always possible due to the chaotic nature of meteorological events, this approach provided a massive performance boost. It successfully expanded the radiological dispersion database to evaluate potential long-term outcomes over the region. This probability information directly supports decision makers in determining appropriate, timely countermeasures during radiological releases.

Overall, the successful execution of this full computational platform has provided a complete picture of reactor safety. Furthermore, to answer the final research question, while this

methodology was demonstrated using a specific BWR design, the established interfaces and the computational route are highly flexible and can be applied to any reactor design. Not only the severe accident progression analysis, but also the extension of the study with precise radionuclide inventories and the finalization with probabilistic Risk Maps, delivers a vital, generalizable toolset for strengthening public and environmental safety.

9 Outlook

The development of the integrated computational route in this thesis establishes a robust foundation for severe accident risk assessment; however, its methodology opens several critical potential applications for future research. The extension of this end-to-end platform is foreseen for new nuclear power plant designs, particularly Small Modular Reactors (SMRs). Because these next generation plants are designed to be built on smaller scales and distributed across various locations, such as providing power in remote areas or ensuring industrial heat production near highly populated zones, severe accident investigations using this enhanced probabilistic Risk Map approach will be absolutely necessary to guarantee public and environmental safety.

Furthermore, the evolution of BWR fuel assemblies has continuously transitioned towards higher burn-up levels, extended operation periods, and longer lifetimes. The design and shape of fuel assemblies are changing to increase neutron and thermal efficiencies. The configuration of new 11x11 BWR fuel assemblies, such as the Framatome Atrium 11 and the Westinghouse Triton 11, represents the next generation of modern fuel for these plants. They introduce significant geometric and material changes, including variations in rod diameter, heat transfer area, and water rod placements within the assembly. Future reactor safety analyses and severe accident progression investigations must adapt to include these new assembly designs.

In addition, reducing uncertainties by applying highly specific operational parameters to produce a fuel inventory closer to real time plant values should be considered in future work. This would eliminate potential overestimations of the decay heat and fission product inventory, further improving the accuracy of safety limits and margins. Future development of the ASTEC code itself could also focus on enhancing the azimuthal discretization capabilities for core degradation and material placement. The current concentric ring approximation limits the ability to capture strong local thermal gradients caused by non-symmetric features. While large conventional power plants may not suffer significantly from this limitation due to their homogeneous cores, the compact and complicated geometries of SMRs will require it. Implementing a more flexible, refined azimuthal meshing approach would enable a much more accurate prediction of localized failures and blockages.

The ASTEC code could also be extended to include localized penetration failure models for the BWR lower head. The Fukushima Daiichi accident indicated that accident progression and vessel failure are heavily driven by thermal attack and the ejection of molten material through failed control rod guide tubes (OECD and Nuclear Energy Agency, 2021). Because this specific model is not currently available in the code, global thermal failure modes were used for the lower

plenum wall of the plant. Integrating penetration tube thermal failure and localized ejection modes would enable a more accurate prediction of the timing and location of debris release during the transition from the in-vessel to the ex-vessel domain.

Finally, to accelerate the generation of the probabilistic Risk Maps, the implementation of artificial intelligence surrogate models and machine learning will play an important role. Although the statistical methodology developed in this thesis produces a critical database for emergency preparedness, conducting tens of thousands of dispersion analyses still requires significant computational time. Trained AI surrogate models could drastically accelerate this process, expanding the dispersion database to include millions of simulations over broader geographic regions and more complex weather conditions. Ultimately, integrating AI into this established computational chain will allow emergency management teams to generate dynamic, real-time Risk Maps, ensuring immediate and highly optimized responses to any severe radiological event.

Bibliography

Barrachin, M., De Luze, O., Haste, T. and Repetto, G. (2013) "Late phase fuel degradation in the Phébus FP tests," *Annals of Nuclear Energy*, 61, pp. 36–53. Available at: https://doi.org/10.1016/j.anucene.2013.03.041.

Bixler, N., Gauntt, R., Jones, J. and Leonard, M. (2013) *State-of-the-Art Reactor Consequence Analyses Project Volume 1: Peach Bottom Integrated Analysis*. NUREG/CR-7110 Vol. 1, Rev. 1. Albuquerque, New Mexico 87185: Sandia National Laboratories. Available at: https://www.nrc.gov/docs/ML1315/ML13150A053.pdf.

Carbajo, J.J. (1993) *Severe Accident Source Term Characteristics for Selected Peach Bottom Sequences Predicted by the MELCOR Code*. NUREG/CR-5942, ORNL/TM-12229. Oak Ridge, TN37831-6285: Oak Ridge National Laboratories. Available at: https://doi.org/10.2172/10182846.

Carbajo, J.J. (1994) "MELCOR sensitivity studies for a low-pressure, short-term station blackout at the Peach Bottom plant," *Nuclear Engineering and Design*, 152(1–3), pp. 287–317. Available at: https://doi.org/10.1016/0029-5493(94)90093-0.

Carénini, L., Fichot, F. and Seignour, N. (2018) "Modelling issues related to molten pool behaviour in case of In-Vessel Retention strategy," *Annals of Nuclear Energy*, 118, pp. 363–374. Available at: https://doi.org/10.1016/j.anucene.2018.04.032.

Chatelard, P., Belon, S., Bosland, L., Carénini, L., Coindreau, O., Cousin, F., Marchetto, C., Nowack, H., Piar, L. and Chailan, L. (2016) "Main modelling features of the ASTEC V2.1 major version," *Annals of Nuclear Energy*, 93, pp. 83–93. Available at: https://doi.org/10.1016/j.anucene.2015.12.026.

Chatelard, P. and Laborde, L. (2023) "ASTEC V2.2 code validation: Illustrative results and main outcomes," *Nuclear Engineering and Design*, 413, p. 112547. Available at: https://doi.org/10.1016/j.nucengdes.2023.112547.

ERIN Engineering and Research, Inc. (2010) *MAAP4 Applications Guidance: Desktop Reference for Using MAAP4 Software, Revision 2*. 2010. 1020236. Palo Alto, CA: ELECTRIC POWER RESEARCH INSTITUTE (EPRI). Available at: https://www.epri.com/research/products/000000000001020236.

Ewens, W.J. and Brumberg, K. (2023) *Introductory Statistics for Data Analysis*. Cham: Springer Nature Switzerland. Available at: https://doi.org/10.1007/978-3-031-28189-1.

Exelon Generation Company (2018) *SUBSEQUENT LICENSE RENEWAL APPLICATION Peach Bottom Atomic Power Station Units 2 and 3*. Facility Operating License Nos. DPR-44 and DPR-56. Available at: https://www.nrc.gov/docs/ML1819/ML18193A773.pdf.

Gauld, I. and Mertyurek, U. (2018) *Margins for Uncertainty in the Predicted Spent Fuel Isotopic Inventories for BWR Burnup Credit*. NUREG/CR-7251 ORNL/TM-2018/782. Bethel Valley Road Oak Ridge, TN 37831: U.S. Nuclear Regulatory Commission Office of Nuclear Regulatory Research. Available at: https://www.nrc.gov/docs/ML1835/ML18352A520.pdf.

Gauntt, R.O., Gasser, R.D. and Ott, L.J. (1989) *The DF-4 fuel damage experiment in ACRR (Annual Core Research Reactor) with a BWR (Boiling Water Reactor) control blade and channel box*. NUREG/CR-4671. Albuquerque, NM 87185: Sandia National Laboratories. Available at: https://doi.org/10.2172/5101359.

Gauntt, R.O. and Humphries, L.L. (1997) *Final results of the XR2-1 BWR metallic melt relocation experiment*. NUREG/CR-6527. Albuquerque, NM 87185: Sandia National Laboratories. Available at: https://doi.org/10.2172/531083.

Hodge, S.A. and Ott (1997) "Interpretation of the XR2-1 experiment and characteristics of the BWR lower plenum debris bed." *American Nuclear Society (ANS) international meeting on advanced reactors safety*, Orlando, FL (United States): American Nuclear Society, Inc., pp. 905–912.

Hofmann, P. (1999) "Current knowledge on core degradation phenomena, a review," *Journal of Nuclear Materials*, 270(1–2), pp. 194–211. Available at: https://doi.org/10.1016/S0022-3115(98)00899-X.

Hofmann, P., Stuckert, J., Miassoedov, A., Veshchunov, M.S., Berdyshev, A.V. and Boldyrev, A.V. (1999) *ZrO2 Dissolution by Molten Zircaloy and Cladding Oxide Shell Failure. New Experimental Results and Modelling*. FZKA 6383. Karlsruhe: Forschungszentrum Karlsruhe GmbH. Available at: https://doi.org/10.5445/IR/270046616.

Hu, J., Peterson, J.L., Gauld, I.C. and Bowman, S.M. (2016) *U.S. Commercial Spent Nuclear Fuel Assembly Characteristics - 1968-2013*. ORNL/TM--2015/619, 1330516, p. ORNL/TM--2015/619, 1330516. Available at: https://doi.org/10.2172/1330516.

Humphries, L.L., Beeny, B.A., Gelbard, F., Louie, D.L. and Phillips, J. (2017) *MELCOR Computer Code Manuals Vol. 1: Primer and Users' Guide Version 2.2.9541*. Albuquerque, NM 87185-0748: Sandia National Laboratories. Available at: https://www.nrc.gov/docs/ML1704/ML17040A429.pdf.

Hykes, J.M., Ferrer, R.M. and Rhodes, J.D. (2022) *CASMO5 A FUEL ASSEMBLY BURNUP PROGRAM User's Manual*. SSP-07/431 Rev 21. Idaho Falls, ID 83402-3345, USA: Studsvik Scandpower, Inc.

IAEA (1999) *Basic safety principles for nuclear power plants: 75-INSAG-3 Rev. 1; a report*. Vienna: International Atomic Energy Agency. ISBN 978-92-0-102699-6 (Safety series INSAG / International Atomic Energy Agency, Vienna).

IAEA (2023) *Nuclear Power Reactors in the World*. Vienna: INTERNATIONAL ATOMIC ENERGY AGENCY. ISBN 978-92-0-137123-2.

Ievdin, I., Trybushny, D., Zheleznyak, M. and Raskob, W. (2010) "RODOS re-engineering: aims and implementation details," *Radioprotection*, 45(5), pp. S181–S189. Available at: https://doi.org/10.1051/radiopro/2010024.

Institute of Nuclear Power Operations (INPO) (2011) *Special Report on the Nuclear Accident at the Fukushima Daiichi Nuclear Power Station*. INPO 11-005. Available at: https://www.nrc.gov/docs/ML1134/ML11347A454.pdf.

Lahey, R.T. and Moody, F.J. (1993) *The thermal-hydraulics of a boiling water nuclear reactor*. 2nd ed. La Grange Park, Ill: American Nuclear Society. ISBN 978-0-89448-037-9.

Lamarsh, J.R. and Baratta, A.J. (2001) *Introduction to nuclear engineering*. 3rd ed. Upper Saddle River, N.J: Prentice Hall. ISBN 978-0-201-82498-8 (Addison-Wesley series in nuclear science and engineering).

Larsen, N. (1978) *Core design and operating data for Cycles 1 and 2 of Peach Bottom 2*. EPRI-NP-563, 6561294, p. EPRI-NP-563, 6561294. Available at: https://doi.org/10.2172/6561294.

Leonard, M.T., Gauntt, R.O. and Powers, D.A. (2007) *Accident Source Terms for Boiling Water Reactors with High Burnup Cores Calculated Using MELCOR 1.8.5*. SAND2007-7697. Albuquerque, New Mexico 87185 and Livermore, California 94550: Sandia National Laboratories. Available at: https://www.osti.gov/servlets/purl/1004364.

Litz, L.M. and Mercuri, R.A. (1963) "Oxidation of Boron Carbide by Air, Water, and Air-Water Mixtures at Elevated Temperatures," *Journal of The Electrochemical Society*, 110(8), p. 921. Available at: https://doi.org/10.1149/1.2425901.

Marshall, W., Ade, B.J., Bowman, S. and Martinez-Gonzalez, J.S. (2016) *Axial Moderator Density Distributions, Control Blade Usage, and Axial Burnup Distributions for Extended BWR Burnup Credit*. NUREG/CR-7224 ORNL/TM-2015/544. Oak Ridge, TN 37831-6170: Oak Ridge national Laboratory.

Martinez, J.S., Ade, B.J., Bowman, S.M., Gauld, I.C., Ilas, G. and Marshall, W.J. (2015) "IMPACT OF MODELING CHOICES ON INVENTORY AND IN-CASK CRITICALITY CALCULATIONS FOR FORSMARK 3 BWR SPENT FUEL." *Conference: ICNC 2015 International Cooperation in Nuclear Criticality Safety*, Charlotte, NC (United States): Oak Ridge National Laboratories. Available at: https://doi.org/OSTI ID:1223658.

Murat, O., Sanchez-Espinoza, V., Gabrielli, F., Stieglitz, R. and Queral, C. (2023) "Analysis of the short Term-Station Blackout accident at the Peach Bottom Unit-2 reactor with ASTEC including the estimation of the radiological impact with JRODOS," *Nuclear Engineering and Design*, 406, p. 112227. Available at: https://doi.org/10.1016/j.nucengdes.2023.112227.

Murat, O., Sanchez-Espinoza, V., Gabrielli, F., Wang, S., Stieglitz, R. and Queral, C. (2024) "Improved Analysis of the Short-Term Station Blackout Accidents of the Peach Bottom Unit-2 Reactor with ASTEC Including Radiological Impact and Statistical Analysis with JRODOS," *Nuclear Engineering and Design*, 420, p. 113012. Available at: https://doi.org/10.1016/j.nucengdes.2024.113012.

Murat, O., Sanchez-Espinoza, V., Wang, S. and Stuckert, J. (2020) "Preliminary validation of ASTEC V2.2.b with the QUENCH-20 BWR bundle experiment," *Nuclear Engineering and Design*, 370, p. 110931. Available at: https://doi.org/10.1016/j.nucengdes.2020.110931.

Nagase, F., Uetsuka, H. and Otomo, T. (1997) "Chemical interactions between B4C and stainless steel at high temperatures," *Journal of Nuclear Materials*, 245(1), pp. 52–59. Available at: https://doi.org/10.1016/S0022-3115(96)00747-7.

Narabayashi, T., Yamazaki, Y., Kobayashi, H. and Shakouchi, T. (2006) "Flow Analysis for Single and Multi-Nozzle Jet Pump," *JSME International Journal Series B*, 49(4), pp. 933–940. Available at: https://doi.org/10.1299/jsmeb.49.933.

NEA (2003) *OECD Lower Head Failure Project Final Report*. OECD Publishing. Paris.

OECD and Nuclear Energy Agency (2003) *Chernobyl: Assessment of Radiological and Health Impacts: 2002 Update of Chernobyl: Ten Years On*. OECD. Available at: https://doi.org/10.1787/9789264184879-en.

OECD and Nuclear Energy Agency (2021) *Benchmark Study of the Accident at the Fukushima Daiichi Nuclear Power Plant*. OECD (Nuclear Safety). Available at: https://doi.org/10.1787/a7af03aa-en.

Radaideh, M.I., Price, D. and Kozlowski, T. (2018) "Criticality and uncertainty assessment of assembly misloading in BWR transportation cask," *Annals of Nuclear Energy*, 113, pp. 1–14. Available at: https://doi.org/10.1016/j.anucene.2017.11.006.

Rochman, D., Vasiliev, A., Ferroukhi, H., Muñoz, A., Antolin, M.V., Torres, M.B., Sanchez, C.C., Simeonov, T. and Shama, A. (2022) "Analysis of ENRESA BWR samples: nuclide inventory and decay heat," *EPJ Nuclear Sciences & Technologies*, 8, p. 9. Available at: https://doi.org/10.1051/epjn/2022007.

Sato, T., Haryu, K. and Endo, T. (1988) "Oxidation of Nonoxide Ceramics by Water Vapor at High Temperatures," *Journal of the Society of Materials Science*, 37, pp. 77–82. Available at: https://doi.org/10.2472/jsms.37.77.

Schanz, G., Adroguer, B. and Volchek, A. (2004) "Advanced treatment of zircaloy cladding high-temperature oxidation in severe accident code calculations," *Nuclear Engineering and Design*, 232(1), pp. 75–84. Available at: https://doi.org/10.1016/j.nucengdes.2004.02.013.

Sehgal, B.R. (ed.) (2012) *Nuclear safety in light water reactors: severe accident phenomenology*. Amsterdam ; Boston: Elsevier/Academic Press. ISBN 978-0-12-388446-6. Available at: https://doi.org/10.1016/C2010-0-67817-5.

Sehgal, B.R., Theerthan, A., Giri, A., Karbojian, A., Willschütz, H.G., Kymäläinen, O., Vandroux, S., Bonnet, J.M., Seiler, J.M., Ikkonen, K., Sairanen, R., Bhandari, S., Bürger, M., Buck, M., Widmann, W., Dienstbier, J., Techy, Z., Kostka, P., Taubner, R., Theofanous, T. and Dinh, T.N. (2003) "Assessment of reactor vessel integrity (ARVI)," *Nuclear Engineering and Design*, 221, pp. 23–53. Available at: https://doi.org/10.1016/S0029-5493(02)00343-6.

Steinbrück, M. (2005) "Oxidation of boron carbide at high temperatures," *Journal of Nuclear Materials*, 336(2–3), pp. 185–193. Available at: https://doi.org/10.1016/j.jnucmat.2004.09.022.

Steinbrück, M. [Hrsg (2019) "25th International QUENCH Workshop : 22-24 October 2019, Karlsruhe Institute of Technology, Karlsruhe, Germany." Karlsruhe. Available at: https://doi.org/10.5445/IR/1000100298.

Stuckert, J., Bechta, S., Hollands, T., Isaksson, P. and Steinbrueck, M. (2023) "Experimental and modelling results of the QUENCH-20 experiment with BWR test bundle," *Nuclear Engineering and Design*, 410, p. 112391. Available at: https://doi.org/10.1016/j.nucengdes.2023.112391.

Stuckert, J., Boldyrev, A.V., Miassoedov, A., Palagin, A.V., Schanz, G., Sepold, L., Shestak, V.E., Stegmaier, U., Steinbock, L., Steinbrück, M., Steiner, H. and Veshchunov, M.S.

(2005) *Experimental and Computational Results of the QUENCH-08 Experiment (Reference to QUENCH-07)*. FZKA 6970. Karlsruhe: Forschungszentrum Karlsruhe GmbH. Available at: https://doi.org/10.5445/IR/270062382.

Tien, C.L., Sanchez, R.A., Mandell, D.A. and McDaniel, C.T. (1979) "Surface Radiative Exchange in Rod Bundles," *Journal of Heat Transfer*, 101(2), pp. 378–379. Available at: https://doi.org/10.1115/1.3450981.

U.S. Nuclear Regulatory Commission (1990) *Severe Accident Risks: An Assessment for Five U.S. Nuclear Power Plants*. NUREG-1150 Vol. 1. U.S. Nuclear Regulatory Commission Office of Nuclear Regulatory Research. Available at: https://www.nrc.gov/reading-rm/doc-collections/nuregs/staff/sr1150/v1/sr1150v1-intro-and-part-1.pdf.

U.S. Nuclear Regulatory Commission (1991) *Radiation Dose Limits for Individual Members of the Public (Subpart D), 10 C.F.R. § 20.1301*. U.S. Nuclear Regulatory Commission. Available at: https://www.ecfr.gov/current/title-10/chapter-I/part-20/subpart-D/section-20.1301.

U.S. Nuclear Regulatory Commission (2021) *Standard Technical Specifications General Electric BWR/4 Plants Volume 1, Specifications*. NUREG-1433 Volume 1 Revision 5.0. Washington, DC 20555-0001: U.S. Nuclear Regulatory Commission Office of Nuclear Reactor Regulation. Available at: https://www.nrc.gov/docs/ML2127/ML21272A357.pdf.

White, J.F. (1968) *SEVENTH ANNUAL REPORT AEC FUELS AND MATERIALS DEVELOPMENT PROGRAM*. NUCLEAR TECHNOLOGY DEPARTMENT NUCLEAR ENERGY DIVISION General Electric, pp. 316–351. Available at: https://doi.org/10.2172/4823661.

Wielenberg, A., Lovasz, L., Pandazis, P., Papukchiev, A., Tiborcz, L., Schöffel, P.J., Spengler, C., Sonnenkalb, M. and Schaffrath, A. (2019) "Recent improvements in the system code package AC2 2019 for the safety analysis of nuclear reactors," *Nuclear Engineering and Design*, 354, p. 110211. Available at: https://doi.org/10.1016/j.nucengdes.2019.110211.

Wieselquist, W.A., Lefebvre, R.A. and Jessee, M.A. (2020) *SCALE Code System*. ORNL/TM-2005/39. Oak Ridge, TN 37831-6283: OAK RIDGE NATIONAL LABORATORY. Available at: https://doi.org/10.2172/1616812.